



Volume 17 | Number 3 | July/September 2014

MAGAZINE

The Global Publication of the International Federation
of Societies of Cosmetic Chemists

Spectroscopic Analysis of Microstructure and Protein Degradation of Human Hair Caused by New Hair Straightening Systems

Skin Youthfulness Index –

A Novel Model Correlating Age with Objectively Measured Visual Parameters of Facial Skin

Preservation of Sympathetic Neuron-Adipocyte Crosstalk May Limit Chronic Emotional Stress-Mediated Fat Accumulation

Development of a Water-Based Long-Lasting Makeup: Dispersion of Hydrophobically Surface-Treated Pigments in an Oil-In-Water Emulsion

Restoration of Both Epithelial and Endothelial Perlecan / Dystroglycan Expressions by Polygonum bistorta induces Skin Rejuvenation

Balance of Cleaning Efficacy and Dental Hard Tissue Abrasive Wear: An In Vitro Study Assessing Toothpaste Effects Associated with Manual or Powered Toothbrushes

Scientific Papers

Spectroscopic Analysis of Microstructure and Protein Degradation of Human Hair Caused by New Hair Straightening Systems <i>Francini C. Picon, Viviane C. Albarici, Diogo Terci, Douglas Terci, Valeria Longo, Elson Longo, Adriano S. Pinheiro</i>	5
Skin Youthfulness Index – A Novel Model Correlating Age with Objectively Measured Visual Parameters of Facial Skin <i>Di Qu and Yulia Park</i>	8
Preservation of Sympathetic Neuron-Adipocyte Crosstalk May Limit Chronic Emotional Stress-Mediated Fat Accumulation <i>Pascale Prouheze, Barbara Morand, Jean-François Nicolaÿ, Mathilde Fréchet</i>	17
Development of a Water-Based Long-Lasting Makeup: Dispersion of Hydrophobically Surface-Treated Pigments in an Oil-In-Water Emulsion <i>E. Akiyama, Y. Yago, K. Fukuda</i>	23
Restoration of Both Epithelial and Endothelial Perlecan / Dystroglycan Expressions by Polygonum bistorta induces Skin Rejuvenation <i>Sabine Pain, Morgan Dos Santos, Amandine Gaydon, Aurelie Boher, Christelle, Nicolas Bechetoille, Patricia Rousselle, Valerie André</i>	31
Balance of Cleaning Efficacy and Dental Hard Tissue Abrasive Wear: An In Vitro Study Assessing Toothpaste Effects Associated with Manual or Powered Toothbrushes <i>Thomas Welss, Claudia Hundeiker and Thomas Förster</i>	37

IFSCC Magazine:	IFSCC Office/Publisher's Office	Important Information
Official scientific magazine of the International Federation of Societies of Cosmetic Chemists	IFSCC Suite 109, Christchurch House 40 Upper George Street Luton, Beds LU1 2RS, UK Tel: +44-1582-72 66-61 Fax: +44-1582-40-52-17 lorna.weston@ifsc.org	From 2014 onwards we publish the contents of the IFSCC Magazine on the IFSCC Website: www.ifsc.org
Publications Chair: <i>Andrea Weber</i> , Germany		You will have to sign in to the Member Zone where you can then find the Scientific Papers of the IFSCC Magazine Detail to be found on the Website:
Chair Science Committee: <i>Fujihiro Kanda</i> , Japan	Front Cover Design: <i>Fabian Mai</i> fabian.mai@sofw.com	You will find the contents on the IFSCC Website as follows:
Chair Education Committee: <i>Amy Wyatt</i> , USA	Layout: <i>Andrea Weber</i> andrea.weber@babor.de	News from Member Societies: News Page on Website
Scientific Editor: <i>Lothar Motitschke</i> , Germany		Awards: Awards Pages on Website
Language Editor: <i>Marcia Franzen-Hintze</i> , Germany		Educational Programs: Education Pages on Website
Honorary Auditors: <i>Anne Hunt</i> , France <i>Judy Beerling</i> , United Kingdom		Scientific Papers: Member Zone
4 issues / year Copyright 2014 Arranged in Germany ISSN# 1520-4561		

Spectroscopic Analysis of Microstructure and Protein Degradation of Human Hair Caused by New Hair Straightening Systems

Francini C. Picon¹, Viviane C. Albarici¹, Diogo Terci¹, Douglas Terci¹, Valeria Longo², Elson Longo², Adriano S. Pinheiro¹

¹ Kosmoscience Ciência e Tecnologia Cosmética Ltda., Valinhos, SP, Brazil.

² Universidade Estadual Paulista, Araraquara, SP, Brazil.

ABIHPEC Award winning paper at the 22nd IFSCC Conference, October 30-November 01, 2013, Rio de Janeiro, Brazil

Keywords: Hair straightening, hair microstructure, hair degradation, Raman spectroscopy, fluorescence spectroscopy

ABSTRACT

Hair straightening is a procedure widely used today. The hair damage caused by this procedure has been assessed via analysis of the cystine content in hair fibers. Another important indicator of overall hair health is tryptophan, which can be measured by fluorescence spectroscopy. To investigate the influence of different hair straightening treatments, hair fibers were analyzed by Raman spectroscopy, fluorescence spectroscopy and scanning electron microscopy, and the me-

chanical properties were determined. Tresses of bleached hair were prepared and then straightened once and 5 times with commercial products based on ammonium thioglycolate, guanidine hydroxide, sodium hydroxide, glyoxyloyl carbocysteine/glyoxyloyl keratin amino acids (glyoxyloyl system) and glyoxylic acid. Fluorescence spectroscopy showed that all straightening systems led to degradation of tryptophan. From Raman spectroscopy we concluded that straightening caused disorder in the hair fiber keratin structure with all straightening systems

employed. Straighteners based on the glyoxyloyl system and glyoxylic acid produced a significant increase in cysteic acid residues, resulting in oxidized fibers. Scanning electron microscopy allowed observation of damage to the hair surface induced by the straightening procedures. The glyoxyloyl and glyoxylic acid systems affected the mechanical properties of hair, but the influence was milder than with the thioglycolate, guanidine and sodium hydroxide systems.

INTRODUCTION

Hair fiber damage can be either the result of physical changes like grooming, or chemical processes such as bleaching, dyeing, relaxing or straightening. Hair straightening is a widely used procedure today.

Hair damage caused by straightening processes has been assessed via analysis of the cystine content in hair fibers. The cysteic groups are responsible for forming the tertiary crosslinkages in keratin fibers, which contribute to the physical and mechanical properties of hair fibers as well as their structural stability [1]. Thus, it is of key importance to evaluate and understand changes in the microstructure of hair fibers by investigating S-S groups [2]. Raman spectroscopy has been applied in several studies to investigate alterations in the -SS- groups because it is a non-destructive technique that requires no sample extraction or purification. Moreover, Raman spectroscopy provides information about S-S, C-S, C-C, amide I and amide III vibrations, which are weakly active or impossible to measure using infrared spectroscopy [3, 4].

Another important indicator of overall hair health is tryptophan, which can be measured by fluorescence spectroscopy. Tryptophan is an amino acid present in hair fibers that is largely used as an indicator of hair photo damage. Recent studies show that tryptophan fluorescence can be affected by chemical or physical modifications [5, 6].

In addition, determination of the mechanical properties of hair after chemical treatments by analysis of the load-elongation curves provides a rapid and simple method to correlate changes in the elasticity and tensile properties of hair [7, 8].

EXPERIMENTAL

Hair treatments

Tresses of bleached hair (DeMeoBrothers INC, NY, USA) were prepared and then straightened once and 5 times with products commercially available in the Brazilian market. These products are based on ammonium thioglycolate 6%, guanidine hydroxide 5%, sodium hydroxide 3%, glyoxyloyl carbocysteine/glyoxyloyl keratin amino acids (glyoxyloyl system) 20% and glyoxylic acid 10%. The straighteners were applied according to the manufacturers' instructions. The exposure time of the straighteners was standardized at 15 minutes. After the full procedure, all tresses were blow dried and straightened with a flat iron. Then the tresses were rinsed with SLES 10% solution and dried in a standardized environment at 22°C and 55% R.H.

Assessments

The fluorescence measurements were taken with a Fluorolog spectrophotometer, model FL3-12 (Jobin Yvon Horiba, Edison, NJ, USA) with a xenon light source providing the full solar spectrum. The experiments were performed in emission mode in the 300- 400 nm range. The excitation line utilized for the tryptophan evaluation was 294 nm and the emission intensity was evaluated at approximately 340 nm.

The Raman spectra were taken with a FT-Raman spectrometer (RFS 100/S – Bruker Inc., Karlsruhe, Germany). The 1064 line at 300mW from a Nd:YAG laser was the excitation source. Resolution was 4 cm⁻¹ and 64 scans were used for each sample. The spectral range was 20 – 2000 cm⁻¹. OPUS software (Bruker, Inc., Karlsruhe, Germany) was used to evaluate spectral characteristics. Normalization of Raman spectra of keratin fibers was carried out based on the C-H band at 1655 cm⁻¹, where the peak area was large and uninfluenced by straightening treatments.

Hair morphology was characterized using an FE-SEM Supra 35-VP (Carl Zeiss, Oberkochen, Germany).

A universal tester, EMIC model DL500, equipped with a 20N load cell, (EMIC, São José dos Pinhais, Brazil) was used in this study to measure the mechanical properties. Sixty hair strands, collected from the tresses of each

Figure 1: Fluorescence spectra of the study groups.

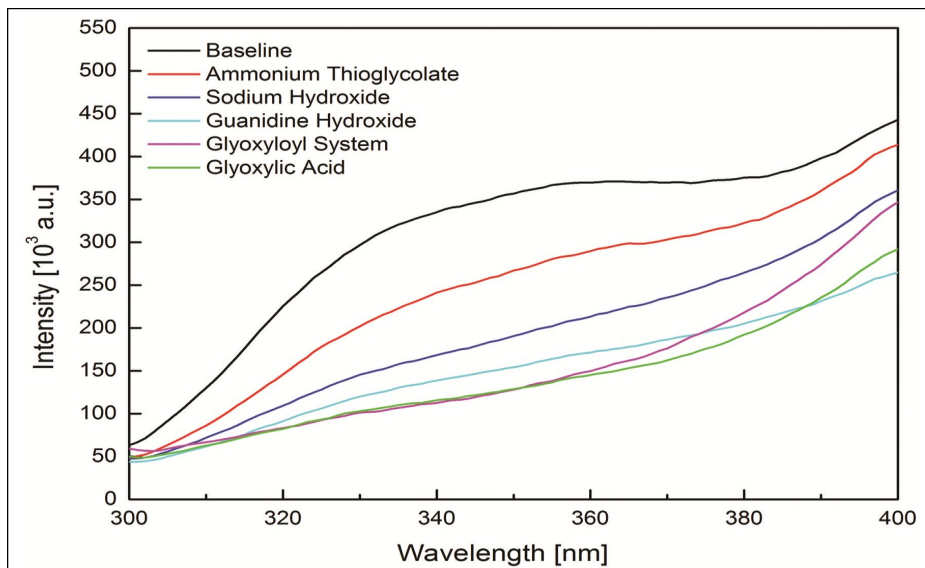
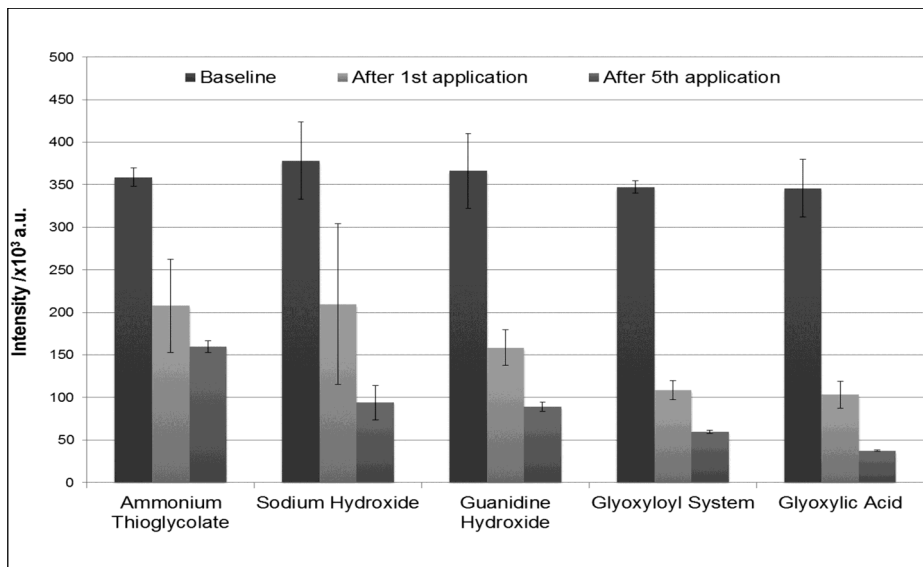


Figure 2: Fluorescence intensity for tresses before and after 1 and 5 applications of straightening treatments. Results are reported as the mean \pm SD, n=3.



treatment, were assessed. Each strand was held by a lower clamp and an upper clamp connected to the load cell of a dynamometer on the upper part. The parameter of force at break was assessed. The load cell was pre-charged, and the increase in load was measured with traction speed rates of 100 mm/min.

All tresses were measured after 1 and 5 applications of the straighteners and the results compared with those obtained for the baseline condition. The One-way ANOVA method followed by Tukey's post-test was used for statistical analysis of the results. The confidence interval was 95%.

RESULTS AND DISCUSSION

The excitation line employed for the tryptophan measurements was 294 nm, which proved to have the highest emission intensity at approximately 340 nm. **Figure 1** presents the fluorescence spectra and **Figure 2** shows the mean values of fluorescence intensity for the baseline condition of the tresses (before the straightening procedure) and for the tresses after the products were applied.

The comparison of the fluorescence intensity values obtained after 1 and 5 applications of the straighteners with the baseline values showed that the intensity of tryptophan emission was significantly reduced with all of the straighteners. These results suggest that all treatment systems led to degradation of

tryptophan.

There was no difference in tryptophan intensity between the results obtained after 1 and after 5 applications of the ammonium thioglycolate, sodium hydroxide and glyoxyloyl systems.

After 5 applications of guanidine hydroxide and glyoxylic acid, there was a decrease in tryptophan intensity compared with 1 application of these straightening systems.

After 1 application of hair straightener, the ammonium thioglycolate system showed no differences in the fluorescence intensity when compared with the guanidine hydroxide and sodium hydroxide systems. The tresses subjected to ammonium thioglycolate treatment showed higher values for the fluorescence intensity than those of the glyoxyloyl system and glyoxylic acid systems.

After 5 applications of hair straighteners, the ammonium thioglycolate straightening system showed higher values of fluorescence intensity than the guanidine hydroxide, sodium hydroxide, glyoxyloyl system and glyoxylic acid systems.

The sodium hydroxide system showed no differences in fluorescence intensity when compared with the guanidine hydroxide and glyoxyloyl systems after 5 applications.

The sodium and guanidine hydroxide systems showed higher values of fluorescence intensity than the glyoxylic acid system. There was no difference in fluorescence intensity between the glyoxyloyl and the glyoxylic acid systems.

The higher results obtained for the tryptophan fluorescence intensity for hair straightened with ammonium thioglycolate could be explained by the disruption of the hydrogen bond between tryptophan and alanine that releases tryptophan, as described by Jachowicz [5].

The Raman spectra of the human hair fiber for the baseline condition (tresses before straightening process) and for the tresses after the application of the products are shown in **Figure 3**. The disulfide content of the hair samples was determined by estimating the ratio of the peak area of the S-S band (506 - 519 cm^{-1}) divided by the peak area of the C-H band (1656 cm^{-1}). Similarly, the sulfonic acid function produced by straightening was assessed by estimating the ratio of the peak area of the S-O band (1040 cm^{-1}) divided by the peak area of the C-H band (1655 cm^{-1}).

The ratio of the peak areas of the S-S and S-O

bands for the baseline condition and the ratio after 1 and after 5 applications were compared. The S-S band intensity did not decrease after straightening when compared with untreated fibers, indicating that the broken -S-S- bonds were reformed in the neutralization process with reducers such as thioglycolate, guanidine and sodium hydroxide and in an after-heat process in case of glyoxyloyl system and glyoxylic acid. However, the shape of the S-S band was modified by straightening, which was previously observed in untreated hair, where two conformations were reported for the S-S band, one at 508 cm⁻¹ taken as the gauche-gauche-gauche (GGG) conformation and the other 520 cm⁻¹ taken as the trans-gauche-gauche (TGG) conformation.

After straightening, the TGG conformation was preferentially observed because although S-S bonds reform, the structure of the polypeptide chain begins to show greater disorder than in untreated hair that is composed of GGG and TGG conformations where

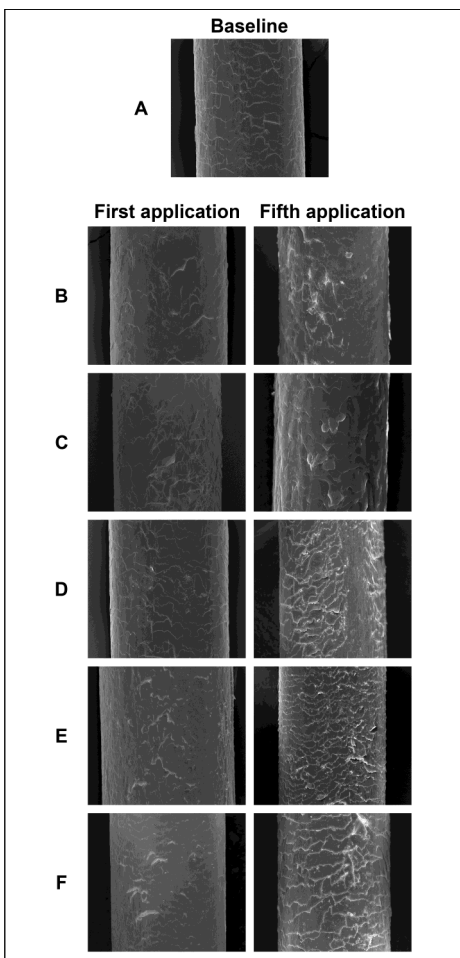


Figure 5: FE-SEM images of the human hair surface before the straightening procedures (a) and after 1 and 5 applications of the straightening systems: (b) ammonium thioglycolate, (c) sodium hydroxide, (d) guanidine hydroxide, (e) glyoxyloyl system and (f) glyoxylic acid.

Figure 3: Raman spectra of the study groups.

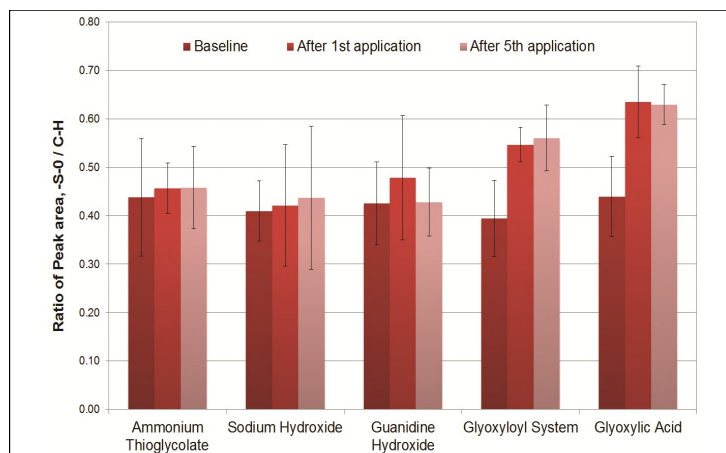
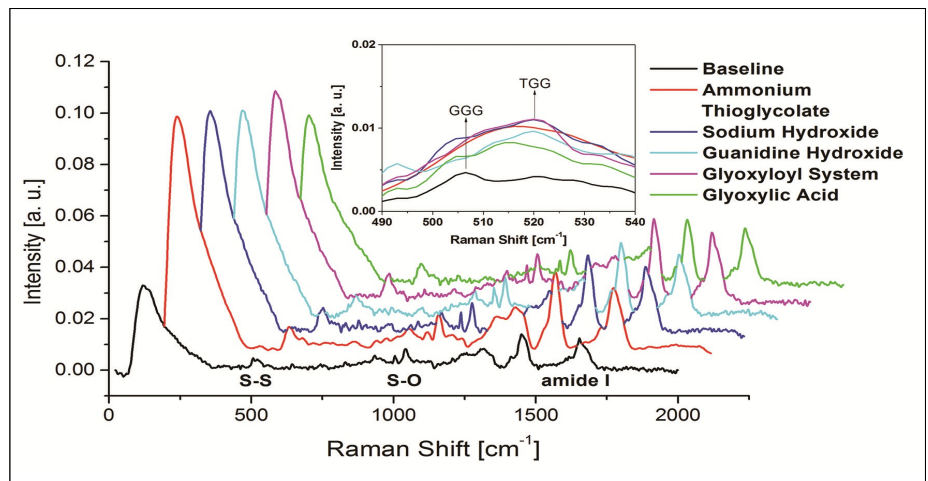


Figure 4: Ratio of peak area S-O/C-H for the tresses before and after 1 and 5 applications of straightening treatments. Results are reported as the mean ± SD, n=3.

the distance between a polypeptide chain and the other polypeptide chain surrounding the S-S bond is shorter. As a consequence, the untreated hair assumes a more compact structure than straightened hair. We observed an increase in intensity of the sulfonic groups in hair fibers subjected to one application of glyoxyloyl system and glyoxylic acid systems when compared with untreated hair, showing that these actives promote strong oxidation of hair fibers (Figure 4). However, after five applications of the glyoxyloyl system and glyoxylic acid systems, there was no difference in intensity of the sulfonic groups from after one application, indicating that the accumulated applications did not increase the surface oxidation of the fibers.

Figure 5 shows examples of images of the hair surface before and after the straightening procedures.

The scanning electron microscopy (SEM) images showed the surface changes in hair fibers after straightening. According to the SEM micrographs, the applications of straightening products damaged the hair surface, as evidenced by lifting of the cuticles, and the damage to the hair surface worsened with an

increase in the number of applications with all systems. This damage to the hair surface was expected, since the treatments are chemically aggressive, making use of oxidizing and reducing agents in combination with thermal treatments like blow drying and a flat iron.

The force at break was measured before and after 1 and 5 applications of straightening treatment (Figure 6). The results of the statistical analysis indicated that there was a decrease in the force at break after the first application of the straightening systems. The decrease in the force at break became larger with an increasing number of applications (from 1 application to 5 applications), but was not as great with the glyoxylic acid system. The only system that showed no decrease in strength with an increasing number of applications was the glyoxyloyl system. Therefore, the glyoxyloyl and glyoxylic acid systems, in spite of affecting the mechanical properties of hair, were milder than the classical systems (thioglycolate, guanidine and sodium hydroxide).

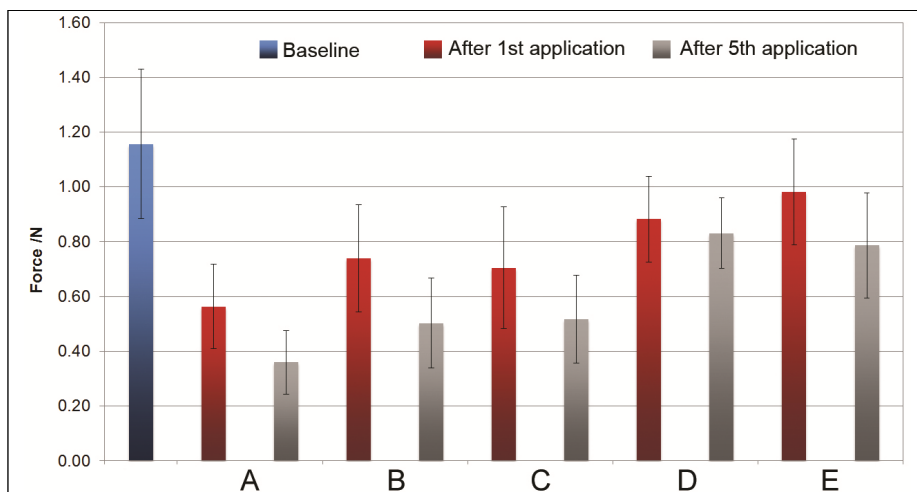


Figure 6: Force at break (N) before and after 1 and 5 applications of the straightening systems: (a) ammonium thioglycolate, (b) sodium hydroxide, (c) guanidine hydroxide, (d) glyoxyloyl system and (e) glyoxylic acid. Results are reported as the mean \pm SD, n=60.

CONCLUSIONS

The results obtained with fluorescence spectroscopy showed that all straightening systems lead to degradation of tryptophan. From Raman spectroscopy, we concluded that all straightening systems studied caused disorder in hair fiber keratin structure. Straighteners based on glyoxyloyl and glyoxylic acid systems produced a significant increase in cysteic acid residues, resulting in more oxidation of hair fibers. By means of SEM images it was possible to observe damage to the hair surface induced by the straightening procedures.

The mechanical properties of hair were affected by all straightening systems. The force at break was significantly decreased with all straightening systems, and this effect was greater with the classical straighteners. Increasing the number of product applications also increased damage to the internal structure of hair fiber and decreased the force at break, notably with the classical straighteners.

We conclude that the internal structure of hair was better preserved by the glyoxyloyl and glyoxylic acid systems than by hair subjected to classical systems.

REFERENCES

- [1] Gniadecka, M., Nielsen, O. F., Christensen, D. H. and Wulf, H. C., *Structure of Water, Proteins, and Lipids in Intact Human Skin, Hair, and Nail*, *The Journal of Investigative Dermatology*, 110, (1998) 393-398.
- [2] Brenner, L., Squires, P. L., Garry, M., and Tumosa, C. S., *A Measurement of Human Hair Oxidation by Fourier Transform Infrared Spectroscopy*, *Journal of Forensic Sciences*, 13, (1985) 420-426.
- [3] Kuzuhara A., *Analysis of Structural Changes in Bleached Keratin Fibers (Black and White Human Hair) Using Raman Spectroscopy*, *Biopolymers*, 81, (2006) 506-514.
- [4] Kuzuhara, A., *Analysis of structural changes in permanent waved human hair using Raman spectroscopy*, *Biopolymers* 85, (2007) 274-283.
- [5] Jachowicz, J., & McMullen, R. L., *Tryptophan fluorescence in hair-examination of contributing factors*, *Journal of Cosmetic Science*, 62, (2011) 291-304.
- [6] McMullen, Roger L., Susan Chen, and David J. Moore, *Spectrofluorescent characterization of changes in hair chemistry induced by environmental stresses*, *Journal of the Society of Cosmetic Chemists*, 62, (2011) 191-202.
- [7] Richard Beyak, B.S., C. F. Meyer, M.S., M.B.A., and G. S. KASS, B.S., *Elasticity and Tensile Properties Human Hair. I. Single Fiber Test Method*, *Journal of Society Cosmetic Chemists*, 20, (1969) 615 – 626.
- [8] ROBBINS, C. R., *Chemical and Physical Behavior of Human Hair*. Nova York, Springer-Verlag, 1994, 3rd Edition, 105-148

Corresponding author
email: francini@kosmoscience.com

Skin Youthfulness Index – A Novel Model Correlating Age with Objectively Measured Visual Parameters of Facial Skin

Di Qu and Yulia Park

Advanced Imaging and Measurement Laboratory, R&D
Amway Corporation, 7575 Fulton St East, Ada, MI 49355, USA

This publication was presented as a podium presentation at the 22nd IFSCC Conference, October 30 – November 01, 2013, Rio de Janeiro, Brazil.

Keywords: skin youthfulness index, age correlation, objective measurement, skin aging parameters, image analysis.

ABSTRACT

A novel skin youthfulness index is introduced in this study to establish a mathematical model that correlates age with the visual properties of facial skin using an image analysis method. Images of 1,505 Asian female volunteers between the ages of 20 and 60 years were captured using a VISIA-CR[®] system under five different lighting conditions. Skin properties, such as wrinkles, hyperpigmentation, pores, color, translucency, ITA[°], color evenness and

surface texture parameters, were objectively measured from the images using Amway exclusively developed image analysis algorithms. Correlations between the measured parameters and the participants' chronological age were observed with statistical significance. By defining and calculating a set of weight factors five objectively measured visual parameters of skin were found to be most relevant to describe skin conditions influenced by the aging process. Combining these parameters in a mathematical model we have established a

skin youthfulness index which has a range of 0 to 100 and is inversely correlated to people's chronological age ($R^2 = 0.9959$). The index allows us to accurately assess a person's apparent skin age based on the measured skin parameters. Of the various age groups tested, the largest difference between the actual and the calculated skin age was 2.4 years with a mean difference of 0.86 years. This model has potential for quantification of skin care product efficacy and thereby substantiation of new product claims.

INTRODUCTION

Skin is the largest organ in the human body and measuring the changes in its properties with age is a primary topic in skin related research [1]. Skin care researchers have strived to develop a comprehensive model correlating multiple skin properties with age, thereby providing an objective and quantitative measure of skin conditions that will help assess the efficacy of skin care products and treatments [2].

Currently, most models reported in the literature use subjectively measured skin parameters to assess skin aging. Guinot et al. [3] introduced a skin age score (SAS) correlating 24 visual and tactile parameters of facial skin with chronological age, concluding that SAS could be generated from the evaluation of multiple discrete signs on facial skin and was an informative tool for quantifying skin aging. Vierkotter et al. [4] reported a skin aging index (SCINEXA) which incorporates 23 clinically graded intrinsic and extrinsic parameters characteristic of skin aging. They concluded that the model could be used to separate the extrinsic and intrinsic effects of aging. Nkengne et al. [5] established an index of aging using clinically graded parameters such as the degree of wrinkles, brown spots, and sagging. They believed that their skin aging index captured information relevant to the visual transformation of facial skin with

age and was meaningful when applied to product efficacy evaluations. Additional research by Bazin and Doublet [6] and Bazin and Flament [7] described linear correlations with multiple clinically assessed parameters for Caucasian and Asian populations, respectively. While subjective grading is the current standard of clinical assessment, it is a common belief that the subjectivity of these assessments carries the intrinsic possibility of variation between graders and inconsistency in the grader's perception at different time points.

Zedayko et al. [8] developed an instrumental method to correlate age with skin brightness of Caucasian subjects. While the measurement was objective and the correlation was good, the approach was rather simplistic in that it only used skin color as the measurable aspect of skin aging. A more complex measurement was established by Dicanio et al. [9], in which a linear function between age and multiple skin parameters was constructed using principal component analysis and multivariate regression. A total of 76 parameters (10 clinical, 14 biophysical and 52 biochemical) were analyzed to identify 12 primary variables for age estimation. While the statistical analysis method was sound, the physical significance of their results was still open to discussion. For example, both clinical and instrumental measurements of the same skin property (such as crow's feet) were included

in the formula as two independent variables, which was difficult to justify. In addition, both glycation (a biochemical parameter) and the degree of wrinkles (a clinical parameter) were included in their model. Since it is commonly believed that glycation is the molecular marker for the clinical signs of aging [10, 11], listing both of them as separate independent variables in a linear equation could potentially impair the validity of the model.

Over the past decade, sophisticated facial imaging systems have been developed to measure visual properties of skin using image analysis [12]. Our skin research program uses Amway-designed Facial Analysis Computer Evaluation System (F.A.C.E.S.) which has been used to establish an infrastructure of more than 20 facial imaging centers in various countries and regions throughout the world. Since 2007, we have collected images from more than 30,000 people worldwide, representing a wide range of ages and ethnicities in both genders. This vast database has allowed us to analyze multiple visual parameters of facial skin and correlate them with age.

Compared with the studies referenced above, which used subjective or multiple instrumental methods to collect age related data, exclusive use of image analysis for the quantification of the visual signs of aging has

Age group	20	25	30	35	40	45	50	55	60			
Age	20	25	30	35	40	45	50	54	55	59	60	61
Count	156	275	201	194	175	135	100	78	84	26	51	30
Total Count	156	275	201	194	175	135	100	162		107		

Table I: Age and Count Distribution of the Study Participant Population

the advantage of being more simple than the multi-instrument method and in the mean time is more comprehensive than the single measurement technique. In this report, we describe a novel model correlating the chronological age of female Asian consumers with a list of objectively measured visual parameters of facial skin. This approach establishes a comprehensive function, the skin youthfulness index (SYI), calculated using image analysis to bridge age and the measured skin properties. A special focus was placed on calculating meaningful weight factors for each of the skin parameters in order to improve the age correlation and more accurately predict skin age based on visually displayed skin conditions.

EXPERIMENTAL

Facial imaging system

A VISIA-CR® System (Canfield, U.S.A.) was used to capture facial images under five different lighting conditions (standard, flat, UV, cross polarized, and parallel polarized). The system consisted of a facial imaging booth with eight flashes placed at different locations for uniform illumination, a Nikon 200 SLE camera, and a set of standard color plates. The camera settings were ISO100, f14, and “cloudy” for white balance. An Amway proprietary F.A.C.E.S. software was used to control the image capture process.

Study Design

From our image database of more than 30,000 participants collected around the world, we used the images of 1,505 female volunteers between the ages of 20 and 60 years covering four Asian countries in the East, Far East, and South East regions. The selection was made to have exact or almost exact ages in each of nine age groups (e.g. volunteers in the 20, 25, 30, 35, 40, 45, and 50- year-old groups were exactly at the claimed age, while the 55-year-old group consisted of volunteers 54 and 55 years old, and the 60-year-old group consisted of volunteers 59, 60 and 61 years old). Our large image database allowed us to make this tight age selection, which consequently improved the predictability of the model by using finer age

ranges of study subjects. Currently, in the literature the age ranges of study subjects are usually wide, e.g., 20s (to represent subjects aged 20 – 29 years), 30s (30 – 39), 40s (40 – 49), etc. We believe more accurately defined age ranges help to construct a more accurate mathematical model. **Table I** summarizes the age and the count of the volunteer population included in this study. At least 100 subjects in each age group were included in this study, which provided a good approximation of skin property distribution of the general population.

All participants were confirmed by means of written informed consent. Five front view images of each study volunteer were taken during the image collection stage after face washing by a standardized cleansing procedure. Using proprietary image analysis software, visual skin properties representative of aging (wrinkles, pores, translucency, redness, yellowness, ITA°, unevenness of skin tone, and surface texture parameters) were quantified from the set of captured images.

Image analysis

Parameters obtained through F.A.C.E.S. analysis

Amway’s F.A.C.E.S. and other proprietary image analysis algorithms were used to objectively quantify facial skin properties such as wrinkle score, hyperpigmentation score, pore count, skin color parameters, lightness

of skin tone, evenness of skin tone, skin translucency, and surface texture properties. All images were first color corrected using standard color plates embedded in each picture to achieve accurate measurements of skin color and other visual skin properties. The automatic feature recognition algorithms generate a facial mask that excludes eyebrows, eyes, nostrils, mouth, and terminal hair, rendering only the skin surface for accurate wrinkle, pore, and subsurface hyperpigmentation analysis. A representative graphic output of the facial masks is shown in **Figure 1**.

Facial wrinkle analysis was performed in the entire facial area. A wrinkle score was reported which reflected both the number of wrinkles and wrinkle severity; therefore, a deep wrinkle would be equivalent to multiple smaller wrinkles lying on top of each other in one location. Skin sub-layer hyperpigmentation was measured from the UV images in which areas with large amounts of melanin deposition were quantified to produce a hyperpigmentation score. Facial pores were quantified in the selected regions of interest that included the nose, upper lip, chin, cheek areas close to the nose, and portion of the forehead close to the eyebrows. The output of the facial pore analysis included pore count and pore area.

Facial skin color was measured using the cross-polarized images. Regions of interest on the cheeks and forehead were created following automatic detection of the facial features such as hairline, eyes, eyebrows, nose, and mouth. Color parameters in the RGB color space were obtained from the regions of interest and converted to the L*, a* and b* of the CIELAB color space using in-house developed algorithms in ImageJ (National Institutes of Health). The skin individual typology angle (ITA°) was calculated using the

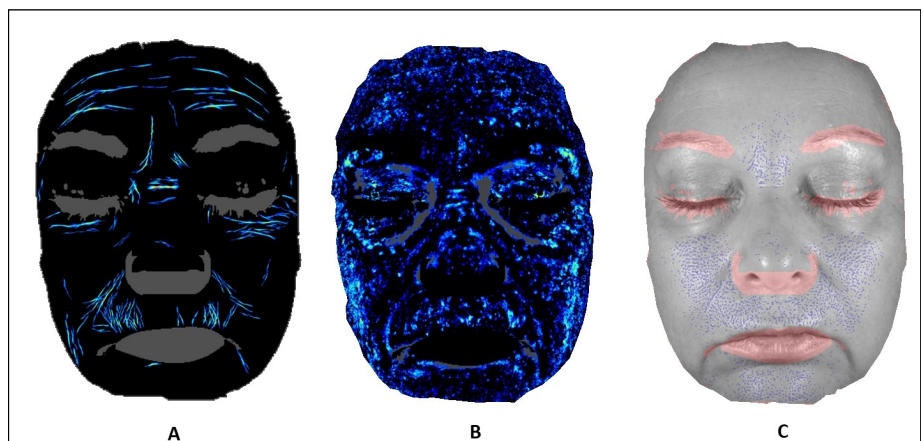


Figure 1: A representative graphic output (a screenshot) of the facial masks generated by our F.A.C.E.S. analysis software showing quantified facial skin properties. A= wrinkles, B= skin sub-layer hyperpigmentation, and C= facial pores.

measured L^* and b^* values. Unevenness of skin tone (U) was measured as the variance of pixel intensity in each region of interest. Skin surface texture parameters were obtained from the region of interest using the Gray Level Co-occurrence Matrix (GLCM) statistical method, a built-in function of ImageJ. Two GLCM parameters, entropy (E) and inverse difference moment (IDM), were found to be the most relevant to describing the age-related changes of skin texture properties. Entropy is a measure of the orderliness of the surface texture pattern. The skin with more fine lines and wrinkles often shows a more regular parallel pattern and would therefore result in higher entropy values. The IDM, on the other hand, indicates the homogeneity of surface texture pattern. A uniform surface texture pattern like that of young skin would have a high IDM value.

Skin translucency, a quality of facial skin greatly appreciated in Asian culture, was measured by using both cross-polarized and parallel-polarized images. Skin with high translucency is perceived by consumers to have a flawless surface appearance, delicate texture, subtle subsurface reflection, and a rosy glow. Matsubara et al. [13] described an image analysis method to quantify facial skin translucency. We employed a modified version of this method by quantifying skin translucency through diffuse reflection, as opposed to specular reflection used in Matsubara's study, and defined a skin translucency index based on the average intensity value and its distribution in each of the RGB channels.

DATA ANALYSIS

Data type and range

Properties of the 10 objectively measured visual parameters of facial skin are summarized in **Table II**. The extensive properties such as wrinkles, sub-layer spots, and pores were measured in the whole face area, while the intensive properties such as color and texture were measured in regions of interest on both cheeks.

Statistical analysis

Statistical analysis was performed using JMP® 10.0.0 statistical software (SAS Institute Inc.). Distribution and histogram analyses were performed with the data normality test, and ANOVA/Tukey-Kramer analysis was used for comparisons of the means of skin properties among various age groups.

Multiple regression analysis

A multiple regression analysis was performed

Table II: Properties of objectively measured visual parameters of facial skin

Parameter	Name	Data range	Mean value (20-60 years old)
W_r	Wrinkles	0 – 600	80
S	Sub-layer spots	10 – 1500	166
P	Pores	10 – 4000	1632
T	Skin translucency	10 – 100	39
a^*	Redness	9 – 30	16
b^*	Yellowness	13 – 34	24
ITA°	Skin tone lightness	6 – 63	42
U	Color unevenness	10 – 200	65
E	Texture orderliness	3 – 7	6
IDM	Local homogeneity	0.3 – 0.7	0.5

using JMP® to correlate participant age with the objectively measured skin parameters in order to establish a linear equation in the following form:

where I = intercept; C = coefficient; V = value

$$\text{Predicted Age} = I + \sum_{i=1}^n C_i V_i \quad \text{Equation 1}$$

of an objectively measured visual parameter; and i = any specific parameter.

Skin youthfulness index

In addition to the multiple regression method, we established a new model, a skin youthfulness index (SYI), by correlating the age of the study participants with the measured parameters of their facial skin. The following requirements were considered to define the SYI :

- A single comprehensive index that indicates the youthfulness of facial skin and is correlated inversely with people's

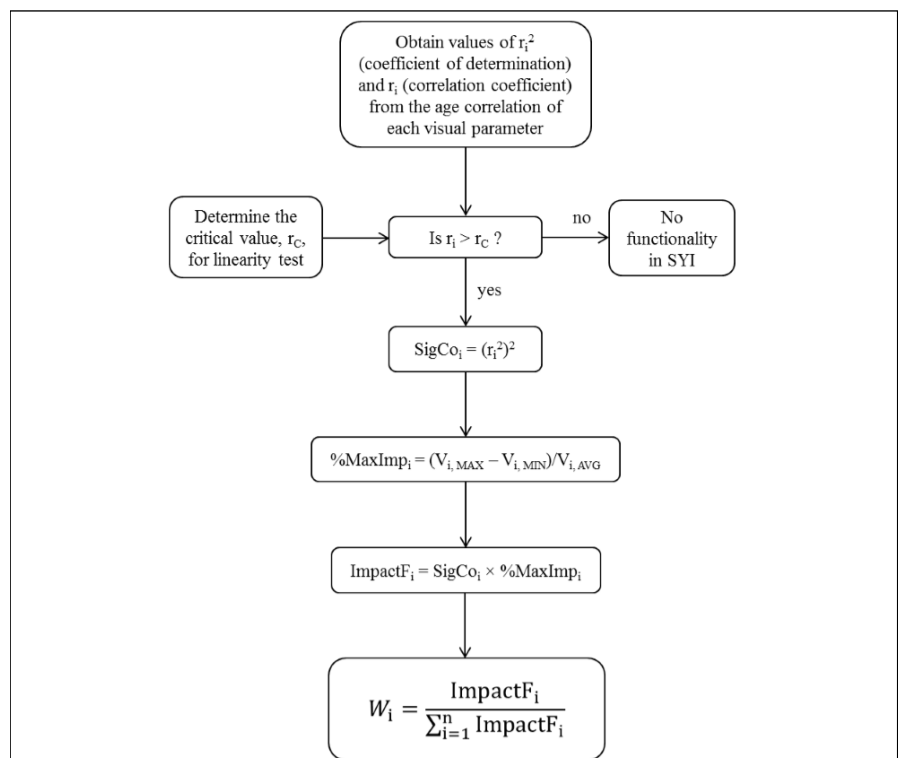


Figure 2:

Flow chart for calculation of weight factors of the objectively measured visual parameters of facial skin. r^2 : coefficient of determination, r : correlation coefficient, r_c : critical value for linearity test, SYI : skin youthfulness index, $SigCo$: significance factor, $\%MaxImp$: maximum impact factor, $ImpactF$: impact factor, W : weight factor and i : any of the objectively measured visual parameter of facial skin.

chronological age (i.e., younger people have a higher index value and older people a lower value)

- An index that is affected by the measured visual parameters in a linear composite fashion through appropriately defined weight factors
- The positive or negative effect of each parameter on the index is reflected (i.e., the value of a parameter that increases with age would have a negative influence on *SYI*, whereas the value of a parameter that decreases with increasing aging would have a positive effect).
- A target scale for the index of 0 – 100

Based on these considerations, the following linear composite function was proposed:

$$SYI = N_1 \left(N_2 + \sum_{i=1}^n J W_i (\ln V_i) \right) \quad \text{Equation 2}$$

where *W*= weight factor; *V*= value of an objectively measured visual parameter; and *i*= any specific parameter type. The constants *N*1 and *N*2 are factors to produce *SYI* values on a scale of 0 – 100. The *J* term in Equation 2 indicates whether a parameter has a positive or negative effect on *SYI* where *J*= 1 represents a positive effect and *J*= -1 a negative effect. For example, since a higher age indicates a lower *SYI* value, an increasing wrinkle score with increasing age would have a negative effect on *SYI*.

Weight factor calculation

Calculating the weight factor *W* for each visual parameter was a key step in the development of the index and was performed as outlined in the flow chart shown in **Figure 2**. Basically, the coefficient of determination, r_i^2 , and the correlation coefficient, r_i , were obtained from the age correlation plots for each of the 10 visual parameters (**Figures 3A – 3J**). A linearity test was conducted by determining a critical value for the correlation coefficient [14]. If the correlation of a parameter passed the linearity test, the variable was considered meaningful and included in the weight factor calculation. A significance factor was then defined, $SigCo = (r^2)^2$, which ranks the significance of the contribution of the ten visual parameters. Then a maximum impact factor (%MaxImp) was defined emphasizing the level of influence a variable has as it changes with age (i.e., a high %MaxImp indicates that the parameter has a high impact on the *SYI*-age correlation). Then the impact factor, defined as ImpactF, was calculated as the product of SigCo and %MaxImp. Finally, the weight factor was calculated by normalizing the impact factor in a unit fraction form.

Age prediction from *SYI*

After a function of *SYI* is obtained, it can then be correlated with the study participants' chronological age to establish an *SYI*-age curve. Such a curve enables us to examine the goodness of fit of Equation 2 by computing the residual sum of squares, a statistical parameter, between each group's actual and calculated age. In addition, this *SYI*-age correlation allows us to calculate a person's skin age from the objectively measured visual parameters of facial skin, as discussed later in the results and discussion.

Parameter optimization

To identify parameters that contribute most meaningfully to *SYI*, we used RSS to compare the goodness of fit in the *SYI*-age correlation.

Using Equation 2, the individual effect of each parameter was first evaluated to identify the one which correlated the best with age. The combined effects were then examined by adding other parameters one after another to Equation 2. Their corresponding RSS values were calculated and compared to determine if the age correlation was improved.

RESULTS AND DISCUSSION

Effect of age on the measured visual parameters of skin

It has been well documented through clinical grading that a person's visual signs of aging

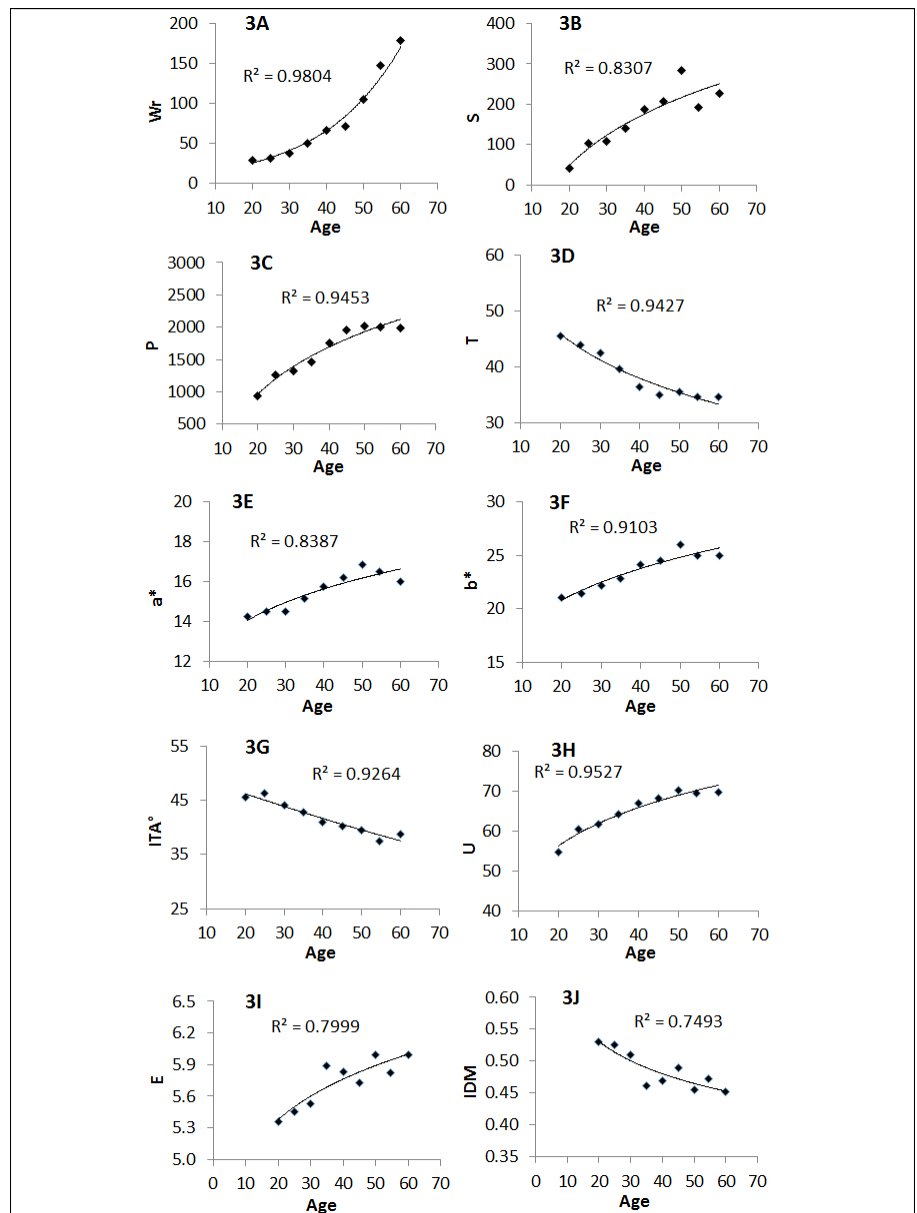


Figure 3: Correlation of age with each of the ten objectively measured visual parameters. 3A: wrinkle score (Wr), 3B: count of sub-layer spots (S), 3C: pore count (P), 3D: skin translucency index (T), 3E: skin redness (a^*), 3F: skin yellowness (b^*), 3G: skin tone lightness (ITA°), 3H: color unevenness (U), 3I: texture orderliness (E), and 3J: local homogeneity (IDM).

increase with age [15]. In this study, we observed statistically a significant age correlation for each of the ten objectively measured visual properties (wrinkles, pores, translucency, redness, yellowness, ITA° , unevenness of skin tone, and surface texture). **Figure 3** shows the average values of each of the visual parameters plotted against the participants' chronological age.

The average wrinkle score increases exponentially with increased age (**Figure 3A**). This is, to our knowledge, the first time such a trend has been reported. Since our F.A.C.E.S. algorithms include both number and severity of facial wrinkles in the calculation, a deep and wide wrinkle is represented by multiple single wrinkle lines as opposed to a single line color-coded to differentiate it from other smaller wrinkles, as seen in many commercial wrinkle-analysis software packages. We believe an exponential increase in facial wrinkling over age displays a meaningful progression of the aging process of human facial skin.

The curve in **Figure 3B** indicates that the amount of sub-layer spots increases with age. This is due to the accumulative UV damage acquired during life. **Figure 3C** shows the average number of visible pores, which increases steadily with age and reaches a plateau after age 45. While it is difficult to argue that the pore number increases with age in a physiological sense, we can conclude that, due to changes in skin color and pore size, facial pores become more easily detectable with age, both visually and with image analysis. Facial skin translucency decreases with increasing age (**Figure 3D**) and levels off after age 45. Younger people possess higher skin translucency, as their skin looks less dull and exhibits higher diffuse reflection. Therefore, the color components in the subsurface of skin are more visible in younger people.

Parameters	Estimate, I & C_i	Prob> t
I	25.25077	<.0001
Wrinkles, Wr	0.090014	<.0001
Sub-layer spots, S	0.008194	<.0001
Pores, P	0.005913	<.0001
Redness, a^*	-0.32862	<.0001
Skin tone lightness, ITA°	-0.3403	<.0001
color unevenness, U	0.022603	0.0065
Texture orderliness, E	2.33272	<.0001

Table III: Estimated parameters (I & C_i in Equation 1) using multiple regression analysis

The lightness of skin tone, as defined by ITA° , decreases steadily with increasing age (**Figure 3G**), indicating that older people have darker complexions, which agrees with the trend of changing facial skin color in a Caucasian population [8]. One component of ITA° , b^* which is a measure of skin yellowness, increases with age (**Figure 3F**), indicating that older people in general have more yellowish skin tone. A similar trend is observed for skin redness as shown by the a^* values in **Figure 3E**.

Unevenness of facial skin tone increases with age due to discoloration, wrinkling, and other physiological changes (**Figure 3H**). The local homogeneity of skin texture (IDM) decreases with age, while the orderliness of skin texture (entropy) exhibited the opposite trend, as shown in **Figures 3J** and **3I**.

Age correlation by multiple regression analysis

The values of ten objectively measured visual parameters were fitted to Equation 1 using the multiple regression tool in JMP[®]. After examining the outcome of the analysis, three parameters (STI , b^* , and IDM) which had p -values larger than 0.05 were removed from the correlation. The final linear equations obtained from the multiple regression analysis correlated the participants' age with seven parameters with $r^2 = 0.6277$. The output of the multiple regression is shown in **Table III**. Inserting these values into Equation 1 we calculated the predicted age of the nine groups of Asian female volunteers using the average values of these visual parameters. **Figure 4** shows the correlation between the actual age and the predicted age of each group with $RSS = 215.32$. Compared with the best fit line (diagonal), the predicted ages deviated more in the lower and higher age groups. The largest difference between the predicted and the actual age was 8.0 years.

Parameter	Weight factor (W)	After parameter optimization
Wrinkles, Wr	0.435	0.627
Sub-layer spots, S	0.202	0
Pores, P	0.121	0.174
Translucency, T	0.056	0.081
Redness, a^*	0.026	0
Yellowness, b^*	0.038	0.056
Skin tone lightness, ITA°	0.044	0
color unevenness, U	0.043	0.062
Texture orderliness, E	0.015	0
local homogeneity, IDM	0.019	0
Total	1.000	1.000

Table IV: Weight factors for Equation 2

Skin youthfulness index and its correlation with age

To calculate skin youthfulness index (SYI), we first calculated the weight factors for each of these ten visual parameters by following the flow diagram described in **Figure 2**. The results are shown in **Table IV** from which we can see that skin wrinkling has the most significant effect on the SYI . This is due to the fact that it is closely correlated with age and its change over age is the largest in the order of magnitude. This agrees with the common understanding that facial wrinkling is a significant marker for skin aging. By plugging the objectively measured visual parameters from each of the 9 age groups into Equation 2 we could calculate a set of SYI values for the corresponding age groups. Then by correlating the SYI with the volunteers' actual age a linear function was obtained which allowed us to back-calculate their apparent skin age based on their objectively measured visual skin parameters. **Table V** summarizes these results together with the difference between the predicted and the actual age of the study volunteers. The goodness of fit was calculated from this table and a $RSS = 22.96$ was obtained, which is much better than that of the multiple regression method.

Using the parameter optimization method described above, we further examined the effect of each visual parameter and the combinations of various parameters which contribute to the SYI -age correlation. This was done by finding the best age correlation (the least RSS) among the individual parameters and then adding more parameters one after another to identify the best combination at the next level. Among the ten individual visual parameters, the effect of wrinkle score correlated the best with age ($RSS = 12.61$). Adding other parameters to the wrinkle score and screening through all ten parameters at various combinations, we were able to obtain

Average age (actual)	SYI	Average age (calculated)	Difference
20	73.8	18.0	2.0
25	70.7	26.2	1.2
30	69.5	29.2	0.8
35	67.0	35.9	0.9
40	64.6	42.3	2.3
45	63.4	45.4	0.4
50	61.1	51.6	1.6
55	60.3	53.6	0.9
60	58.9	57.3	2.7

Table V: Results of SYI and age Calculation using equations 2 & 3

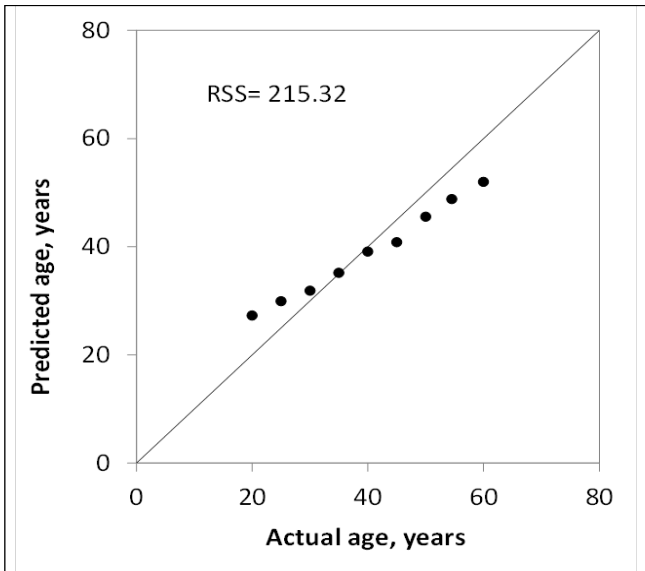


Figure 4: Correlation plot of the predicted and actual ages of nine female Asian groups using the multiple regression method. RSS: residual sum of squares, a measure of the discrepancy between the actual age and the age calculated from the regression model.

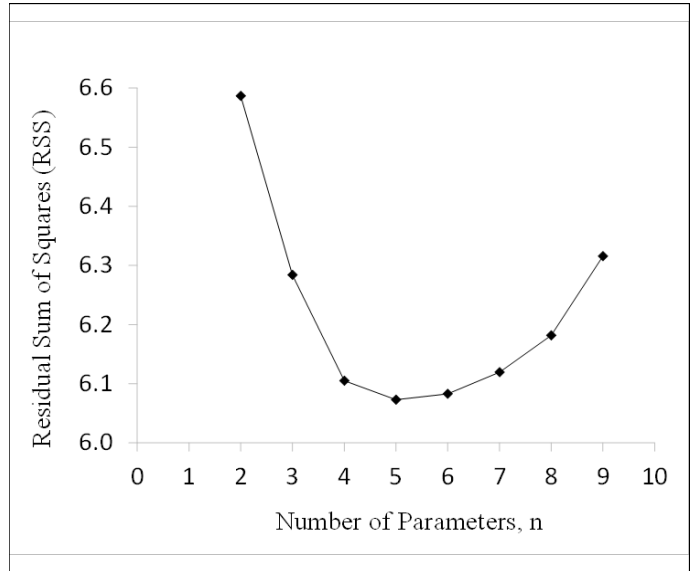


Figure 5: Effect of parameters and their combinations on the goodness of fit of the SYI model. The RSS value for wrinkles alone was 12.61, high out of the chart area. As more parameters are added to the wrinkle score, RSS starts to decrease until reaching a minimum. More parameters added after that have negative effects on RSS and its value starts to increase. The RSS value for the all 10 parameter combination was 22.96, high out of the chart area. The minimum point of a 5-parameter combination represents the optimal condition for the SYI-age correlation.

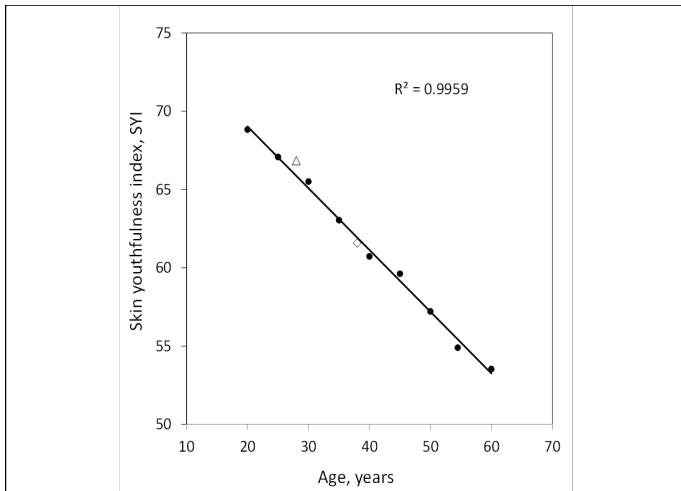


Figure 6: Correlation between age and skin youthfulness index. Solid dots: SYI values calculated (using Equation 3) from the 5-parameter combination from the facial skin of 20, 25, 30, 35, 40, 45, 50, 55, and 60-year-old age groups. Hollow triangle: calculated SYI of the 28-year-old age group. Hollow diamond: calculated SYI of the 38-year-old age group.

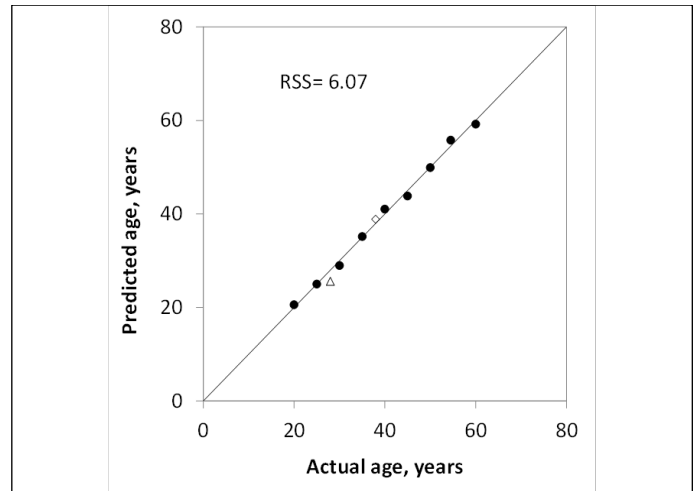


Figure 8: Correlation plot of predicted and actual ages using the skin youthfulness index function. Solid dots: SYI values calculated from the five objectively measured visual parameters of facial skin for the 20, 25, 30, 35, 40, 45, 50, 55, and 60-year-old age groups. Hollow triangle: calculated SYI of a 28-year-old group. Hollow diamond: calculated SYI of a 38-year-old group.

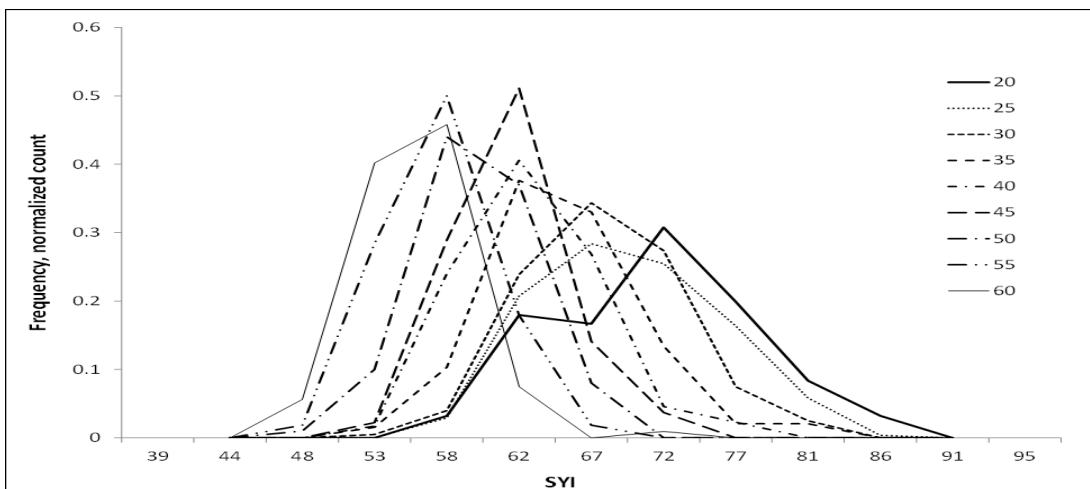


Figure 7: Distribution of the skin youthfulness index (SYI) in each of the nine age groups of the Asian female population. The numbers in the legend indicate group ages in years. The SYI distribution shifts from high to low regions with increasing group age.

the optimal parameter combination as shown in **Figure 5**. From the chart we can see that by combining more parameters with wrinkles a better age prediction was achieved with decreasing RSS values until a point where adding more parameters started to influence the *SYI*-age correlation in a negative way. This optimal combination involved five parameters: wrinkle score, pores, skin translucency, yellowness, and color unevenness. Their corresponding weight factors are listed in **Table IV** under the column heading of “after parameter optimization”.

With the above results, we obtained the final equation for the *SYI* calculation:

where T = translucency index, Wr = wrinkle score, P = pore score, b^* = yellowness, and U = color unevenness.

Using Equation 3 and the values of the objectively measured visual parameters of facial skin, we calculated *SYI* values from the

$$SYI = 10 \left(\frac{10 + (0.081 \ln T - 0.627 \ln Wr - 0.174 \ln P - 0.056 \ln b^* - 0.062 \ln U)}{\dots} \right)$$

Equation 3

images of all 1,505 study participants in the nine age groups indicated above. The average *SYI* value of each age group was correlated with the chronological age of the study participants, as shown by the solid dots and the regression line in **Figure 6** from which a strong inverse linear correlation was observed with $r^2 = 0.9959$. As expected, the younger groups have higher *SYI* values while the opposite holds true for the older groups.

The correlation in **Figure 6** enables us to calculate a person’s apparent age based on the visual parameters objectively measured from her facial images. By apparent age we mean the age of skin which has visual properties of the facial skin of people in that specific age group. This age might be different from the perceived age, as the latter is subjective in nature and strongly influenced by the perceiver’s knowledge, experience, preference, and cultural background. Therefore, when we use Equation 3 to predict a person’s age based on the measured visual parameters of facial skin, we say the subject exhibits a skin age similar to those people who typically possess the same level of visual properties. Higher levels of skin aging parameters shown in the facial images would result in lower *SYI* values, which would correspond to a higher apparent age.

Figure 7 shows the normalized *SYI* distributions for each of the nine age groups. The *SYI* values for all 1505 participants ranged approximately from 44 to 91, with higher values corresponding to a more youthful skin.

Table VI: p-Values of *SYI* Between Various Age Groups

Age (N)	20 (156)	25 (275)	30 (201)	35 (194)	40 (175)	45 (135)	50 (100)	55 (162)	60 (107)
20	NA								
25	<0.01	NA							
30	<0.01	0.012	NA						
35	<0.01	<0.01	<0.01	NA					
40	<0.01	<0.01	<0.01	<0.01	NA				
45	<0.01	<0.01	<0.01	<0.01	0.526	NA			
50	<0.01	<0.01	<0.01	<0.01	<0.01	<0.01	NA		
55	<0.01	<0.01	<0.01	<0.01	<0.01	<0.01	<0.01	NA	
60	<0.01	<0.01	<0.01	<0.01	<0.01	<0.01	<0.01	0.345	NA

From these plots we can see the *SYI*s for the 20-year-old group reside in the high value region. With an increase in group age, the *SYI* distributions shifted toward the lower value region, diminishing the peak value from 72 to 53. These distribution curves show how people’s *SYI*, as well as their exhibited visual properties of facial skin, change with age.

ANOVA/Tukey-Kramer tests were performed to identify significant differences in *SYI* distributions between the different age groups. The differences in *SYI* values between any two adjacent age groups were statistically significant at a 95% confidence level except those between the 40 and 45 and the 55 and 60 age groups, as shown by the p values in **Table VI**. Since we selected study participants who are at the same exact age (or almost same exact age) for each of the nine age groups indicated above, the results of these comparisons became meaningful. For example, from **Table VI** we can say with confidence that the skin’s visual properties and its youthfulness index are statistically different between people 20 and 25 years old. They are now measurable and distinctive properties of skin.

Validation

To validate the age predictability of Equation 3, we selected two new data sets from a Southeast Asian population. Facial images of 104 female volunteers 28 years of age and 70 females 38 years of age were analyzed. The five visual parameters were measured and inserted into Equation 3 along with their corresponding weight factors shown in **Table IV**. The resulting *SYI*s are shown by the hollow square and triangle, respectively, in **Figure 6**. While both of the validating data points fit into the model well, the average value of *SYI* for the 38-year-old group lies almost right on the regression line suggesting an excellent model for this analysis.

Age prediction using measured visual parameters of skin

From the results of these analyses we were able to calculate skin age using the objectively measured visual parameters of facial skin. This was done by replottting the data in **Figure 6** to show a dependence of age on *SYI*. Fitting the correlation to a linear model, we obtained the following relation for the prediction of a person’s apparent age:

where *SYI*= skin youthfulness index calculated from Equation 3, and Age= apparent age of any study participant.

By inserting the average *SYI* values into the equation we were able to calculate the average age of the nine age groups. **Figure 8** is a correlation plot in which the predicted ages are plotted against the actual ages of the nine test groups. An excellent correlation

$$Age = 194.38 - 2.26SYI \quad \text{Equation 4}$$

was obtained with RSS= 6.07. Comparing the result of this age correlation with that of the multivariate regression analysis (**Figure 3**), we can see that the *SYI* method is much more effective at predicting the skin age of the population in this study than the conventional multiple regression method. The maximum age deviation between the predicted and the actual ages was 1.3 years, much smaller than the 8.0 years from the multiple regression method for the same population.

The results from the *SYI* analysis also show a good age correlation and can be used for meaningful age prediction. Using the data from the 28 and 38-year-old age groups used for model validation, we calculated the apparent ages to be 25.6 and 38.9, respectively. As indicated in **Figure 8**, the differences of 2.4 and 0.9 years between the actual and the calculated ages for the 28 and 38-year-old

age groups, respectively, suggest a fairly good age prediction capability.

Concept application

The SYI-age correlation described in this study may provide a useful method for the evaluation of skincare product efficacy. For any given clinical study, we would be able to analyze both before and after clinical images to objectively measure the five visual parameters. If a product or skincare regimen were to demonstrate a skin benefit, such as wrinkle reduction or increase in skin translucency, it would be detected by image analysis and show a positive change in the corresponding measurement results. When the improved values are inserted into Equation 3, the corresponding SYI value would show an increase as seen in **Figure 6**. This increase in SYI would correspond to a skin property of people of a younger age group, i.e., a decrease in calculated skin age. Since all measured parameters are the visual properties of facial skin, this decrease in calculated skin age after product treatment could be used to support a claim that the facial skin of an individual appeared measurably years younger after product use. Our preliminary analysis of images before and after a laser resurfacing procedure indicated a very promising reduction in the calculated age after treatment (unpublished data).

CONCLUSIONS

The large number of facial images obtained from Asian female consumers through the Amway-exclusive F.A.C.E.S. program allowed us to objectively measure ten different visual properties of facial skin in nine age groups. A statistically significant age correlation was obtained for each of the measured visual parameters of skin. Combining the objectively measured parameters into a single function enabled us to establish a novel index of skin youthfulness (SYI), which quantitatively describes the aging of facial skin. An excellent correlation was obtained between age and SYI, providing a potentially useful application to establish skin product efficacy and substantiate new product claims.

Acknowledgements

We thank the staff of Amway F.A.C.E.S. System implementing group for their effort in establishing and maintaining the global infrastructure of this image collecting program. We appreciate Ms. Valentina Kazlova's guidance on statistical analysis, and Mr. Brad Richardson's effort in data mining. We also extend our thanks to Dr. Gopa Majmudar, Dr. Rong Kong, and Ms. Barbara Olson for the

critical reading and editing of this manuscript.

REFERENCES:

- [1] Yaar, M., *Clinical and Histological Features of Intrinsic Versus Extrinsic skin Aging*, in: Gilchrest, B. A. and Krutmann, J. (Eds.), *Skin Aging*, Springer, Berlin, Heidelberg, 2006, pp. 9-21.
- [2] Lange, N., and Weinstock, M., *Statistical Analysis of Sensitivity, Specificity, and Predictive Value of a Diagnostic Test*, in: Serup, J., Jemec, G., and Grove, G. L. (Eds.), *Handbook of Non-Invasive Methods and the Skin*, CRC Press, 2006, 2nd Edition, pp. 53-62.
- [3] Guinot, C., Malvy, D.J., Ambroisine, L., Latreille, J., Mauger, E., Tenenhaus, M., Morizot, F., Lopez, S., Le Fur, I., and Tschachler, E., *Relative Contribution of Intrinsic vs Extrinsic Factors to Skin Aging as Determined by a Validated Skin Age Score*, *Arch. Dermatol.*, 138 (2002) 1454-1460.
- [4] Vierkotter, A., Ranft, U., Kramer, U., Sugiri, D., Reimann, V., and Krutmann, J., *The SCINEXA: A Novel, Validated Score to Simultaneously Assess and Differentiate Between Intrinsic and Extrinsic Skin Ageing*, *J. Dermatol. Sci.*, 53 (2009) 207-211.
- [5] Nkengne, A., Roure, R., Rossi, A.B., and Bertin, C., *The Skin Aging Index: a New Approach for Documenting Anti-aging Products or Procedures*, *Skin Res. Technol.*, 19 (2013) 291-298.
- [6] Bazin, R. and Doublet, E., *Skin Aging Atlas, Volume 1 Caucasian Type*, Editions Med'Com, Paris, 2007, pp. 32.
- [7] Bazin, R., and Flament, F., *Skin Aging Atlas Volume 2 Asian Type*, Editions Med'Com, Paris, 2010, pp. 26.
- [8] Zedayko, T., Azriel, M., and Kollias, N., *Caucasian Facial L* Shifts May Communicate Anti-Ageing Efficacy*, *Int. J. Cosmet. Sci.*, 33 (2011) 450-454.
- [9] D. Dicario, D., R. Sparacio, R., L. Declercq, L., H. Corstjens, H., N. Muizzuddin, N., J. Hirdalgo, J., P. Giacomoni, P., L. Jorgensen, L., and D. Maes, D., *Calculation of apparent age by liner combination of facial skin param-*

ters: a predictive tool to evaluate the efficacy of cosmetic treatments and to assess the predisposition to accelerated aging, *Biogerontology*, 10 (2009) 757-772.

- [10] Kollias, N., Gillies, R., Moran, M., Kochevar, I.E., and Anderson, R.R., *Endogenous Skin Fluorescence Includes Bands that May Serve as Quantitative Markers of Aging and Photoaging*, *J. Invest. Dermatol.*, 111 (1998) 776-780.
- [11] Maillard-Lefebvre, H., Boulanger, E., Daroux, M., Gaxatte, C., Hudson, B.I., and Lambert, M., *Soluble Receptor for Advanced Glycation End Products: a New Biomarker in Diagnosis and Prognosis of Chronic Inflammatory Diseases*, *Rheumatology*, 48 (2009) 1190-1196.
- [12] Hawkins, S., *Computerized Image Analysis of Clinical Photos*, in: Serup, J., Jemec, G., and Grove, G. L. (Eds.), *Handbook of Non-Invasive Methods and the Skin*, CRC Press, 2006, 2nd Edition, pp. 95-100.
- [13] Matsubara, A., *Differences in the Surface and Subsurface Reflection Characteristics of Facial Skin by Age Group*, *Skin Res. Technol.*, 18 (2012) 29-35.
- [14] Weathington, B., Cunningham, C., and Pittenger, D. (Eds.), *Understanding Business Research*, John Wiley & Sons, Inc, Hoboken, New Jersey, 2012, pp. 245-270.
- [15] R. Bazin, and F. Flament, *Skin Aging Atlas Volume 2 Asian Type*, Paris: Editions Med'Com, 2010, pp. 28.

Corresponding author - email:
Di.Qu@amway.com

Preservation of Sympathetic Neuron-Adipocyte Crosstalk May Limit Chronic Emotional Stress-Mediated Fat Accumulation

Pascale Prouheze, Barbara Morand, Jean-François Nicolaÿ and Mathilde Fréchet
Exsymol S.A.M., 4 Av Albert II, 98000 Monaco

This publication was presented as a podium presentation at the 22nd IFSCC Conference, October 30 – November 01, 2013, Rio de Janeiro, Brazil.

Keywords: NGF, glucocorticoids, lipolysis, adipose tissue, sympathetic neurons

INTRODUCTION

While acute emotional stress enables appropriate response to a challenge, chronic emotional stress (from job strain, sleep deprivation, etc.) is noxious, driving metabolic imbalance (e.g., obesity) and diseases. One upstream key mediator of emotional stress is the glucocorticoid cortisol, the hormone of the hypothalamic-pituitary-adrenal axis. Cortisol has a dual effect on white adipose tissue, increasing energy expenditure on the one hand (fat mobilization) and dramatically boosting appetite and food intake on the other (fat storage). While acute levels of cortisol are catabolic, promoting energy substrate release (weight loss), sustained cortisol generated by chronic emotional stress was shown to promote anabolism in adipose tissue, in particular by promoting abdominal fat accumulation [1] and development of insulin resistance. Chronic cortisol anabolic action is also noticeable in Cushing syndrome patients with chronic high levels of cortisol associated with a central obesity phenotype [2]. Peripheral cortisol production may be involved, since overexpression of 11- β -hydroxysteroid dehydrogenase type 1 (11- β -HSD), an enzyme that catalyzes cortisol formation in adipocytes, correlates with central fat accumulation [3].

Some *in vitro* experiments have shown that cortisol impairs the viability of sympathetic nerves [4, 5]; it is thus possible that cortisol weakens brain – white adipose tissue nerve-borne communication. It is now well established that sympathetic innervation of adipose tissue plays an important role in the management of fat stores by delivering the white adipose tissue neuromediators (catecholamines, neuropeptide Y, ...) that modulate adipocyte metabolism [6]. Interestingly, *in vivo* surgical impairment of white adipose tissue innervation was shown to reduce lipolysis and promote fat accumulati-

ABSTRACT

Glucocorticoids, which are key actors during emotional stress, may behave as strong promoters of appetite and weight gain (mainly abdominal). Moreover, glucocorticoids may have a detrimental impact on the sympathetic innervation that is known to be involved in management of the body fat stores. Therefore, crosstalk between adipose tissue and the nervous system is of crucial importance for lipid mobilization. We observed that on the one hand glucocorticoids alter neuronal development, antagonizing neurotrophic properties of NGF, and on the other hand affect the neuroendocrine activity of adipocytes by decreasing NGF secretion and promoting adipogenesis. We set up a monocompartment co-culture system where adipocytes and neuronal cells are closely in contact in order to assess the effects of a glucocorticoid increase on this interplay. First, we show that lipolysis improvement is related to neuronal network development (a high neurotrophic supply correlates with more efficient lipolysis). Then, we show that increased exposure of this co-culture to glucocorticoids results in an altered neuronal network and decreased lipolysis. Pyroglutamylamidoethyl indole, a cosmetic ingredient endowed with neurotrophic properties and potentiating NGF signaling, proved to be effective in limiting the glucocorticoid-dependent lipolysis decrease.

on [7].

To test the hypothesis that sympathetic nerve alteration is involved in the chronic cortisol adipogenic effect, we have set up several *in vitro* models. To investigate the effect of cortisol on neurons, we used the PC12 neuronal cell line, which acquires the secretory

pattern of sympathetic neurons upon stimulation with the growth and survival factor nerve growth factor (NGF), and expresses the glucocorticoid type II receptor [6]. Consequences for adipocyte metabolism were assessed with PC12 neurons– 3T3-L1 adipocytes cell communication studies. Finally, a neuroprotective ingredient, pyroglutamylamidoethyl indole (pGT), able to enhance NGF signaling (“neurotrophic-like” effect), was evaluated in these models to test if neuroprotection can limit the adipogenic effect of cortisol.

EXPERIMENTAL

Cell cultures

Neuronal PC12 cells were isolated from a rat pheochromocytoma and are considered a well established model of sympathetic neurons [8]. They were grown in RPMI-1640 (Invitrogen, Carlsbad, CA, USA), 5% fetal calf serum (Invitrogen), 10% HS (Invitrogen) at 37°C/5% CO₂. For conditioned medium experiments, cells were differentiated using 70 ng/ml of NGF (Invitrogen). Murine 3T3-L1 pre-adipocyte cells, were grown in DMEM 4.5 g/l glucose (Invitrogen), 10% fetal calf serum at 37°C/5% CO₂ [9]. The differentiation process was induced on confluent pre-adipocytes for 13 days, according Green and Meuth [10] with slight modifications: phase 1: 3 days with IBMX (Sigma, St. Louis, MO, USA), dexamethasone (Sigma) and insulin (Sigma) followed by phase 2: 10 days with insulin.

Cortisol treatment of PC12 cells

Cells were incubated for 5 days in the presence of a low concentration of NGF (10 ng/ml) to induce differentiation. Cortisol (Sigma) 100 nM was added in the presence or absence of pyroglutamylamidoethyl indole [6]. At the end of the incubation period, the cells were fixed with 95% EtOH and 5% acetic acid for

10 min at -20°C. Cells were then incubated with the primary antibody β -tubulin (Sigma) followed by incubation with the labeled secondary antibody Alexa Fluor 488 (Invitrogen).

Cortisol treatment of adipocytes

3T3-L1 cells were differentiated into mature adipocytes as described before in absence or presence of cortisol during phase 2. Phase-contrast photographs of the cells were acquired on day 13.

Quantification of NGF secretion

3T3-L1 cells were differentiated into mature adipocytes over 13 days and treated with cortisol for 24 h. NGF secretion was assessed by ELISA (NGF Emax Immunoassay System, Promega, Madison, WI, USA).

Lipolysis assessment

Conditioned media experiments

PC12 cells media of a “weakly or highly developed” neuritic network were harvested and added to mature adipocytes. Glycerol release was assessed by ELISA assay 3 days after lipolysis induction.

Monocompartment co-cultures

PC12 cells were seeded on 3T3-L1 adipocytes 3 days after the beginning of differentiation. A low concentration of NGF (10ng/ml) was added to improve neuronal development and cortisol or pGT were added as indicated the **scheme**. Basal lipolysis was measured 3 days after removal of insulin and washing the cells from any treatment. Glycerol release was quantified using the Adipocyte Lipolysis Assay kit for 3T3-L1 (ZenBio, Research Triangle Park, NC, USA).

RESULTS

Neuron to adipocyte cell communication test system

In a first set of experiments, we examined the effect of PC12 neuroendocrine activity on the adipocyte metabolic activity of white adipose tissue. A cell communication test system was set up where culture media collected from PC12 cells (“conditioned” media) were added to mature adipocytes (differentiated 3T3-L1 adipocytes). The adipocyte lipolytic activity was then assessed by the dosage of the amount of glycerol released in the culture media. As expected, lipolysis was enhanced in mature 3T3-L1 adipocytes exposed to the “conditioned medium” from PC12 cells (**Figure 1**). We noticed that the lipolysis increase was proportional to neuritic network

Scheme

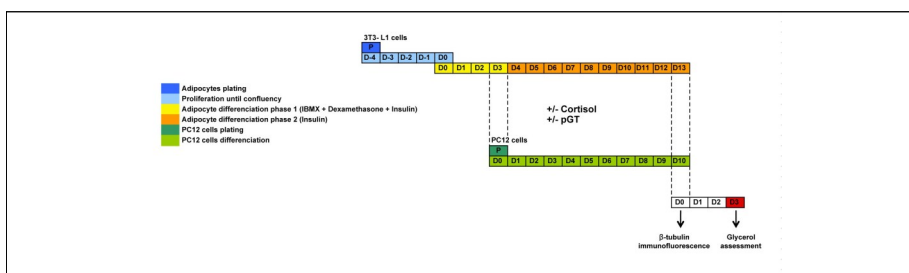
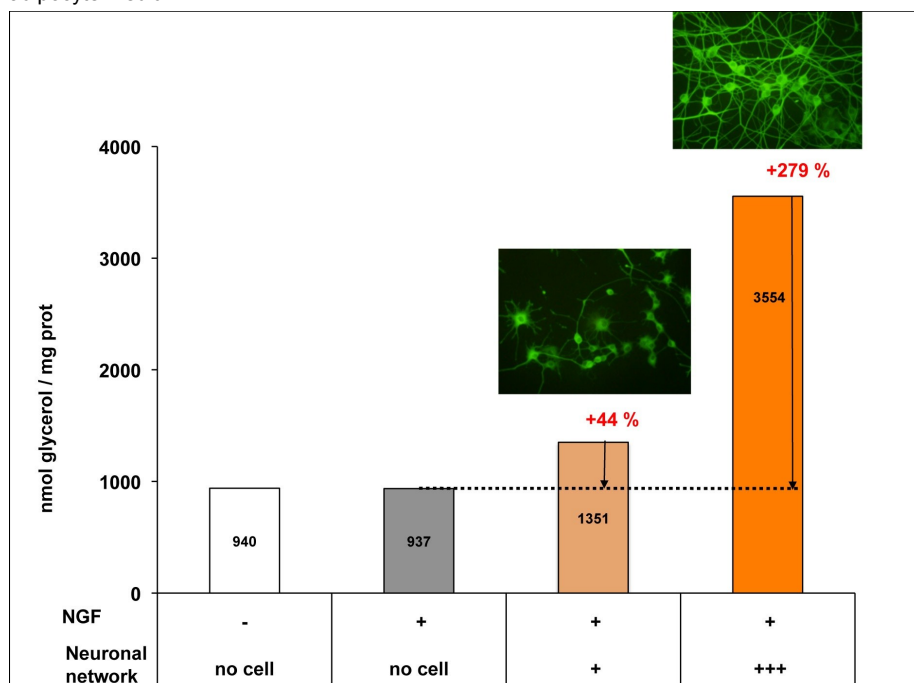


Figure 1: PC12 cell-conditioned medium increases lipolysis. β -tubulin immunofluorescence on PC12 cell cultures. Lipolysis is assessed by the dosage of glycerol released in mature 3T3-L1 adipocyte medium.



development (**Figure 1**). The higher the dose of NGF is, the higher the neuronal development, and lipolysis induction (**Figure 1**). We obtained some evidence that norepinephrine, a potent β -adrenergic agonist, is one of the lipolytic effectors released by PC12 cells, but we cannot rule out that other factors are involved.

Bidirectional cell communication test system

In white adipose tissue, innervation is maintained by the host tissue, e.g. adipocytes produce growth factors, in particular neurotrophins, that act directly on neurons to support their growth, metabolic activity and survival. Among those factors involved in sympathetic innervation development and maintenance is the neurotrophin NGF [11]. Its direct involvement was shown by injecting NGF antibodies into perinatal mammals, resulting in complete destruction of peripheral sympathetic and sensory neurons [12].

To study this important dialog between white adipose tissue and nervous endings, we designed a co-culture system where mature

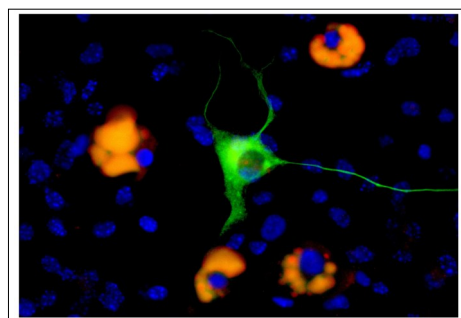


Figure 2: Sympathetic neuron-adipocyte co-culture. PC12 neuronal cells (stained in green: β -tubulin) differentiate in the presence of mature adipocytes (staining of lipid droplet in orange with Nile red). Cell nuclei are stained in blue (DAPI).

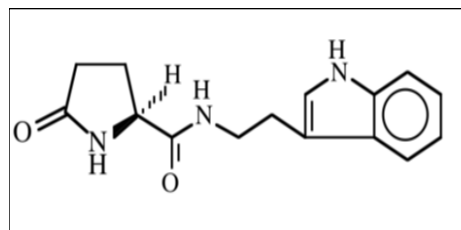


Figure 3: Chemical structure of the neuro-protective molecule pyroglutamylamidoethyl indole (pGT).

adipocytes loaded with lipids (fully differentiated 3T3-L1 cells) produce the survival and growth factors (chiefly NGF) that enable neuron (PC12 cell line) development and survival (production of nerve extensions) (Figure 2).

In this test system, there is bidirectional adipose – neuronal cell communication, and endocrine activity of the neurons may modulate adipocyte metabolism. We evaluated the effect of a specific molecule, pGT (Figure 3), which potentiates NGF signaling and neurotrophic support [13].

We found that lipolysis increased with the addition of increasing concentrations of pGT, as evidenced by increasing amounts of glycerol in the co-culture medium (Figure 4). This supports the hypothesis that improved survival and metabolic activity of the sympathetic neurons to adipose tissue increases the so-called “sympathetic lipolytic drive”.

Effect of cortisol on neurons

When cortisol was added to PC12 cells culture media we found that it was neurotoxic at relatively low doses, and that at non-cytotoxic concentrations cortisol could antagonize the effect of NGF, inhibiting neuritic network development (Figure 5B). Addition of pGT limited the deleterious effects of cortisol on neuronal network formation dose dependently (Figure 5C, 5D).

Effect of cortisol on pre-adipocyte differentiation into mature adipocytes

In a separate set of experiments, we analyzed the direct effect of cortisol on adipogenesis. Under our conditions, cortisol stimulated 3T3-L1 pre-adipocyte differentiation, resulting in a greater number of mature adipocytes (hyperplasia). Lipid droplets were smaller but more adipocytes seem to present these droplets (Figure 6), which is in agreement with the *in vivo* observation in the presence of elevated cortisol levels [14]. Regarding cortisol-induced lipolysis, we observed no significant increase in basal lipolysis for cortisol-treated adipocytes (data not shown).

Effect of cortisol on NGF support of neurons

Addition of cortisol to mature 3T3-L1 adipocytes decreases their NGF production (Figure 7). The same result was obtained when 3T3-L1 pre-adipocytes were exposed to cortisol (data not shown). These data suggest that the local supply of NGF provided by white adipose tissue adipocytes may be altered in response to emotional stress, and thus sympathetic nerve endings may be deprived of survival factors locally.

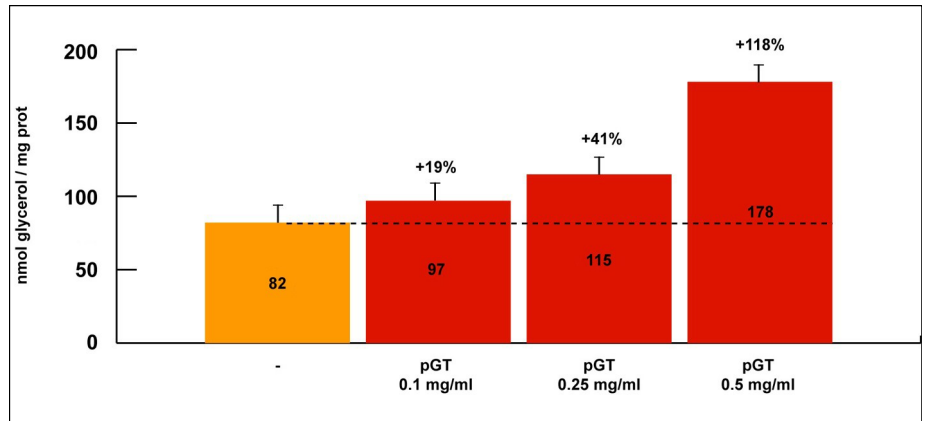


Figure 4: pGT improves PC12 cell-induced lipolysis in a adipocyte – neuron co-culture system. Evaluation of lipolysis by the amount of glycerol released into the co-culture medium.

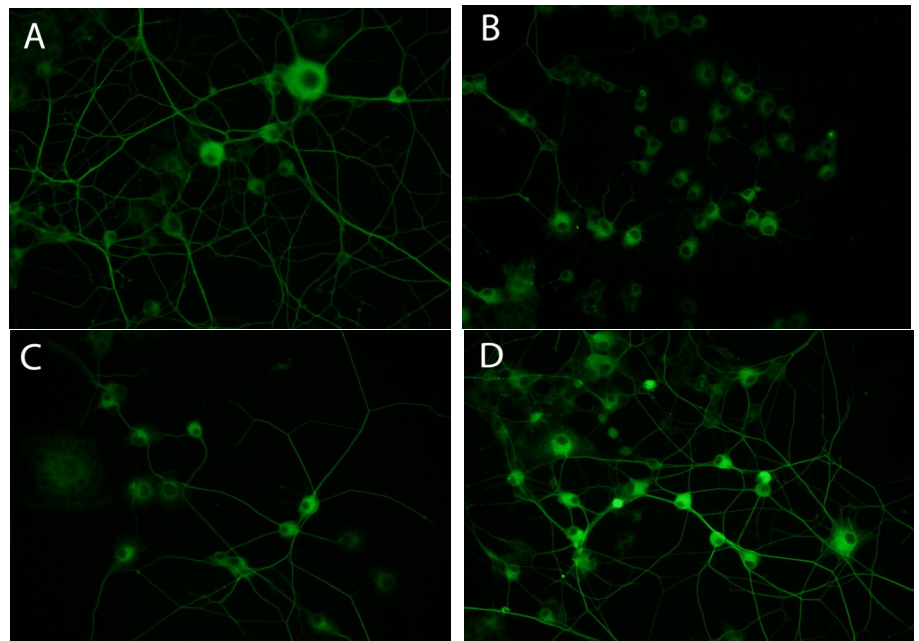


Figure 5: Reversal of the NGF-antagonizing effect of cortisol by pGT. β -Tubulin immunofluorescent staining (green) of PC12 cells; A) control cells with NGF (10 ng/ml), B) cells with NGF (10 ng/ml) + cortisol (100 nM), C) cells with NGF (10 ng/ml) + cortisol (100 nM) + pGT (0.25 mg/ml), D) cells with NGF (10 ng/ml) + cortisol (100 nM) + pGT (0.5 mg/ml).

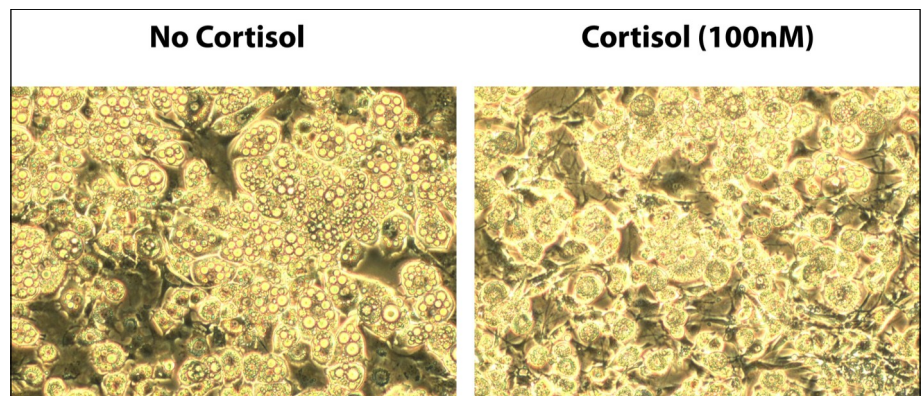


Figure 6: Effect of cortisol on pre-adipocyte differentiation. 3T3-L1 cells were differentiated into mature adipocytes over 13 days in the absence or presence of cortisol

Effect of cortisol on neuron – adipocyte crosstalk

To confirm that cortisol affects neuronal-adipocyte crosstalk, it was added to our *in vitro* monocompartment co-culture system where PC12 cells are seeded in contact with differentiated adipocytes. After 10 days of co-culture in the presence of cortisol, strong inhibition of neuritic network formation was noticeable (Figure 8) indicating that cortisol affects neurotrophic signaling by decreasing supply of NGF by adipocytes and antagonizing its effect on neuronal cells.

Figure 7: Effect of cortisol on NGF secretion by adipocytes. Monitoring of NGF released into the culture medium of 3T3-L1 mature adipocytes exposed to non-cytotoxic amounts of cortisol.

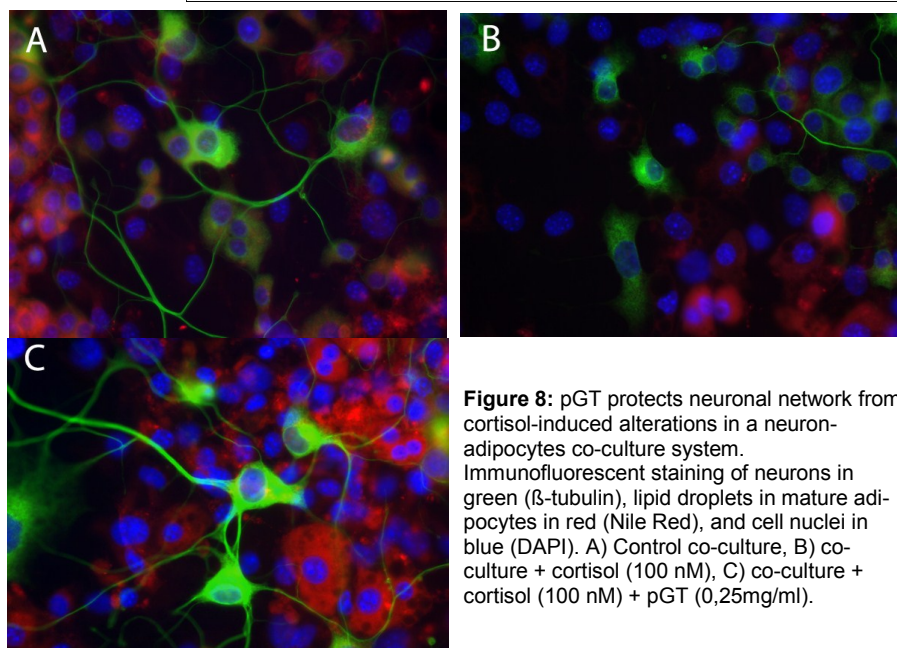
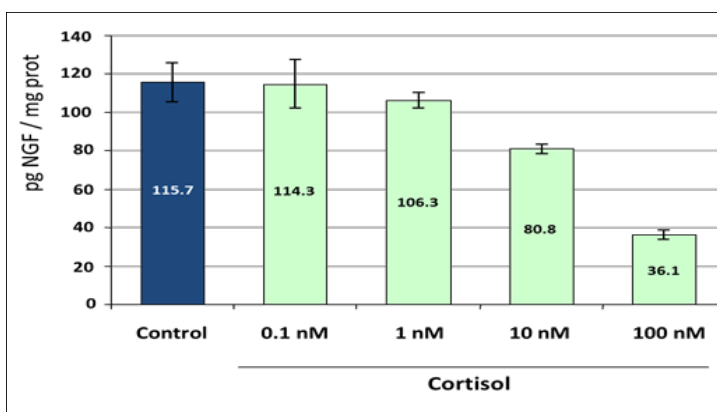
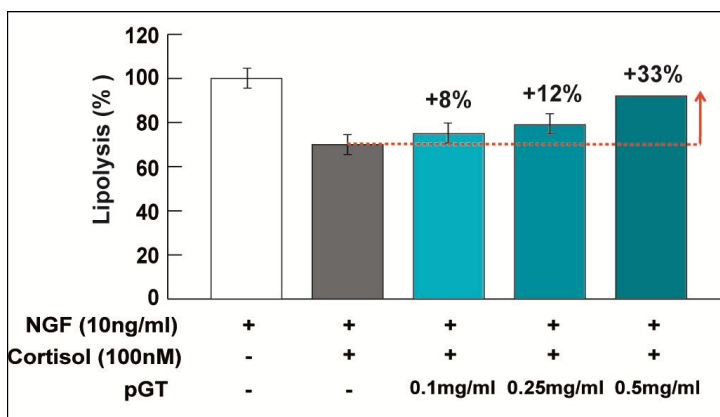


Figure 8: pGT protects neuronal network from cortisol-induced alterations in a neuron-adipocytes co-culture system. Immunofluorescent staining of neurons in green (β -tubulin), lipid droplets in mature adipocytes in red (Nile Red), and cell nuclei in blue (DAPI). A) Control co-culture, B) co-culture + cortisol (100 nM), C) co-culture + cortisol (100 nM) + pGT (0,25mg/ml).

Figure 9: pGT limits cortisol negative impact on lipolysis in a neuron-adipocyte co-culture system. Lipolysis is assessed by monitoring the amount of glycerol released in the medium of the co-culture.



In line with our findings with monocompartment co-cultures, glycerol quantification revealed that basal lipolysis was less efficient when the co-culture was « stressed » with cortisol (Figure 9). Addition of pGT to the co-culture medium could limit the effects of cortisol. Neurotrophic support was preserved, as evidenced by a well-developed neuritic network (Figure 8), and lipolysis improved (Figure 9).

CONCLUSION

We obtained a set of coherent experimental results showing that cortisol, the central messenger of chronic stress, opposes fat mobilization and stimulates adipogenesis, which echoes a number of clinical reports on the consequences of chronic emotional stress on body fat accumulation and distribution. Our results support the hypothesis that cortisol-induced impairment of white adipose tissue innervation contributes significantly to its effects on fat accumulation, and that “neurotrophic support”, e.g. local protection of white adipose tissue sympathetic nerve endings, may bring some appreciable benefits. We could show that a cosmetic ingredient (pGT) can protect sympathetic innervation of white adipose tissue locally from chronic cortisol-induced damage, and therefore might limit metabolic imbalance and fat accumulation caused by chronic emotional stress.

REFERENCES

- [1] Epel, E.S., McEwen, B., Seeman, T., Matthews, K., Castellazzo, G., Brownell, K.D., Bell, J., and Ickovics, R.I., *Stress and body shape: stress-induced cortisol secretion is consistently greater among women with central fat*, *Psychosomatic Med.*, 62 (2000) 623-632.
- [2] Bose, M., Oliván, B., and Laferrère, B., *Stress and obesity: the role of the hypothalamic-pituitary-adrenal axis in metabolic disease*, *Curr. Opin. Endocrinol. Diabetes Obes.*, 16 (2009) 340–346.
- [3] Masuzaki, H., Paterson, J., Shinyama, H., Morton, N.M., Mullins, J.J., Seckl, J.R., and Flier, J.S., *A transgenic model of visceral obesity and the metabolic syndrome*, *Science*, 294 (2001) 2166 –2170.
- [4] Kasai, M., and Yamashita, H., *Cortisol suppresses noradrenaline-induced excitatory responses of neurons in the paraventricular nucleus: an in vitro study*, *Neurosci. Letter*, 91 (1988) 65-70.
- [5] Lecht, S., Arien-Zakay, H., Tabakman, R., Jiang, H., Fink, D.W., and Lazarovici, P., *Dexamethasone-induced down-regulation of NGF receptor p75NTR is mediated by glucocorticoid type II receptor in PC12 cell model*, *The Open Pharmacology Journal*, 1 (2007) 19-26.
- [6] Bradley, R.L., Mansfield, J.P.R., and Mara-



tos-Flier, E., *Neuropeptides, including neuropeptides Y and melanocortins, mediate lipolysis in murine adipocytes*, *Obesity Research*, 13 (2005) 653-661.

[7] Bartness, T.J., and Song, C.K., *Brain-adipose tissue neural crosstalk*, *Physiol. Behav.*, 91 (2007) 343-351.

[8] Greene, L.A., and Tischler, A.S., *Establishment of a noradrenergic clonal line of rat adrenal pheochromocytoma cells which respond to NGF*, *Proc. Natl. Acad. Sci. USA*, 73 (1976) 2424-2428.

[9] Green, H., and Kehinde, O., *Sublines of mouse 3T3 cells that accumulate lipid*, *Cell*, 1 (1974) 113-116

[10] Green, H., and Meuth, M., *An established*

pre-adipose cell line and its differentiation in culture, *Cell*, 3 (1974) 127-133.

[11] Peeraully, M.R., Jenkins, J.R., and Trayhurn, P., *NGF gene expression and secretion in white adipose tissue: regulation in 3T3-L1 adipocytes by hormones and inflammatory cytokines*, *Am. J. Physiol. Endocrinol. Metab.*, 287 (2004) E331-E339.

[12] Aloe, L., Cozzari, P., Calissano, P., and Levi-Montalcini, R., *Somatic and behavioural postnatal effects of fetal injections of NGF antibodies in the rat*, *Nature*, 291, 413-415.

[13] Nicolay, J.-F., and Frechet, M., *Renforcer les défenses antimicrobiennes de la peau*, *Expression Cosmétique, Hors-série Guide des ingrédients*, Décembre 2013.

[14] Campbell, J.E., Peckett, A.J., D'souza, A.M., Hawke, T.J., and Riddell, M.C., *Adipogenic and lipolytic effects of chronic glucocorticoid exposure*, *Am. J. Physiol. Cell Physiol.*, 300 (2011) C198-209.

Corresponding author - email:
mfrechet@exsymol.com

Development of a Water-Based Long-Lasting Makeup: Dispersion of Hydrophobically Surface-Treated Pigments in an Oil-In-Water Emulsion

E. Akiyama¹, Y. Yago¹, K. Fukuda²

¹Makeup Products Research Laboratory, Kao Corporation., 2-1-3, Bunka, Sumida-ku, Tokyo, Japan 131-8501

²Skin Care Products Research Laboratory, Kao Corporation., 2-1-3, Bunka, Sumida-ku, Tokyo, Japan 131-8501

This paper was presented as a podium presentation at the 22nd IFSCC Conference, 30th Oct. -1st Nov., 2013, in Rio de Janeiro, Brazil.

Keywords: Makeup, long-lasting, O/W emulsion, amphiphilic polymer, hydrophobically surface-treated pigment

INTRODUCTION

Liquid-type base makeup products such as liquid foundations, makeup bases and sunscreens are required to not only conceal skin imperfections but also provide long-lasting performance. The ingredients of liquid-type base makeup cosmetics include water, oil, pigment, surfactant and polymer. With pigments like titanium dioxide, iron oxide and zinc oxide hydrophobic surface-treatment is preferable because it gives water-repellency and provides a strong makeup film against sweat. Hydrophobically surface-treated pigments easily disperse into oil and are usually used in water-in-oil (W/O) emulsions (**Figure 1(a)**). However, conventional W/O type cosmetics containing a large amount of oil feel greasy when applied to the skin. The O/W type is generally superior in smoothness and freshness at the first touch of application.

If hydrophobically surface-treated pigments can be dispersed sufficiently in oil-in-water (O/W) emulsions, a fresh feel and water resistance can be obtained at the same time. Hydrophobically surface-treated pigments have a low affinity to water and need a large amount of hydrophilic surfactant to disperse in water adequately. However, hydrophilic surfactants in emulsions cause makeup to come off on the skin due to a re-emulsification by sweat. Therefore, use of hydrophilic surfactants should be avoided.

Without hydrophilic surfactants, hydrophobically surface-treated pigments tend to exist in the oil phase as a suspension. If the hydrophobicity, aggregability and/or specific gravity of the disperse phase is high (these depend on the composition), fine and stable O/W emulsions like those shown in **Figure 1(b)** are difficult to obtain. Highly effective interfacial and rheological stabilization mechanisms are needed. In today's market, most of the O/W emulsions containing pigments include hydrophilic surfactants. Although the stability of these emulsions is adequate, their water-repellency is poor.

Thickening polymers are effective for rheological modification of the continuous phase in emulsions and used as a stabilizer. Water-soluble thickening agents can reduce the amount of hydrophilic surfactant in O/W emulsions. However, their ability to decrease interfacial tension is low and this leads to large emulsified particles. Moreover, water-soluble thickening polymers such as polyacrylic acid lose their thickening ability when combined with zinc oxide pigments because the ions on the surface of zinc oxide pigments (cation) affect the carboxylic acid groups (anion) of the polymers and aggregates are formed [1, 2]. Therefore, an inventive approach is necessary in order to obtain high dispersibility and stability.

We directed our attention to salt-resistant hydrogels as an O/W type emulsifier and

ABSTRACT

Hydrophobically surface-treated pigments were dispersed and stabilized in O/W emulsions using a hydrogel-forming polymer, hydrophobically-hydrophilically modified hydroxyethylcellulose (HHM-HEC). Emulsion stability was obtained mainly with a thixotropic and elastic HHM-HEC hydrogel. Addition of a small amount of lipophilic surfactant improved the dispersibility of the emulsified particles. The salt resistance of HHM-HEC enabled formulation of zinc oxide microparticles which have an ultraviolet scattering effect.

Specific combinations of surface-treatment agents and oils created fine emulsions and offered functional performance. Use of fluorochemical surface treatment and fluorine oil provided sebum resistance, and use of alkylsilane surface treatment and ultraviolet-absorbing oils improved the dispersibility of emulsified particles in sunscreens.

These emulsions had both a fresh feel and long-lasting performance on the skin and could find practical application as base makeup cosmetics.

stabilizer, focusing on a hydrogel-forming agent, hydrophobically-hydrophilically modified hydroxyethylcellulose (HHM-HEC [3], INCI: Sodium Stearoyl PG-Hydroxyethylcellulose Sulfonate, **Figure 2**). HHM-HEC is an amphiphilic, strongly acidic polyelectro-

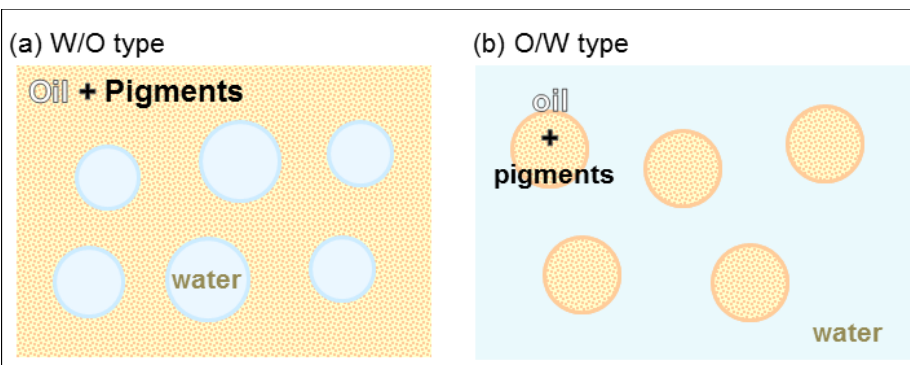


Figure 1: Emulsions including hydrophobically surface treated pigments

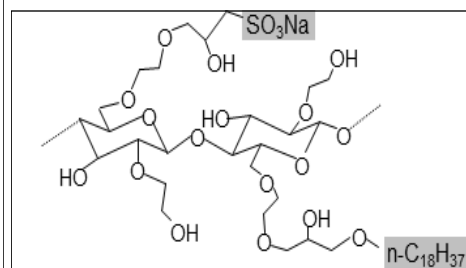


Figure 2: Structure of HHM-HEC

lyte with a high molecular weight that forms three-dimensional network structures in water and emulsifies various kinds of oil without using hydrophilic surfactant [4]. In this study we dispersed various kinds of hydrophobically surface-treated pigments in O/W emulsions using HHM-HEC. We also investigated the dispersibility and worked on improving performance by changing the agent used for surface-treatment of pigments. Finally, this system was then applied to actual products.

EXPERIMENTAL

Materials

Polymers: HHM-HEC (analytical grade) was synthesized at Kao Corporation, Tokyo, Japan [5]. HHM-HEC is a high molecular weight polysaccharide which introduces hydrophobic alkyl chains and hydrophilic sulfonate groups. Two types of HHM-HEC (Table I) were used. Thickening properties of these HHM-HECs are similar (Figure 3). HMPAA (hydrophobically modified polyacrylic acid, INCI: Acrylates/C10-30 Alkyl Acrylate Cross-polymer) was purchased from The Lubrizol Corporation, Ohio, USA.

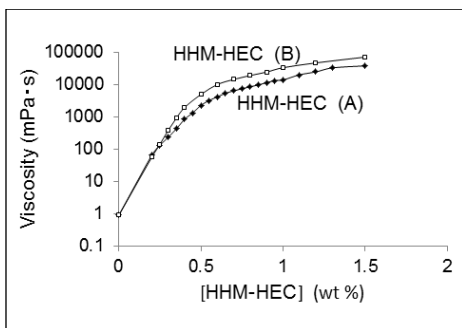


Figure 3: Thickening curves of HHM-HEC (A) and (B)

Oils: Squalane, dimethylpolysiloxane (viscosity: 6mm²/s (non-volatile) and 2mm²/s (volatile)), ethylhexyl methoxycinnamate, perfluoroalkylether silicone and perfluoropolymethylisopropyl ether were purchased from Kishimoto Special Liver Oil Co. Ltd., Tokyo, Japan, Shin-Etsu Chemical Co., Ltd., Tokyo, Japan, BASF SE, Ludwigshafen, Germany, Kao corporation, Tokyo, Japan and Solvay Solexis, Brussels, Belgium, respectively.

Hydrophobically surface-treated pigments: Metal oxide pigments (Table II) covered by each surface-treatment agent (N-octyltriethoxysilane [OTS], methylhydrogenpolysiloxane [SI] and perfluoroalcohol phosphates [PF]) were purchased from and supplied

by Daito Kasei Kogyo Co., Ltd., Osaka, Japan and Miyoshi Kasei Inc., Saitama, Japan. The surface structures of these pigments are listed in Table III [6]. The pigments were pulverized before use.

Surfactants: Isostearyl glyceryl ether (HLB=2.5) and polyoxyethylene (20) sorbitan monostearate (HLB=14.9) were supplied by Kao Corporation, Tokyo, Japan.

Methods

Preparation of emulsions: A mixture of oils, surfactants and pigments was dispersed with a high-speed disperser at 2500 rpm for 10 min. Then the mixture was added to an HHM-HEC aqueous solution with stirring with a propeller mixer (Three-one motor, SHINTO Scientific Co. Ltd., Tokyo, Japan) at 400 rpm for 5 min. After pre-mixing, the mixture was stirred with a laboratory homomixer (ROBOMICS f-model, PRIMIX, Osaka, Japan) at 5000 rpm for 10 min. The mixture was defoamed with a vacuum defoaming apparatus.

Viscosity measurements: Viscosity was measured with a viscometer (TVB-10, Rotor No. 3 and 4, 6 rpm, Toki-Sangyo, Tokyo, Japan).

Optical measurements: Photomicrographs of the emulsions were taken using a photomicroscope (VHX-2000, KEYENCE, Osaka, Japan).

SEM measurements: Cryo-SEM images of the emulsions were obtained with a scanning electron microscope (JSM 6301, JEOL Ltd., Tokyo, Japan). The sample was cooled to -150 °C and then fractured with a microtome knife. The samples were viewed after etching for 30 s - 1 min at -100 °C. The sample was also viewed with a low vacuum SEM (LV-SEM JSM-6610, JEOL Ltd., Tokyo, Japan).

Droplet size measurements: Droplet size distribution was determined using a laser scattering particle size distribution analyzer (LA-920, HORIBA Ltd., Kyoto, Japan)

Sample name	M _w	Hydrophobic modification (mol %)	Hydrophilic modification (mol %)
HHM-HEC(A)	1.7 × 10 ⁶	0.33	21
HHM-HEC(B)	1.2 × 10 ⁶	0.55	21

Table I: HHM-HEC samples used in this work

Name	Chemical composition	particle size (μm)	Remarks
Titanium dioxide	TiO ₂	0.25	Al ₂ O ₃ surface-treated
Iron oxide (red)	α-Fe ₂ O ₃	0.38 (colcothar)	: PF surface-treated
Iron oxide (yellow)	α-FeOOH	0.08 × 0.8	: Non-surface-treated, OTS, SI
Iron oxide (black)	Fe ₃ O ₄	0.07 × 0.7	
Zinc oxide	ZnO	0.2-0.6	
Zinc oxide (microparticle)	ZnO	0.25	
		0.020	

Table II: Metal oxide pigments used in this work

Name	OTS	SI	PF
Kind of surface-treatment	Alkylsilane	Silicone	Fluorochemical
Surface-treatment material	n-octyltriethoxysilane	Methylhydrogen polysiloxane	Perfluoroalcohol phosphates
Surface-structure			
Treatment ratio	2% (7%: zinc oxide [7] and zinc oxide (microparticle))	2% (6%: zinc oxide (microparticle))	5%

Table III: Kinds of surface treatment used in this work

Contact angle measurement: Samples were applied to polyurethane artificial skins (3 mg/cm²) and dried for 3 hours before measurement. The contact angles of water and squalane droplets were measured using a contact angle meter (CA-X, Kyowa Interface Science, Saitama, Japan). The contact angle value on the artificial skin was correlated with the value on bare skin.

Sedimentation velocity measurements: The suspension height in a glass tube was measured by an optical analyzer (TURBISCAN MA2000, Formal Action, L'Union, France). The rate of sedimentation per hour (%/hour) was calculated using the height values after two hours.

Wettability measurement: 0.1 g of pigments was put on the surface of 20 g of an acetone aqueous solution or an oil medium with stirring, and absorption of the pigments into the medium was observed. The solubility parameter (SP) of the pigment surface was calculated from an acetone concentration at which the pigments were absorbed and sank to the bottom according to the following formula [8].

$$SP = (23.3A + 9.75B) / (A + B)$$

(A is acetone volume (ml) and B is water volume (ml))

Rheological measurements: Rheological measurements were carried out using a rheometer (MCR301, Cone plate: D=50 mm, cone angle=2°, PHYSICA Messtechnik GmbH, Stuttgart, Germany) at 25°C.

SPF test: in vitro SPF testing was performed with a UV transmittance analyzer (UV-2000S, Labsphere, North Sutton, USA) based on ISO24443.

Sensory test: 15 trained panelists evaluated the feel of a prototype formula during application to the face.

Long-lasting effect test: A prototype formula and a commercial product were applied to the left and right side of a woman's face to give the same appearance. After 5 hours, 10 trained panelists evaluated the appearance of the makeup on the left and right.

Water-resistance test: In vitro SPF values were measured before and after immersion in water. Samples were applied to PMMA plates and the plates attached to a propeller and rotated in a 5 L water bath for 15 minutes at a speed of 150 rpm. After immersion the plate was dried for 15 minutes. [9]

RESULTS AND DISCUSSION

Formulation and stabilization with HHM-HEC

HHM-HEC forms a hydrogel by self-association of the alkyl chains in water. **Figure 4 (a) and (b)** show the elastic/viscous moduli and yield value of an aqueous solution of HHM-HEC(B) as a function of concentration. It changes from viscous fluid to elastic gel above 0.6 wt %. The yield value increased gradually.

SI surface-treated pigments (mixture of titanium dioxide, iron oxide and zinc oxide) were held at the interface or within silicone oil particles surrounded by HHM-HEC hydrogel (**Figure 5(a) and (b)**). Although the density of the emulsified droplets was high and they tended to sink, stable emulsions (stable for more than one month) were obtained in the concentration range above 0.6 wt % where an elastic network structure is formed (**Figure 6**).

The upper limit of the HHM-HEC concentration is about 1.0 wt% because, above this con-

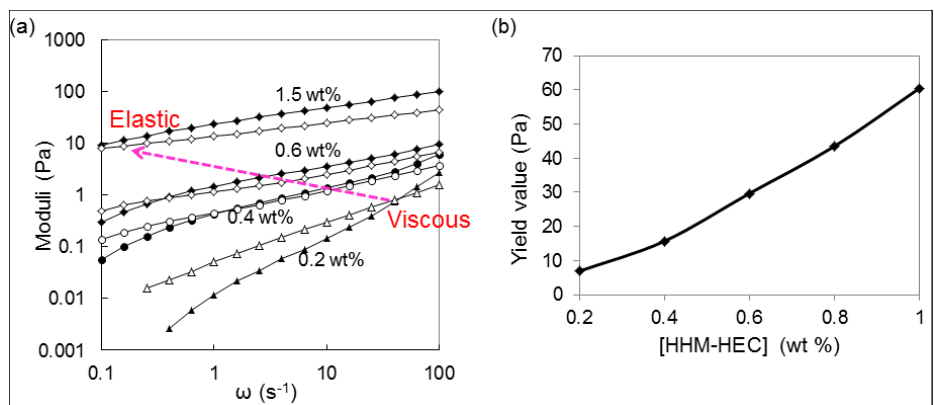


Figure 4: a) Dynamic frequency sweep at $\gamma=1\%$ (elastic modules = closed symbols, viscous modules = open symbols) and b) yield value of HHM-HEC(B) aqueous solution as a function of concentration

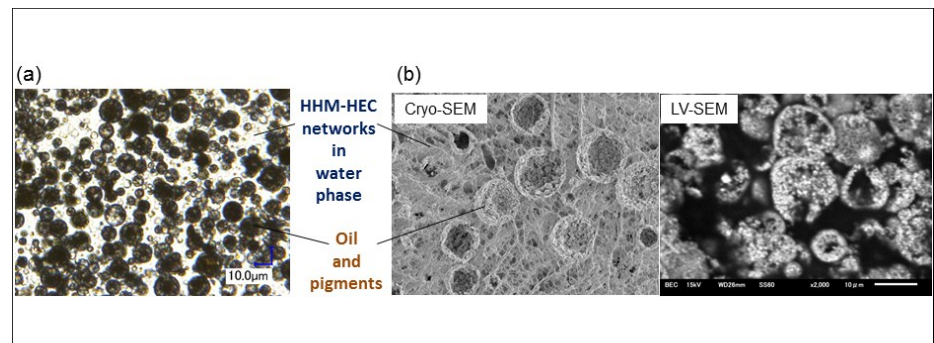


Figure 5: a) Photomicrograph and b) SEM images (Cryo-SEM, LV-SEM, x2000) of HHM-HEC o/w emulsion containing hydrophobically surface treated pigments. (HHM-HEC(B) 0.3wt%, dimethylpolysiloxane 10wt%, dimethylpolysiloxane (volatile) 10% and SI surface treated pigment (mixture of titanium dioxide, iron oxide and zinc oxide) 10wt%)

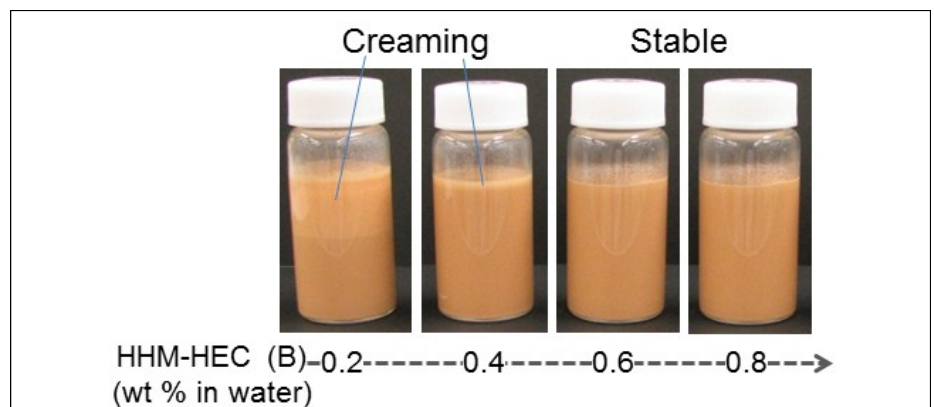


Figure 6: HHM-HEC emulsions at five days after preparation as a function of HHM-HEC concentration. (Dimethyl-polysiloxane 20wt% and SI surface treated pigments 10wt%)

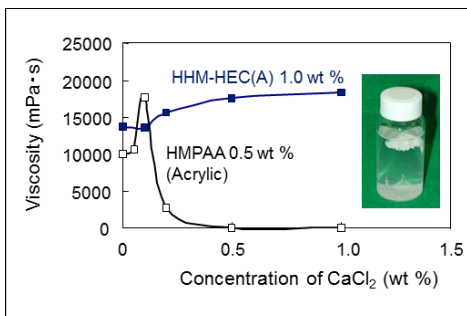


Figure 7: Effect of CaCl₂ concentration on viscosity of aqueous solutions of HHM-HEC(A) and HMPAA

centration, the texture of the emulsion becomes too thick to homogenize and apply to the skin.

The diameter of emulsified particles, including hydrophobically surface-treated pigments, was large (approximately 20 μm) and such an emulsion was inferior in appearance especially in the case of the highly colored emulsions. However, the particle size was remarkably reduced to <5μm by adding a small amount of lipophilic surfactant without phase inversion occurring. This phenomenon was explained in previous reports [10] as follows; “It is derived from the decrease of the interfacial tension between the oil droplets and water, and the gel structure of HHM-HEC in the continuous phase”. The lipophilic surfactant is limited to a low concentration in order to avoid a sticky feel.

Figure 7 shows the decrease in viscosity of an aqueous solution of acrylic polymer (HMPAA) with addition of a salt. In contrast, the associ-

Oil medium	Surface-treatment	OTS	SI	PF
Squalane		30.3	38.8	Separation
Dimethyl polysiloxane		37.5	41.6	Separation
Perfluoro alkylether silicone		0.8	0.5	0.0
Perfluoro polymethyl isopropyl ether		4.0	2.2	0.0

Table IV: Sedimentation rate (%/hour) of pigments in the dispersions of Fig. 8. (Dispersion: surface treated pigments (mixture of titanium dioxide, iron oxide, zinc oxide) in four kinds of oil. (5wt% pigments in oil medium))

ation of alkyl chains in HHM-HEC was slightly enhanced by addition of CaCl₂. HHM-HEC did not form aggregates with metal ions such as Ca²⁺ and Zn²⁺ even at high concentrations [11]. Therefore, the dispersion of pigments, particularly zinc oxide, became possible [12]. Microparticles of zinc oxide are effective in scattering ultraviolet rays.

Dispersibility and performance improvement by varying the surface-treatment agents

In O/W emulsions using HHM-HEC, hydrophobically surface-treated pigments exist in oil droplets. Sometimes the emulsions show aggregation of pigments and low dispersibility because the amounts of HHM-HEC (rheology modifier) and lipophilic surfactant (interfacial-tension effect) are limited. It depends on the kind, amount and composition of the pigments and oils. Therefore, different kinds of surface-treatment agents for pigments and oil were examined in order to improve the stability and homogeneity of the emulsions. Surface-treatment agents also

allowed more functional properties such as a long-lasting appearance and protection from ultraviolet rays.

Three types of surface-treated (OTS, SI and PF) pigments (mixture of titanium dioxide, iron oxide and zinc oxide) were dispersed in four kinds of oil (squalane, dimethylpolysiloxane, perfluoroalkylether silicone and perfluoropolymethylisopropyl ether). The dispersibility of pigments in these suspensions was visually evaluated and the sedimentation velocities were measured. The results are shown in **Figure 8** and **Table IV**. OTS and SI surface-treated pigments had higher dispersibility in squalane and dimethylpolysiloxane than PF surface-treated ones. The suspension of PF surface-treated pigments in fluorochemical oils (perfluoroalkylether silicone and perfluoropolymethylisopropyl ether) also showed high dispersibility [13]. Dispersibility is thought to be promoted when the affinity of pigments to oil is high.

Next, these combinations of oils and surface-treated pigments were emulsified in HHM-HEC hydrogels. Photomicrographs and the emulsified particle sizes of the emulsions are shown in **Figure 9**. The particle sizes were different among the kinds of oil depending on the interfacial tension between the oil and water. For the same type of oil highly dispersible surface-treated pigments gave finer O/W emulsions.

Table V compiles the skin feel on application and the stability of prototype makeup bases composed of a HHM-HEC O/W emulsion with specific combinations of surface-treated pigment and oil. The use of silicone oil was effective in providing a fresh and light feel. The combination of PF surface-treated pigments and perfluoropolymethylisopropyl ether caused sedimentation of emulsified particles because the specific gravity of the oil is high [14]. Thus, perfluoroalkylether silicone oil is better for actual use.

The water and oil repellency of these emulsions obtained with a contact angle measurement are shown in **Figure 10**. In the case of O/W type emulsions with non-surface-

Surface-treatment	OTS	SI	PF
Oil			
Squalane	Somewhat high	Somewhat high	Low (separation)
Dimethyl polysiloxane	High	High	Somewhat low
Perfluoroalkylether silicone	Somewhat high	High	High
Perfluoropolymethyl isopropyl ether	Neither high nor low	Somewhat low	High

Figure 8: Photomicrographs of a dispersion of surface treated pigments (mixture of titanium dioxide, iron oxide, zinc oxide) in four kinds of oil. (5wt% pigments in oil medium)

Surface-treatment	OTS		SI		PF	
Oil	Squalane	Dimethyl polysiloxane	Squalane	Dimethyl polysiloxane	Perfluoro alkylether silicone	Perfluoro polymethyl isopropyl ether
Sensory feeling of emulsion	Heavy	Light	Heavy	Light	Light	Light
Stability of emulsion	Stable	Stable	Stable	Stable	Stable	Creaming

Table V: Sensory feeling and stability of the prototype makeup bases composed of o/w emulsions using specific combinations of surface treatment agent and oil. (HHM-HEC 0.3wt%, oil 10wt%, dimethylpolysiloxane (volatile) 10wt%, isostearyl glyceryl ether 0.5wt%, hydrophobically surface treated pigments 10wt%)

	Titanium dioxide	Iron oxide (yellow)	Zinc oxide	Zinc oxide (microparticle)
OTS surface-treatment	15.1	3.6	5.1	2.9
SI surface-treatment	27.9	20.9	3.2	4.1

Table VI: Sedimentation rate (%/hour) of the particles in the dispersion of Fig. 11. (Dispersion: surface treated pigments (5wt%) in a mixture of ethylhexyl methoxycinnamate (24wt%) and dimethylpolysiloxane (71wt%))

	Titanium dioxide	Iron oxide (yellow)	Zinc oxide	Zinc oxide (microparticle)
OTS surface-treatment	15.8	16.6	14.5	15.8
SI surface-treatment	17.5	18.8	16.6	18.8

Table VII: Surface solubility parameter (SP) of the surface treated pigments

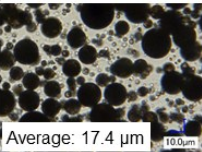
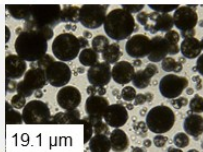
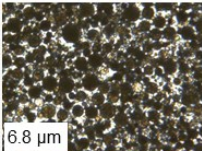
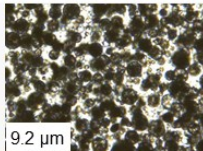
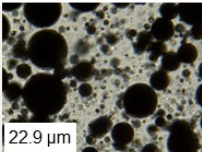
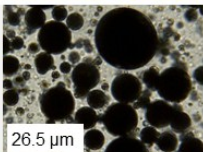
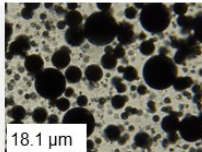
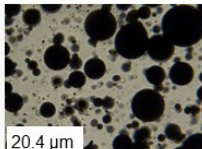
Surface-treatment	OTS	SI	PF
Oil			
Squalane			N/A (Disperse phase separated.)
Dimethyl polysiloxane			N/A (Disperse phase separated.)
Perfluoroalkylether silicone			
Perfluoropolymethyl isopropyl ether	N/A (Disperse phase was too thick to emulsify.)	N/A (Disperse phase was too thick to emulsify.)	

Figure 9: Photomicrographs of HHM-HEC o/w emulsions including hydrophobically surface treated pigments (HHM-HEC(B) 0.3wt%, oil 20wt% and surface treated pigments (mixture of titanium dioxide, iron oxide, zinc oxide) 10wt%)

treated pigments and 3.0% of the hydrophilic surfactant (polyoxyethylene (20) sorbitan monostearate (HLB=14.9)), the water repellency is 45 degrees. The HHM-HEC emulsion with a combination of SI surface treatment and dimethylpolysiloxane improved water repellency. The combination of PF surface treatment and a fluorochemical oil had high repellency against both water and oil. A sensory test of a fluorine-type HHM-HEC O/W liquid foundation clearly indicated the feel of an O/W emulsion (**Figure 11**). The test for a long-lasting effect revealed that the HHM-HEC O/W liquid foundation achieved the same level as a commercial long-lasting type W/O (fluorine type) liquid foundation (**Figure 12**).

To improve the product, a high degree of protection from ultraviolet rays was desirable. However, some ultraviolet-absorbing oils such as ethylhexyl methoxycinnamate are highly polar and cause a phase separation when mixed with silicone oils. Microphotographs of OTS and SI surface-treated pigments (titanium dioxide, iron oxide and zinc oxide) dispersed in a mixture of ethylhexyl methoxycinnamate and dimethylpolysiloxane are shown in **Figure 13**. The dispersibility of the OTS surface-treated pigments was better than the SI surface-treated pigments. SI surface-treated pigments seem to aggregate in the oil particles (ethylhexyl methoxycinnamate) or at the interface between ethylhexyl methoxycinnamate (particles) and dimethylpolysiloxane (outer phase). The sedimentation rates of the particles in these dispersions are listed in **Table VI**. However, they include an oil particle sedimentation rate and do not express pigment aggregability itself. Therefore we evaluated the dispersibility of pigments in immiscible oils only using the microphotographs. The difference in dispersibility between OTS and SI surface-treated pigments is considered to result from the wettability of the pigments because the aggregability of the dried pigments is almost the same.

The surface solubility parameters (SP) of these surface-treated pigments are listed in **Table VII**. These results indicate that OTS surface treatment is more hydrophobic than SI. Actually, OTS surface-treated pigments were absorbed into ethylhexyl methoxycinnamate (polar oil) more slowly than the SI surface-treated pigments. OTS surface-treated zinc oxide, the most hydrophobic (highly treated) of these pigments, is mainly dispersed in dimethylpolysiloxane and showed less aggregability in ethylhexyl methoxycinnamate. SI surface-treated pigments were less hydrophobic and wettable in both ethylhexyl methoxycinnamate and dimethylpolysiloxane and showed enhanced formati-

on of aggregates at the interface between oils.

In general, an alkyl moiety has a high affinity to hydrocarbon (nonpolar and polar) oils, and a silicone molecule has a high affinity to silicone oils and low affinity to polar oils. However, in this case SI surface-treated pigments showed higher wettability in ethylhexyl methoxycinnamate than OTS surface-treated pigments. This makes it unlikely that the difference in the wettability of these pigments is due solely to the kinds of surface-treatment material used and suggests that the wettability of these pigments is affected by the surface coverage or the surface roughness. In other words, either untreated surfaces remain on the pigments in the case of SI surface treatment or nanostructures formed by OTS surface treatment repel polar oils. The surface structure analysis is a subject for further investigation.

We prepared O/W emulsions including both dimethylpolysiloxane and ethylhexyl methoxycinnamate using HHM-HEC. The state of emulsions using the two types of surface-treatment agent is shown in Figure 14. When SI surface-treated pigments were used, the emulsion showed pigment aggregation and larger emulsified particles. On the other hand, OTS surface-treated pigments gave fine and even emulsions. The creaming level of the emulsions with OTS surface-treated pigments was lower than those with SI surface-treated pigments. These results demonstrate that high pigment dispersibility in an oil medium produces fine HHM-HEC O/W emulsions. The dispersibility is derived from the wettability of the pigments.

An in vitro SPF test was performed for the formula listed in Table VIII and the value measured was 22.7±2.2. The in vitro percent-

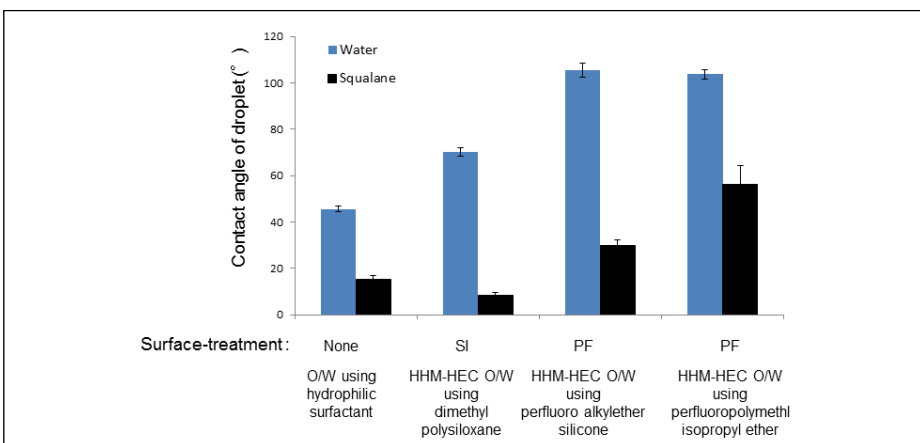


Figure 10: Water and oil (squalane) repellency test by measurement of contact angle. (HHM-HEC emulsions: HHM-HEC(B) 0.3wt%, oil 10wt%, dimethylpolysiloxane (volatile) 7wt%, isostearyl glyceryl ether 0.5wt%, surface treated pigments 15wt%)

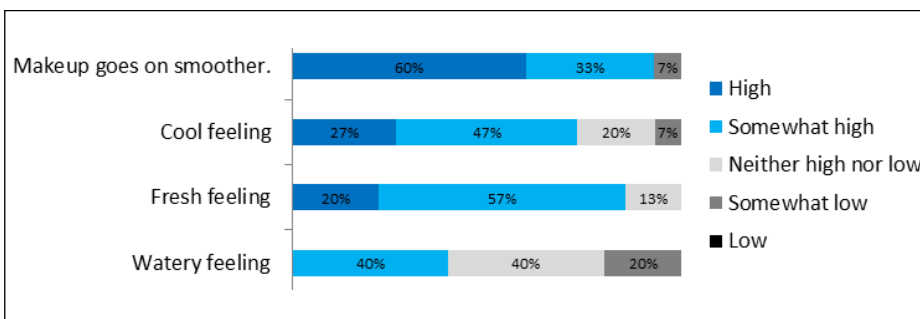


Figure 11: Sensory test of the prototype o/w (fluorine type) liquid foundation. (prototype o/w: HHM-HEC 0.3wt%, perfluoroalkylether silicone 10wt%, dimethylpolysiloxane (volatile) 20wt%, isostearyl glyceryl ether 0.7wt%, PF surface treated pigments 15wt%)

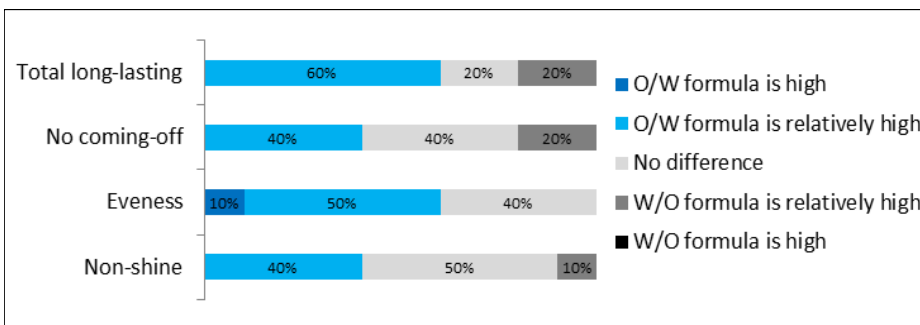


Figure 12: Long-lasting effect test of the prototype o/w in Fig. 11 against the commercial w/o (fluorine type) liquid foundation. (commercial w/o: polyether modified silicone 0.4wt%, perfluoroalkylether silicone 10wt%, volatile oil 30wt%, ethylhexyl methoxycinnamate 3wt% and PF surface treated pigments 20wt%)

Ingredient	(wt %)
HHM-HEC (B)	0.3
Water	40.7
Ethanol	10.0
Ethylhexyl methoxycinnamate	4.5
Dimethylpolysiloxane	24.0
Isostearyl glyceryl ether	0.5
OTS surface-treated titanium dioxide	6.3
OTS treated-treated iron oxide (red, yellow, black)	1.7
OTS treated-treated zinc oxide	6.0
OTS treated-treated zinc oxide (microparticle)	6.0

Table VIII: Composition of the emulsion tested in SPF measurement

tage measured for the water resistance of this formula was 90.9 % ± 11.4 %. This emulsification system could therefore potentially provide water-resistant O/W type sunscreens.

CONCLUSION

The characteristic associative thickening properties of HHM-HEC and control of the pigment surface treatment enabled preparation of a superior O/W type formulation. The wettability and aggregability of pigments in

oil media were important factors for dispersibility. With this formulation a fresh feel, high water and oil repellency and protection from ultraviolet rays were all achieved at the same time. They are considered to be useful in an environment of high temperature and humidity. In addition, this type of emulsion is sustainable because it contains a small amount of oils. These findings and techniques have been utilized in practical applications. First, a silicone-type sunscreen product was launched. Fluorine-type makeup bases and liquid foundations followed. Presently, there are many types of sunscreens based on this formulation on the market, and the range is continually expanding.

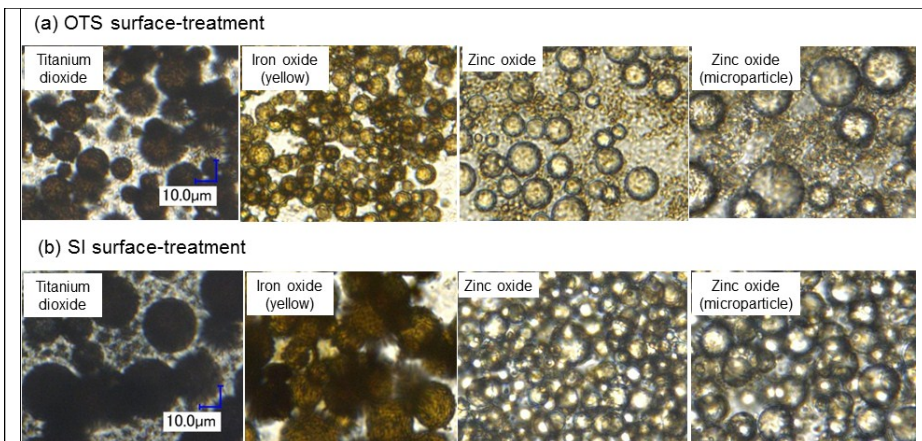


Figure 13: Photomicrographs of a dispersion of surface treated pigments (5wt%) in a mixture of ethylhexyl methoxycinnamate (24wt%) and dimethyl polysiloxane (71wt%)

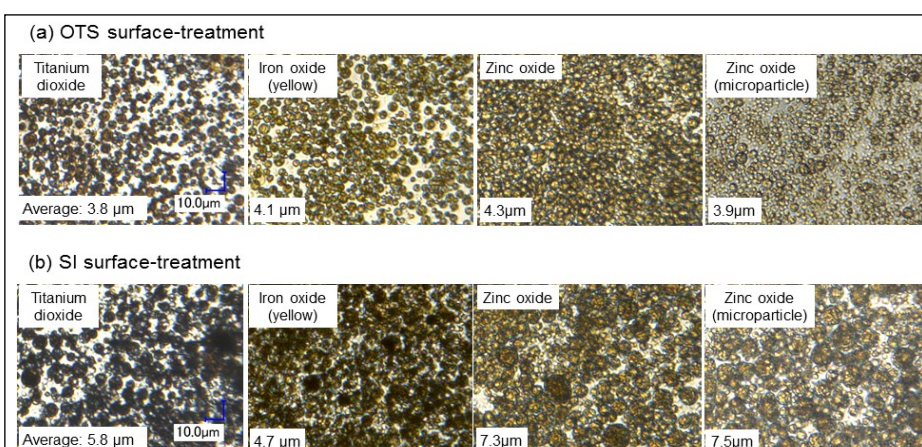


Figure 14: Photomicrographs of a HHM-HEC o/w emulsion including hydrophobically surface treated pigments. (HHM-HEC(B) 0.3wt%, dimethyl polysiloxane 16.5wt%, ethylhexyl methoxycinnamate 3wt%, isostearyl glyceryl ether 0.5wt%, surface treated pigments 10wt%)

REFERENCES

[1] Kosmulski, M., *Chemical Properties of Material Surfaces*, Marcel Dekker, Inc., New York, USA, 2001, pp. 150-151

[2] Ashida, T., *Development of water-dispersible ultraviolet scattering agent* *Fragrance Journal*, 9 (2013) 36-40.

[3] Ihara, T., Nishioka, T., Kitsuki, T., and Kamitani, H., *Solution properties of a novel polysaccharide derivative*, *Chem. Lett.*, 33 (2004) 1094-1095.

[4] Akiyama, E., Kashimoto, A., Hotta, H., and Kitsuki, T., *A Novel Water-Repellent O/W emulsion Using a New Water-Soluble Amphiphilic Polymer*, *IFSCC Magazine*, 9, 4 (2006) 313-318.

[5] Patent WO98/13389

[6] *Product catalog of DAITO KASEI*, Japan, 2013.

[7] Patent JP 5149886

[8] Kobayashi, K., Terada, T., and Ikeda, S., *Pigment Dispersion in Water Soluble Acrylic Resins*, *Shikizai*, 62 (1989) 524-528.

[9] Pissavini, M., Alard, V., Heinrich, U., Jenni, K., Perier, V., Tournier, V., Lutz, D., Meloni,

M., Kockott, D., Ferrero, L., Gonzalez, B., Zastrow, L., and Tronnier, H., *In vitro assessment of water resistance of sun care products: a reproducible and optimized in vitro test method*, *International Journal of Cosmetic Science*, 29 (2007) 451-460.

[10] Akiyama, E., Kashimoto, A., Hotta, H., and Kitsuki, T., *Mechanism of oil-in-water emulsification using a water-soluble amphiphilic polymer and lipophilic surfactant*, *J. Colloid Interface Sci.*, 300 (2006) 141-148.

[11] Akiyama, E., Kashimoto, A., Yago, Y., Hotta, H., Ihara, T., and Kitsuki, T., *Thickening properties and emulsification mechanisms of new derivatives of polysaccharide in aqueous solution 2: the effect of the substitution ratio of hydrophobic/hydrophilic moieties*, *J. Colloid Interface Sci.*, 311 (2007) 438-446.

[12] Kawakami, K., Ihara, T., Nishioka, T., Kitsuki, T., and Suzuki, Y., *Salt Tolerance of an*

Aqueous Solution of a Novel Amphiphilic Polysaccharide Derivative, *Langmuir*, 22 (2006) 3337-3343.

[13] Shao, Y., and Schlossman, D., *Super Dispersible Pigment Treatment for Applications in Multimedia*, *Podium Proceedings of 23rd IFSCC Congress* (2004) 239-243.

[14] *Product catalog of Solvay Specialty Polymers*, 2012.

Corresponding author
email: akiyama.eri@kao.co.jp

Restoration of Both Epithelial and Endothelial Perlecan / Dystroglycan Expressions by Polygonum bistorta Induces Skin Rejuvenation

Pain, Sabine¹; Dos Santos, Morgan²; Gaydon, Amandine¹; Boher, Aurélie¹; Gaillard, Christelle¹; Bechetoille, Nicolas¹; Rousselle, Patricia^{2*} and André, Valérie^{1*}.

¹BASF Beauty Creations, Beauty Care Solutions France SAS, 32 rue Saint Jean de Dieu, 69007 Lyon, France.

²Laboratoire de Biologie Tissulaire et Ingénierie Thérapeutique, Institut de Biologie et Chimie des Protéines; UMR 5305; CNRS; Univ. Lyon 1; SFR BioSciences Gerland-Lyon Sud; 7 passage du Vercors, 69367, Lyon, France.

Keywords: Perlecan, dystroglycan, basement membranes, Polygonum bistorta and skin aging

ABSTRACT

Perlecan is one of the main well-characterized basement membrane heparan sulfate proteoglycans (HSPGs), playing a role in epidermal morphogenesis. Dystroglycan is considered a major perlecan partner. Dramatic changes occurring within epidermal and endothelial basement membranes during the chronological aging process lead to an impaired epidermis and capillary fragility. Findings in the literature, led us to ask whether expression of perlecan and dystroglycan were modified with aging.

We showed immunohistochemically on a cohort of 36 human biopsies that perlecan expression decreased in both epithelial and

endothelial basement membranes during aging. We confirmed these results in a proprietary skin equivalent model and at gene expression levels in keratinocytes and in endothelial cells from different volunteers aged from 17 to 75 years (data not shown). Based on proteomic screening on keratinocytes and endothelial cells, Polygonum bistorta root extract was selected because it was able to induce perlecan and dystroglycan expression. We also used immunofluorescence to show that Polygonum bistorta extract increased Claudin-5 expression in endothelial cells, demonstrating an improvement in their cohesion.

Finally, to prove the *in vivo* effects of Polygonum bistorta, we performed an *in vivo* test with 45 volunteers with a dull complexion. After application of a formulation with 1% of Polygonum bistorta root extract the skin of the volunteers was more radiant and showed fewer crow's feet. Moreover, the skin contrast and skin homogeneity were improved.

Altogether, this study reinforces findings on the role of perlecan in epidermal homeostasis and further reveals its implication for age-related epidermal disorders.

INTRODUCTION

Recently, the field of proteoglycans has emerged as an important class of basement membrane components presenting major biological and structural properties. In addition to their involvement in epidermal/dermal attachment, these components of the dermal-epidermal junction play crucial roles in biological events such as adhesion, migration, proliferation and differentiation of keratinocytes [1]. Perlecan, one of the main well-characterized basement membrane heparan sulfate proteoglycans, is crucial for skin homeostasis and for the terminal differentiation of keratinocytes. Despite findings showing that the perlecan gene is expressed in both keratinocytes and fibroblasts, the perlecan localized in the dermal-epidermal junction is produced by keratinocytes [2]. Dystroglycan, which is produced by both keratinocytes and fibroblasts, is described as a major perlecan partner.

Dramatic changes occurring in the skin during the chronological aging process lead to altered epidermal and endothelial basement membranes with an increase in capilla-

ry permeability and fragility [2, 3]. Sher et al. (2006) showed that exogenous addition of perlecan restores the ability of perlecan-deficient keratinocytes to form fully differentiated epidermis [2]. Recent experiments confirmed these results by showing that exogenous perlecan has the ability to restore an altered basement membrane produced by aged keratinocytes [4]. Findings in the literature led us to ask whether perlecan and dystroglycan expression was modified with aging and whether age-related modifications can be related to a lack of functional properties of the skin with aging. Then, using a specific in-house screening method, we corrected perlecan and dystroglycan expression in different culture systems.

EXPERIMENTAL

Monolayer cultures

Normal human keratinocyte monolayers were established from skin specimens isolated during plastic surgery (50-year-old patient - retrieved from the Biological Resources Center-Hospices Civils de Lyon (BCR-HCL, Lyon, France) and grown in Keratinocyte SFM

medium (PRF Life Technology Invitrogen, Cergy Pontoise, France). Human microvascular endothelial cells (HMVEC) were purchased and cultured in EMG2-MV (Lonza, Basel, Switzerland).

Plate immunoassay method for perlecan and dystroglycan expression in keratinocytes and endothelial cells

Human microvascular endothelial cells and keratinocytes from 50-year-old donors were seeded in 96-well plates until 80% confluence. Cells were fixed with PBS/ paraformaldehyde 2%, permeabilized with PBS/ Triton X100 0.5% and uncovered with chondroitinase ABC 0.5 % and heparitinase I 0.5%. After a saturation step with PBS/ BSA 1% for 60 min, antibodies were incubated 90 min either with anti-perlecan antibody (2.5 mg/mL, clone 3G166, Novus Biological, Littleton, USA), or anti-dystroglycan antibody (4 mg/ml, sc-28535, Tebu Bio, Le Perray-en-Yvelines Cedex, France). Secondary antibodies were FITC goat anti-mouse (7.5 mg/ml, 115-095-146, Jackson ImmunoResearch, Marseille, France) and FITC mouse anti-rabbit (15 mg/ml, 442220, Interchim, Montluçon, France).

Fluorescence was detected with a specific plate reader with an excitation at 485 nm and emission at 528 nm. The results were normalized to the MTT test and reported as % relative to the untreated sample.

Histology and immunohistological analysis

Thirty-six donors were included in this study: Eighteen older persons (age range 50-73 years) and 18 younger persons (age range 22-47 years).

The skin specimens came from patients who underwent mammary reduction (BRC - HCL, Lyon, France). After surgery, tissues were either immediately frozen in liquid nitrogen or fixed for 24 hours and embedded in paraffin processed for paraffin embedding. Paraffin-embedded formalin-fixed samples were then cut into 5 µm sections. After dewaxing and rehydration, sections were stained with hematoxylin. Next, endogenous peroxidases were inactivated and non-specific binding was blocked before incubating sections with perlecan antibody (clone 3G166, US Biologicals, Boston, USA). After incubation for 1 hour with the peroxidase-conjugated secondary antibody (EnVision, Dakocytosystem, Les Ulis, France), the antigen was detected with the specific substrate. Tissue sections were subsequently counterstained for 40 seconds with Harris hematoxylin (25%, Sigma Aldrich, Saint-Quentin Fallavier, France).

For immunofluorescence, the frozen biopsies were embedded in Cryomount embedding medium (Microm, Francheville, France). Histological specimens 6 mm-thick were fixed and incubated for 1 hour with perlecan antibody (Euromedex, Souffelweyheim, France) followed by secondary antibody coupled to an Alexa-633 probe. Cell nuclei were then counterstained before being mounting on microscope slides.

Perlecan immunostaining was observed using an LSM700 laser scanning confocal system (Zeiss, Marly le roi, France). Twelve representative images were captured for each condition in the same manner. 8-bit images were saved in an uncompressed Zeiss image file format (lsm).

Image analysis was performed using the software NIS-Elements v.4 (Nikon, Champigny sur Marne, France). Pixels corresponding to perlecan immunostaining in the dermal-epidermal junction area were segmented from other pixels. The mean grey value of perlecan specific area was measured automatically.

Senescent and chimeric skin equivalents

For the preparation of dermal equivalent, fibroblasts from a 20 years old donor were seeded onto a dermal substrate made of chitosan-collagen-GAG matrix. This dermal equivalent was grown for 14 days at 37°C in a 5% CO2 atmosphere. For the preparation of skin equivalents (SE), keratinocytes from a 20 years old donor were seeded on the dermal equivalent at day 14. After 7 days of submerged culture in an appropriate medium, the SE was raised at the air-liquid interface and cultured in an appropriate medium [5]. The SE samples were harvested at day 35 of culture following fibroblasts seeding for young SE and at day 100 for senescent SE.

For the chimeric skin equivalent, young fibroblasts from a 20 year old donor were seeded with keratinocytes from a 56 year old donor. Samples were harvested for immunohistology studies.

Cosmetic treatment

For the screening of cosmetic active ingredients, cells were plated in 96 well plates, cultivated for 2 days either with vehicle or with the water soluble Polygonum bistorta root extract (PERLAURATM, BASF Beauty Care Solutions, Lyon, France) in dose effect before in situ cell-based enzyme-linked immunosorbent assay to detect and quantify perlecan and dystroglycan core proteins in human skin cells microenvironment. In house in situ cellular ELISA has been developed with perlecan antibody from Novus Biologicals, Littleton, USA (H1890-93) and with dystroglycan antibody from Santa Cruz Biotechnology, Dallas, USA (sc-28535). Fluorescence intensity was determined at 485-535 nm with a VICTOR X4 Technologies reader (Perkin Elmer SAS, Courtaboeuf, France). Each assay point was derived from six measurements.

Living skin biopsies

Human skin samples were obtained from plastic surgery on patients (Caucasian women of 50 and 55 years). Skin samples were then placed on culture inserts with the epithelium uppermost at an air/liquid interface. At day 0, skin samples were cultured either with maintenance medium alone [5] (untreated sample) or with 0.5% of the soluble Polygonum bistorta extract for 6 days. Treatment was stopped by successive rinsing in PBS. Skin samples were frozen with -120°C isopentane before perlecan immunostaining and nuclei counterstaining as previously described.

CLINICAL TRIALS

Study model

The study was conducted on the whole face with comparison of the results obtained after 2 and 4 weeks of application versus baseline (time 0). Each volunteer served as her own control. The study was carried out between February and April 2013.

Volunteer recruitment criteria

All volunteers were female, aged from 25 to 65 with skin phototype I to III skin, a dull complexion and wrinkles around the eyes. The study was completed with 45 volunteers.

Application method

The following clinical test formula at pH 5.45 was applied to the whole face twice a day for 4 weeks.

INCI name	%
Glyceryl stearate and ceteareth-20 and ceteareth-12 and cetearyl alcohol and cetyl palmitate	5%
Behenyl alcohol	2%
Ethylhexyl palmitate	5%
Hexyldecanol and Hexyldecyl Laurate	3%
Dicaprylyl ether	3%
Sodium polyacrylate	0.8%
Dimethicone	1%
Aqua	73.10%
Propylene glycol and phenoxyethanol and chlorphenesin and methylparaben	2.5%
Glycerin	3%
Sodium stearyl glutamate	0.4 %
Xanthan gum	0.2 %
Polygonum bistorta root extract	1%

Table 1: Formula of Cream Containing the Polygonum bistorta Root Extract

Assessment methods

Visible signs of skin aging were assessed in vivo using a digital image capture system (VISIA-CR®, Canfield, Fairfield, USA). The Canfield Visia CR® takes high quality images using pre-set lighting parameters which are ideally suited for recording the specific conditions of skin. The images were obtained at baseline and after 2 and 4 weeks of application and the length, area covered by and volume of the wrinkles were analyzed.

- **Wrinkle length:** A map of the wrinkled skin area was drawn. The lengths of each of the individual wrinkles were added together. Length was matched to the number of pixels on the map (1 pixel = 0.03 mm). When the length of wrinkles decreased, crow's feet were less visible.
- **Wrinkle volume:** Wrinkle volume was calculated by counting the pixels in the entire area measured, taking into account color intensity to gain an idea of wrinkle depth (volume = area x depth).
- **Wrinkle surface area:** The number of segmented pixels was calculated to de-

termine the apparent surface area of the crow's feet. A decrease in the surface area of the wrinkles indicates a decrease in the size of crow's feet (1 pixel = 0.03 mm).

Image analysis was also conducted to assess skin appearance as measured by the contrast and entropy.

The contrast measures the local variations of grey levels and is defined as follows:

$$Contrast = \sum_{i,j=0}^{N-1} P_{i,j} (i - j)^2$$

The contrast decreases when the texture becomes thinner and finer.

The entropy reflects the complexity of the texture and is defined as follows:

$$Entropy = \sum_{i,j=0}^{N-1} P_{i,j} (-\ln(P_{i,j}))$$

The entropy decreases when the texture becomes more regular. Cosmetically speaking, the term entropy can be translated as the skin smoothness.

Both crow's feet and radiance were assessed visually by a technician.

- *Crows' feet*: Mean visual scores were measured and compared with the crows' feet scale in the skin aging atlas T.1 for the Caucasian type skin.
- *Radiance*: Mean visual skin radiance scores were measured and compared with an in-house scale developed by BASF.
- *Statistics*: Statistics are specified in each figure caption.

RESULTS AND DISCUSSION

Decrease in perlecan expression during skin aging

Normal human biopsy cohort

Immunohistochemical revelation of perlecan with DAB in a cohort of 36 human skin biopsies from donors aged from 22 to 73 years revealed strong and continuous staining in the epidermal basement membrane (**Figure 1**) and the basement membranes of dermal micro-vessels (**Figure 2**) in young skin that decreased in aged skin. Quantification showed that perlecan expression is significantly decreased by 76 % and 97 % from 38 years

(mean age) to 57 years (mean age), respectively, compared with in the epithelial basement membrane of a 27 year old (mean age) (**Figure 1B**). In **Figure 2B**, it can be seen that perlecan protein expression decreased up to 81 % from a group of donors with a mean age of 32 to a group of donors with a mean age of 57.

Perlecan sensitivity to proteolysis suggests that controlled degradation processes may regulate its bioactivity, including growth factor storage and release [6, 7]. Enzyme up-regulation during aging [6, 7] or in senescent cells [8] may accelerate perlecan degradation. Moreover, q-RT-PCR analysis revealed a reduced level of perlecan transcript in aging keratinocytes (data not shown) suggesting

that a disturbed ability to neo-synthesize perlecan may create a disorder in the perlecan synthesis/degradation balance. This severe decline in the perlecan mRNA level with aging may be a result of the location of its gene, namely HSPG2, on the telomeric portion of chromosome 1 at locus 1p36.1 [9]. Telomerase has been detected in keratinocytes of the basal epidermis and in the bulge component of the hair follicle [10], and evidence suggests that telomeres shorten with age in human skin [11].

Chimeric skin equivalent model

We mimicked the earliest signs of skin aging in the proprietary skin equivalent MI-MESKIN™. In **Figure 3A**, it is evident that perlecan protein expression decreased in the dermal-epidermal junction in the long-term culture (100 days) relative to the 42-day culture. In **Figure 3B**, we used a chimeric skin equivalent model to analyze the impact of keratinocyte aging on perlecan expression. As shown in **Figure 3B** (left), when young keratinocytes were seeded, the skin equivalent supported epidermal proliferation, giving rise to a full thickness and well organized terminally differentiated epidermis, and displayed perlecan expression evenly along the dermal-epidermal junction. Seeding aged normal human keratinocytes over these SEs led to an obvious decrease in epidermal thickness (**Figure 3B**, right). No perlecan was found in the dermal-epidermal junction. The reduction in cell layers was accompanied by anomalies in the differentiated layers, reflecting disorganization and abnormalities in the differentiation process. These data show that aged keratinocytes are unable to form a multi-layered well-differentiated epidermis in three-dimensional culture conditions associated with a disappearance of perlecan expression.

In conclusion, we showed that aged keratinocytes deficient in perlecan production display an inability to form a multilayered epidermis. Addition of purified perlecan to the culture medium increased epidermal thickness and restored a well-differentiated multilayered epithelium [4]. Basal and intermediate epidermal layers were particularly well developed, confirming the ongoing process of the stratification program. A similar observation was documented in a recently published analysis of the corneal epithelium of perlecan-deficient mice [12].

Polygonum bistorta activities

Polygonum bistorta induced perlecan and dystroglycan expression in keratinocytes and endothelial cells in vitro

In order to perform the screening, we developed an "in-house" plate immunoassay me-

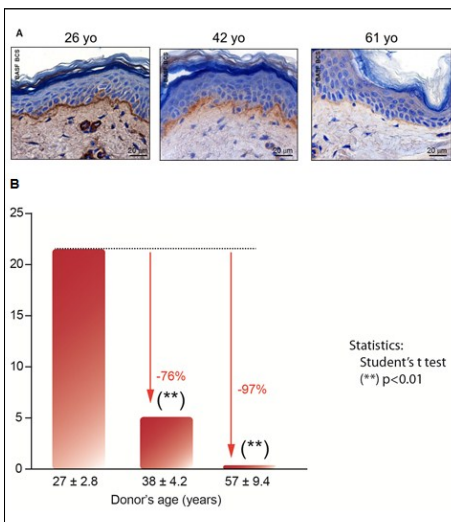


Figure 1: Immunohistochemical staining of perlecan in epithelial basement membranes (A) and quantitative analysis (B).

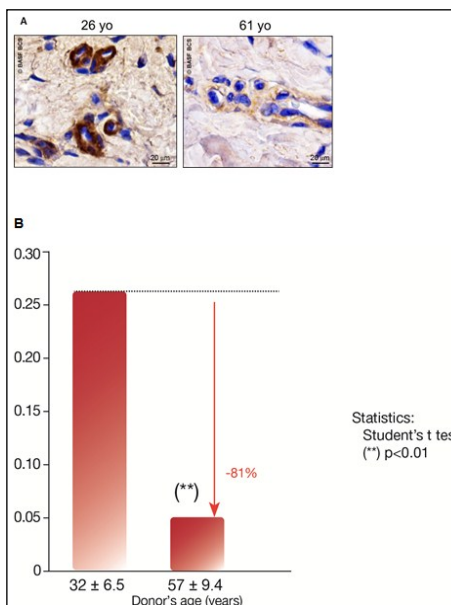


Figure 2: Immunohistochemical staining of perlecan in endothelial basement membranes (A) and quantitative analysis (B).

Figure 3: Perlecan expression in skin equivalents (SE). (A) Young fibroblasts and keratinocytes were cultured for 42 days or 100 days. (B) Young fibroblasts (YF) and keratinocytes (YK) versus young fibroblasts (YF) versus aged keratinocytes (AK). (Counterstaining with Harris hematoxylin, chromogenic DAB revelation.)

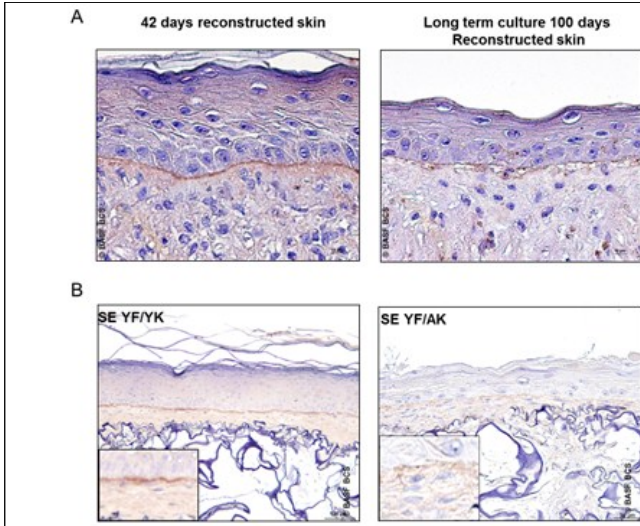
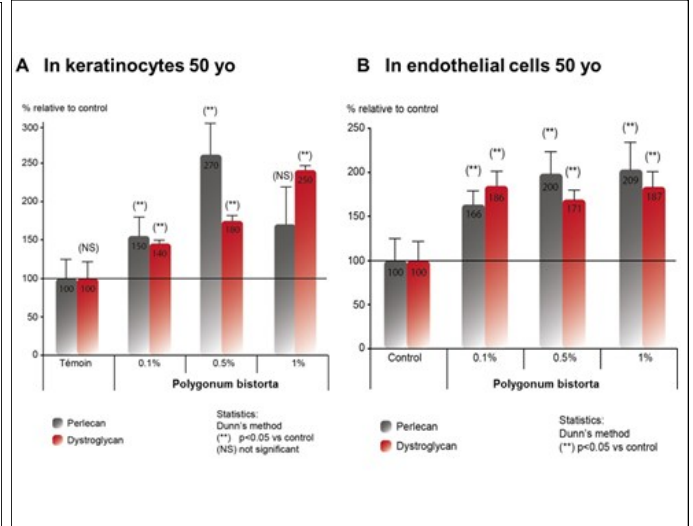


Figure 4: Dose-dependent induction of perlecan and dystroglycan expression by *Polygonum bistorta* in both keratinocytes (A) and endothelial cells (B) from a 50-year-old volunteer. These experiments are representative of 4 experiments (with n=6 samples for each point) in keratinocytes and representative of 3 experiments (with n=6 samples for each point) in endothelial cells



thod which consists of the identification of perlecan and dystroglycan proteins by fluorescence. The *Polygonum bistorta* root extract which was selected, also known as Meadow Bistort, is a species of flowering plant native to Eastern Europe. In keratinocytes from a 50-year-old donor, *Polygonum bistorta* extract induced significant perlecan protein expression at 0.1% (increase of 50%) and 0.5% (increase of 170%) and dystroglycan up to 1% (increase of 150%) (Figure 4A). In endothelial cells from a 50-year-old donor, *Polygonum bistorta* extract induced significant expression of both perlecan and dystroglycan up to a concentration of 1% (Figure 4B). For the following experiments,

we chose 0.5% *Polygonum bistorta* root extract as the efficient concentration.

Polygonum bistorta effect on perlecan in living skin biopsy.

Cutaneous explants from a 50-year-old donor were maintained in culture for 6 days in a specific medium either without (untreated) or with 0.5% of *Polygonum bistorta* root extract (Figure 5). In Figure 5A, we can see a spread and decreased perlecan expression in the dermal-epidermal junction after 6 days in culture and a recovery of this expression in the presence of *Polygonum bistorta* (A). Figure 5B shows the quantification and suggests that recovery with *Polygonum bistorta* root

ex vivo, a phenomenon resembling skin aging. We suggest that *Polygonum bistorta* was able to reverse this phenomenon and preserve a young skin profile.

Effect of Polygonum bistorta on tight junction Claudin-5 in endothelial cells

During the aging process, cutaneous blood vessels become more fragile and permeable. A more specific test on endothelial cell tight junctions highlights the ability of *Polygonum bistorta* to boost capillary cohesion, which is known to ensure the high quality exchange of fluids and nutrients in skin. A Student's t test showed that claudin-5 fluorescence increased by 35 ± 4% with *Polygonum bistorta* root extract 0.5% versus untreated cells relative to 100% fluorescence p < 0.027 (Figure 6).

In conclusion, we could demonstrate the efficacy of the water-soluble *Polygonum bistorta* root extract on the induction of both perlecan and dystroglycan protein expression in monolayer cultures of keratinocytes and

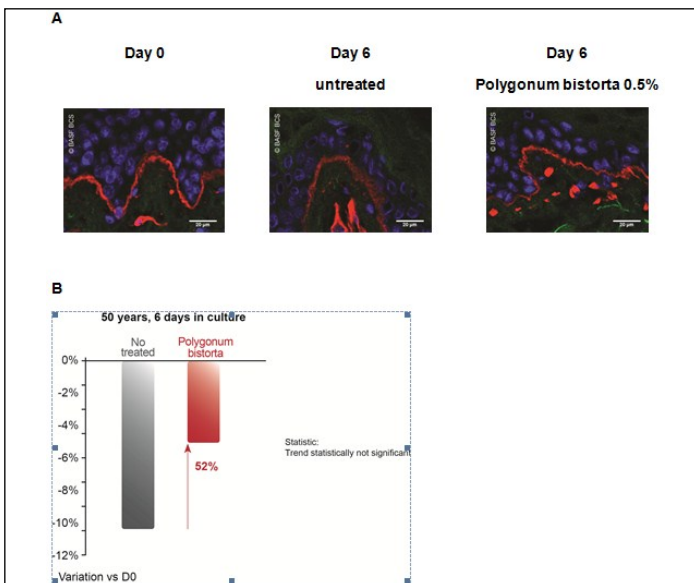


Figure 5: *Polygonum bistorta* (0.5%)-induced perlecan protein expression in epithelial basement membrane in living skin biopsies cultured for 6 days (A) and quantification of perlecan compared with day 0 (B).

extract present reached 52%. An impaired balance between perlecan and dystroglycan synthesis was therefore observed during the skin biopsy fate

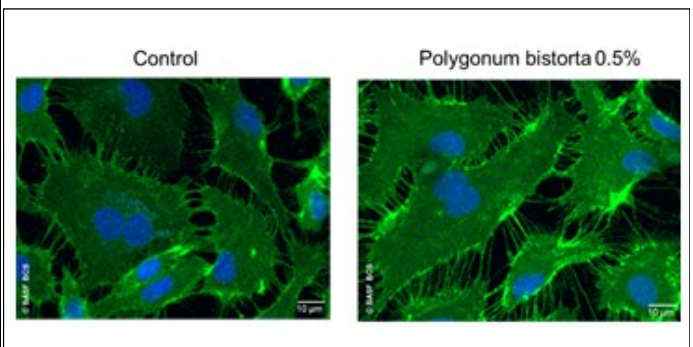


Figure 6: Induction of claudin-5 expression in endothelial cells by *Polygonum bistorta* 0.5% (35% increase with Student's t test p<0.027).

endothelial cells and in ex vivo cutaneous explants. Moreover, we showed that Polygonum bistorta root extract induced expression of the tight junction protein, Claudin-5, in endothelial cells. These results, obtained in vitro, prove that Polygonum bistorta root extract has the ability to reinforce both epidermal and endothelial structures strongly affected by aging.

In addition, a clinical study was performed with 45 healthy Caucasian human volunteers with wrinkles and a dull complexion.

Clinical trial

The aim of the clinical trial was to demonstrate in vivo the ability of Polygonum bistorta root extract to restore the skin's radiance and texture, reduce crows' feet and the wrinkle length and surface. Image analysis was performed to assess these different parameters. The full face study was conducted with a panel of 45 female volunteers aged 25 to 65 selected for their type I to III phototype and a dull complexion with wrinkles around the eyes (the volunteers served as their own control). A formulation containing 1% Polygonum bistorta root extract was applied to the whole face twice daily for 4 weeks and the

parameters assessed at different time and compared with the condition before treatment.

Polygonum bistorta improves skin radiance, contrast and smoothness

Polygonum bistorta formulated at 1% improved the skin radiance significantly by 22% already after 2 weeks and by 42% after 4 weeks of application compared with day 0 (Figure 7). Polygonum bistorta root extract significantly decreased the skin contrast by 21% after 2 weeks and by 23% after 4 weeks of application (Figure 8). In Figure 9, it can be seen that Polygonum bistorta root extract significantly improved the skin smoothness (as measured by the entropy) by 3% after 2 weeks of application.

Polygonum bistorta root extract improves crow's feet and wrinkle length and surface

Polygonum bistorta root extract formulated at 1% significantly decreased the crow's feet by 18% after 4 weeks of application (Figure 10). The improvement is evident in Figure 11B, where the crow's feet are indicated by arrows. The conspicuous cumulative length

and surface of wrinkles were each significantly reduced by 12% and 11%, respectively, after 4 weeks of application (Figure 11A and 12A, respectively). Figure 12B shows the improvement of skin texture and the reduced number of wrinkles.

CONCLUSION

An extract of Polygonum bistorta root was found to successfully improve the repair of basement membranes by inducing higher levels of perlecan and dystroglycan expression in both keratinocytes and endothelial cells. Improvements were confirmed by a clinical study which was able to demonstrate improvements in skin radiance, in the reduction of multiple wrinkle attributes, and in overall skin smoothness (entropy). By reinforcing the structural integrity of the basement membranes, Polygonum bistorta helped make the skin look visibly brighter and smoother as early as after two weeks of application.

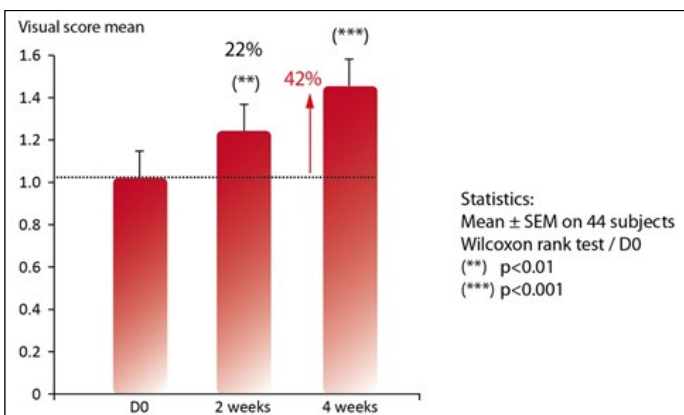


Figure 7: Improvement in skin radiance with Polygonum bistorta 1% in the formula after 2 weeks (significant) and 4 weeks of application.

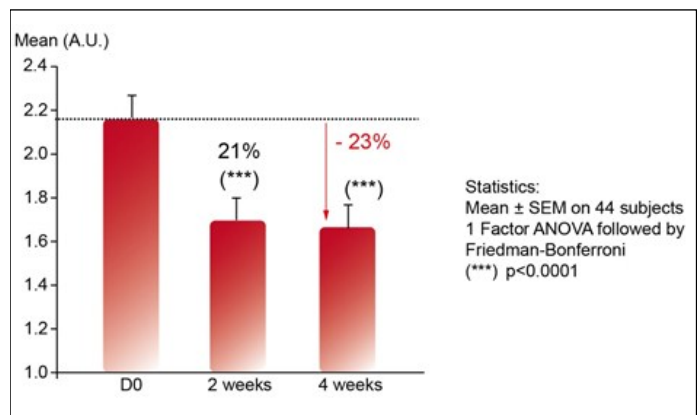


Figure 8: Decrease in skin contrast with Polygonum bistorta 1% in the formula after 2 weeks and 4 weeks of application.

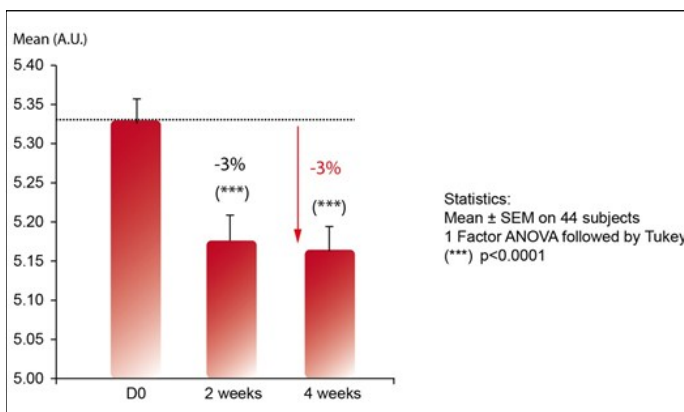


Figure 9: Improvement in skin smoothness (decrease in entropy) with Polygonum bistorta 1% in the formula after 2 weeks and 4 weeks of application.

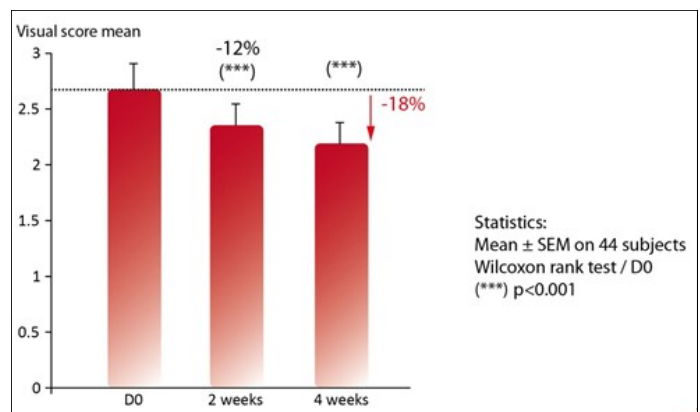


Figure 10: Decrease in crow's feet with Polygonum bistorta 1% in the formula after 2 weeks and 4 weeks of application.

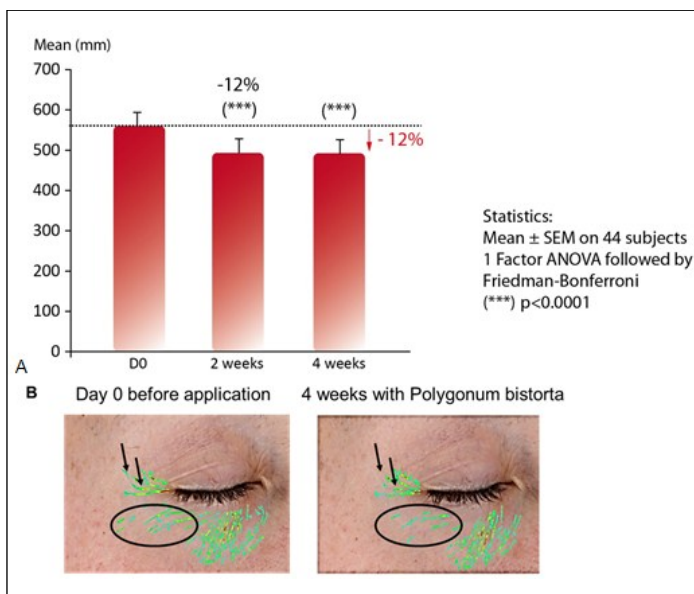


Figure 11: Decrease in the conspicuous cumulative length of wrinkle with Polygonum bistorta 1% in the formula. (A) quantification, (B) illustration.

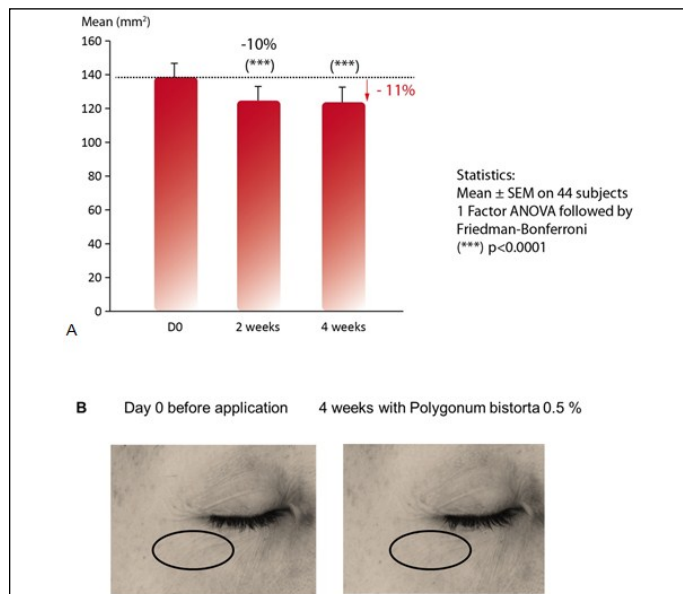


Figure 12: Decrease in the conspicuous surface of wrinkles with Polygonum bistorta 1% in the formula. (A) quantification, (B) illustration.

REFERENCES:

- [1] Ko, M.S., and Marinkovich, M.P., Role of dermal-epidermal basement membrane zone in skin, cancer, and developmental disorders, *Dermatol Clin.*, 28 (2010) 1-16.
- [2] Sher, I., Zisman-Rozen, S., Eliahu, L., Whitelock, J.M., Maas-Szabowski, N., Yamada, Y., Breitzkreutz, D., Fusenig, N.E., Arikawa-Hirasawa, E., Iozzo, R.V., Bergman, R., and Ron, D., Targeting perlecan in human keratinocytes reveals novel roles for perlecan in epidermal formation. *The Journal of Biological Chemistry*, 281 (8) (2006) 5178-5187.
- [3] Gilchrist, B.A., *Skin aging 2003: recent advances and current concepts*, *Cutis*, 2003, 72 (3 Suppl): 5-10.
- [4] Dos Santos, M., Michopoulou, A., André-Frei, V., Boulesteix, S., Dayan, G., Whitelock, J., Damour, O., and Rousselle, P. Decreased perlecan expression in aged skin contributes to epidermal fading (submitted).
- [5] Black, A.F., Bouez, C., Perrier, E., Schlotmann, K., Chapuis, F., Damour O., Optimization and characterization of an engineered human skin equivalent. *Tissue Eng.*, 11 (2005) 723-33.
- [6] Whitelock, J.M., Murdoch, A.D., Iozzo, R.V. and Underwood P.A., The degradation of human endothelial cell-derived perlecan and release of bound basic fibroblast growth factor by stromelysin, collagenase, plasmin, and heparanases, *J Biol. Chem.*, 27 (1996) 10079-86.
- [7] Iriyama, S., Matsunaga, Y., and Amano, S., Heparanase activation induces epidermal hyperplasia, angiogenesis, lymphangiogenesis and wrinkles, *Exp. Dermatol.*, 19 (2010) 965-972.
- [8] Campisi, J., *The role of cellular senescence in skin aging*, *J. Invest. Dermatol. Symp. Proc.*, 3 (1998) 1-5.
- [9] Wintle, R.F., Kisilevsky, R., Noonan, D., and Duncan, A.N., In situ hybridization to human chromosome 1 of a cDNA probe for the gene encoding the basement membrane heparan sulfate proteoglycan (HSPG). *Cytogenet., Cell. Genet.*, 54 (1990) 60-61.
- [10] Ramirez, R.D., Wright, W.E., Shay, J.W., and Taylor, R.S., Telomerase activity concentrates in the mitotically active segments of human hair follicles, *J. Invest. Dermatol.*, 108 (1) (1997) 113-117.
- [11] Buckingham, E.M., and Klingelutz, A.J., The role of telomeres in the aging of human skin, *Exp Dermatol.*, 20(4) (2011) 297-302.
- [12] Inomata, T., Ebihara, N., Funaki, T., Matsuda, A., Watanabe, Y., Ning, L., Xu, Z., Murakami, A., and Arikawa-Hirasawa, E., Perlecan-deficient mutation impairs corneal epithelial structure, *Invest. Ophthalmol. Vis. Sci.*, 53(3) (2012):1277-84.

Corresponding author
email: sabine.pain@basf.com

Balance of Cleaning Efficacy and Dental Hard Tissue Abrasive Wear: An In Vitro Study Assessing Toothpaste Effects Associated with Manual or Powered Toothbrushes

Thomas Welss, Claudia Hundeiker and Thomas Förster

¹Henkel Beauty Care, Henkel AG & Co. KGaA, Düsseldorf, Germany

Presented during the 60th SEPAWA Congress, October 2013

Keywords. Oscillating-rotating powered toothbrushes, abrasion, stain removal, enamel abrasion, dentin abrasion, toothpaste

ABSTRACT

The two objectives of this study were a) to elucidate the balance between cleaning performance and dental hard tissue abrasion of different toothpaste formulations when brushed with manual or high oscillating-rotating powered toothbrushes and b) to evaluate if formulations especially developed for use with powered toothbrushes have an optimized balance between dental hard tissue abrasion and cleaning efficacy.

To assess abrasion on the dental hard tissue, two standard in vitro methods were used: relative dentin abrasion and relative enamel abrasion tests. Furthermore effects on the enamel surfaces were evaluated using profilometry and atomic force microscopy. In addition, the cleaning performance of the same regimens (toothpaste and toothbrushes) was investigated in vitro using the pellicle cleaning ratio test.

With these experimental setups, the in vitro results indicate two main findings: a higher degree of dental hard tissue abrasion with no substantial improvement on the cleaning performance versus using manual toothbrushes for toothpastes used in combination with the powered oscillating-rotating toothbrush and an improved balance between abrasion and cleaning performance for toothpaste formulations developed especially for use with powered toothbrushes.

INTRODUCTION

The common recommendation for an oral hygiene regimen is brushing the teeth twice daily for 2 to 3 minutes using a toothbrush and fluoridated toothpaste. This allows for not only stain and plaque removal but also remineralization of previously demineralized teeth. However, if not properly done, toothbrushing can lead to abrasion of dental hard tissue with subsequent loss of tooth form, function and esthetics as well as dental hypersensitivity [1].

The kind of oral hygiene regimen, i.e. combination of the individual brushing technique, composition of toothpaste and type of toothbrush used, is an important factor to be considered [2, 3]. Some decades ago the development of powered toothbrushes was a further milestone in optimizing the daily oral hygiene regimen. In Europe, powered toothbrushes, either powered oscillating-rotating or (ultra)sonic toothbrushes, are used by approximately 25% of consumers. Powered toothbrushes are more effective than manual ones in plaque removal and thus in improving gingival conditions [4, 5]. Powered toothbrushes showed no clinically relevant negative impact and were assessed as being safe for hard and soft dental tissues [6]. In contrast, recent in vitro studies have implied that powered toothbrushes might increase the

risk of dental hard tissue abrasion due to the high agitation of the brush heads [7, 8]. In detail, activated powered toothbrushes increased abrasion of sound and eroded dentin. Additionally, increased abrasion of eroded enamel was reported.

Furthermore, consumers increasingly seek toothpastes with very good cleaning efficacy and extrinsic stain removal properties ('whitening'). But cleaning efficacy and abrasion often go hand in hand and a high cleaning performance is usually accompanied by increased abrasion [9].

Since whether or not toothpastes used with powered toothbrushes increase the risk of dental hard tissue abrasion compared with manual toothbrushes is controversial, this study had the following two objective: A) elucidate the balance between cleaning performance and dental hard tissue abrasion of toothpastes when brushed with manual or oscillating-rotating powered toothbrushes and b) evaluate if formulations developed especially for use with powered toothbrushes have a better balance between dental tissue abrasion and cleaning efficacy.

We performed a multitude of in vitro tests to compare the effects on the dental hard tissue after brushing with four different toothpastes either with a manual toothbrush or an oscillating-rotating powered toothbrush.

Toothbrushes were selected from the German market, two from the "regular" segment and two from the "whitening" segment. In each segment, one toothpaste was developed especially for use with powered toothbrushes and contained a special ratio of surfactants and hydrated silica. We analyzed the dental hard tissue abrasion by measuring the relative dentine abrasion and relative enamel abrasion. Furthermore, effects on the enamel surfaces were evaluated by profilometry and atomic force microscopy. At the same time, we assessed the respective cleaning power by determining the pellicle cleaning ratio (PCR) to elucidate whether the cleaning efficacy corresponds to abrasion and how this differs between a manual and a powered toothbrush.

EXPERIMENTAL

Materials

Toothbrushes

Oscillating-rotating powered toothbrush: Braun - Oral-B® Professional Care 500 (Procter & Gamble, Schwalbach, Germany with Oral-B® Precision Clean brush head). This powered toothbrush was selected because it is by far the most commonly used powered toothbrush in Western Europe.

Manual toothbrush: Oral-B® 40 toothbrushes soft (Procter & Gamble, Schwalbach, Germany) with soft nylon filaments.

Toothpaste composition

Toothpastes were selected based on the cleaning particles used. Removal of plaque and superficial stain can be achieved by using various kinds of components. Most common are microgranular particles like Hydrated Silica, Calcium Carbonate, Baking Soda, Alumina or Pumice. But also combinations with functional actives such as sequestrants can enhance stain removal efficacy by destabilizing adherent stain.

We compared two groups of commercially available toothpastes: 1) whitening toothpastes (toothpaste A and toothpaste B) and 2) regular toothpastes (toothpaste C and toothpaste D).

The whitening toothpastes (1) and regular toothpastes (2) differ in the composition of their tooth cleaning ingredients. Toothpaste A contains Hydrated Silica, while toothpaste B combines Hydrated Silica and the sequestrant Disodium Azacycloheptane Diphosphate. Toothpaste C combines Calcium Carbonate and Hydrated Silica, while toothpaste D mainly cleanses with a combination of different hydrated silica abrasives.

Toothpastes B and D were developed especially for use with electric toothbrushes. These formulations contain a special ratio of different surfactants that improve the cleaning efficacy in combination with gentle Hydrated Silica. The whitening (B) variant furthermore contains a sequestrant to even boost the cleaning performance.

The product compositions (list of ingredients (INCI)) as well as the pH of a 10% toothpaste slurry are given in **Table I**.

METHODS

To compare the results of the relative dentin abrasion, relative enamel abrasion and pellicle cleaning ratio methods in the different setups (i.e. manual and powered toothbrushes), each test was carried out with the same brushing duration, same brush tension and same source of specimens.

Relative dentin abrasion

When assessing the relative dentin abrasion for the manual toothbrushes, we followed the protocol of Hefferren [10] as described in the ISO 11609:2010 guideline [11]. In brief, 8 human dentin specimens were subjected to neutron bombardment resulting in the for-

mation of radioactive phosphorus in the specimens under the controlled conditions outlined by the American Dental Association. The specimens were mounted in methyl methacrylate, oriented to expose the dentin, so they fit in a V8 cross-brushing machine. In a preconditioning setup the specimens were brushed for 1500 strokes using a slurry consisting of 10 g American Dental Association reference material in 50 ml of 0.5 % carboxymethyl cellulose/glycerin solution. The brushes used were those specified by the American Dental Association and experiments were done with a constant brush tension of 150 g.

Following a preconditioning, the actual test was performed using the above parameters in a sandwich design. Before and after brushing with the test product (25 g product/ 40 ml water) each tooth was brushed with the American Dental Association reference material. Following brushing, one sample was taken, weighed (approx. 1 g) and added to 5 ml of "Ultima Gold" scintillation cocktail for determining the counts per minute per weight (cpm/g). The net cpm/g of the pre and post American Dental Association reference material for each of the test slurries was calculated and averaged to use in the calculation of the relative dentin abrasion. The American Dental Association reference material was assigned a value of 100 and its ratio to the test material calculated.

For assessing the relative dentin abrasion using powered toothbrushes, the protocol was adapted as follows:

A toothbrush-dentifrice apparatus was used to test the different dentifrices with the powered brushes. The power brush was suspended from a pivoting ring so that the brushing head was perpendicular to the dentin paired specimens surface. The pressure tension on

the dentin specimens was adjusted to 150 g for each test brush and the specimens were brushed 8.5 minutes. The TDA Instrument provided a uniform stroke of 20 mm at a rate of 20/minute which corresponds to 1500 strokes on the V-8 cross-brushing machine. The slow brush stroke speed was used because movement of the bristles was from the power head and not from back and forth motions as with the manual brush. The reference runs were performed as outlined by the American Dental Association using the V-8 cross-brushing machine equipped with the manual brush.

Relative enamel abrasion

Similar to the relative dentin abrasion assessment, human incisors were used and prepared as described elsewhere. To meet special requirements for assessing enamel abrasion, minor changes were made. Here the specimens were oriented in the mounting methyl methacrylate to expose the enamel. Furthermore, in contrast to the relative dentin abrasion, the stroke counts were increase to 5000 and 28.5 minutes for manual toothbrushes and powered brushes, respectively. The reference runs were performed as outlined by the American Dental Association using the V-8 cross-brushing machine equipped with the manual brush.

Cleaning Performance

Cleaning performance was determined following a modified pellicle cleaning ratio method by Stookey et al. [12]. In contrast to the original description, FeCl₃ was added and the PGY broth substituted by a trypticase soy broth. Both changes were necessary to adapt the effectiveness of the test due to either changes in the mucin source or the bacteria strain.

Further adaptations were done for testing the cleaning performance with oscillating-

Toothpaste A	Toothpaste B	Toothpaste C	Toothpaste D
Listed Ingredients			
Aqua,	Aqua	Calcium Carbonate	Aqua
Hydrated Silica	Glycerin	Aqua	Glycerin
Glycerin	Hydrated Silica	Sorbitol	Hydrated Silica
Sorbitol	Sorbitol	Hydrated Silica	Sorbitol
PVM/MA Copolymer	Sodium Lauryl Sulfate	Sodium Lauryl Sulfate	Sodium Lauryl Sulfate
Sodium Lauryl Sulfate	Aroma	Sodium Silicate	Aroma
Aroma	Disodium Azacycloheptane Disulphonate	Sodium Monofluorophosphate	Xanthan Gum
Cellulose Gum	Xanthan Gum	Aroma	Silica
Sodium Hydroxide	Sodium Fluoride	Cellulose Gum	Sodium Fluoride
Sodium Fluoride	Trisodium Phosphate	Potassium Citrate	Trisodium Phosphate
Carrageneenan	Sodium Saccharin	Sodium Saccharin	Sodium Saccharin
Triclosan	Disodium Phosphate	Calcium Glycerophosphate	Disodium Phosphate
Sodium Saccharin	Cocamidopropyl Betaine	PEG-32	Cocamidopropyl Betaine
Mica	Zinc Sulfate	Limonene	Zinc Sulfate
Limonene	Sodium Chloride	CI 73360	Sodium Chloride
CI 77891	Sodium Sulfate		Sodium Sulfate
CI 42090	Eugenol		Limonene
	Limonene		Eugenol
	CI 77891		CI 42090
			CI 74160
			CI 77891
pH (10% toothpaste slurry)			
7,5	7,7	9,4	7,7

Table I: Product Ingredient List (INCI) and pH of 10% Toothpaste Slurry

rotating powered toothbrushes. Conditions were similar to those of the relative dentin abrasion and relative enamel abrasion measurements.

Following 800 strokes or 4.5 minutes for the powered toothbrush, stain removal was evaluated colorimetrically. Used as the internal reference was the American Dental Association standard (10 g pyrophosphate in 50 ml 0.5% carboxymethyl cellulose, 10% glycerin in water) and set to a cleaning performance of 100. The resulting brightness (brightness before – brightness after) was referred to the results of the American Dental Association standard. The reference runs were performed as outlined by the American Dental Association using the V-8 cross-brushing machine equipped with the manual brush.

Data management and analysis

Data was analyzed using a one-way analysis of variance model [Sigma Plot Software, San Jose, CA, US]. Data was further analyzed doing all pairwise multiple comparison procedures (Student-Newman-Keuls method). All analyses were done with the significance level of 0.05.

Surface roughness measurement by profilometry and atomic force microscopy

To analyze the effects of different toothbrushing regimens on enamel surfaces, we employed two methods: profilometry and atomic force microscopy.

The same specimens were investigated in both methods. Bovine enamel specimens were polished with abrasive paper, grain size up to 6000, to ensure a standardized surface. The specimens were brushed for 1 h in a slurry containing 1 part water and 1 part toothpaste at a constant pressure tension of 150 g and at constant strokes of 20 mm at a rate of 20/minute. Here we used Braun-Oral-B® Professional Care 500 (Procter & Gamble, Schwalbach, Germany).

As an internal control of an unbrushed/untreated tooth surface 1/3 of each specimen was masked by an adhesive tape. After treatment and before measurement the adhesive tape was removed and residual glue was gently removed with an ethanol-containing wipe.

To evaluate the surface roughness by profilometry, we determined the differences in the Ra values (ΔRa , nm) between brushed and unbrushed tooth surface areas. To determine the Ra values we used a Perthometer (Mahr, Göttingen, Germany). To visualize

these differences by atomic force microscopy, the enamel surfaces were scanned using a NanoScope (Digital Instruments, Tonawanda, NY, USA) at a scan rate of 0.5 Hz and a scan size of 50 μm .

RESULTS

Relative dentin abrasion

The relative dentin abrasion analyses with manual toothbrushes (Table II) revealed that toothpastes B and D are significantly less abrasive than toothpastes A and C.

When brushed with powered toothbrushes, a substantial increase in dentin abrasion in the magnitude of 3.12 to 5.61-fold that of the manual brush was found for all toothpastes tested. Toothpastes B and D showed significantly lower abrasion than toothpastes A and C, which were the toothpastes with the highest relative dentin abrasion values.

Relative enamel abrasion

The relative enamel abrasion analyses with manual toothbrush use (Table III) revealed that toothpastes in the “whitening” segment were significantly more abrasive on enamel abrasion than “regular” toothpastes.

When brushed with powered toothbrushes, a substantial increase in enamel abrasion in the magnitude of 2.78 to 4.79-fold that of the manual brush was seen for all toothpastes tested. This was similar to the findings for dentin abrasion.

Surface roughness measurement by profilometry and atomic force microscopy

The results for the enamel surface obtained by profilometry and atomic force microscopy support the findings for the enamel abrasion. Toothpastes A and C affected the enamel surfaces more than toothpastes B and D. These effects were quantified by the DRa and clearly visualized also by atomic force microscopy (Figure I).

	Manual brush Mean (SEM)	Significant differences between groups ($p>0.05$)	Powered brush Mean (SEM)	Significant differences between groups ($p>0.05$)
Toothpaste A	128.23 (6.33)	Group 1	400.14 (38.86)	Group 2
Toothpaste B	55.39 (1.46)	Group 2	246.41 (32.37)	Group 3
Toothpaste C	125.44 (4.79)	Group 1	552.04 (29.86)	Group 1
Toothpaste D	40.27 (2.26)	Group 3	226.02 (18.84)	Group 3

Table II: Relative Dentin Abrasion (RDA) Values (\pm SEM) and Groups with Significant Differences in Dentin Specimens Following Brushing with Toothpastes A-D, either with Manual or Powered Toothbrushes.

	Manual brush Mean (SEM)	Significant differences between groups ($p>0.05$)	Powered brush Mean (SEM)	Significant differences between groups ($p>0.05$)
Toothpaste A	4.56 (0.42)	Group 1	12.66 (1.33)	Group 1
Toothpaste B	3.45 (0.42)	Group 1	13.02 (1.55)	Group 1
Toothpaste C	1.79 (0.14)	Group 2	8.57 (0.96)	Group 2
Toothpaste D	2.01 (0.30)	Group 2	6.9 (0.40)	Group 2

Table III: Relative Enamel Abrasion (REA) Values (\pm SEM) and Groups with Significant Differences in Dentin Specimens Following Brushing with Toothpastes A-D, either with Manual or Powered Toothbrushes.

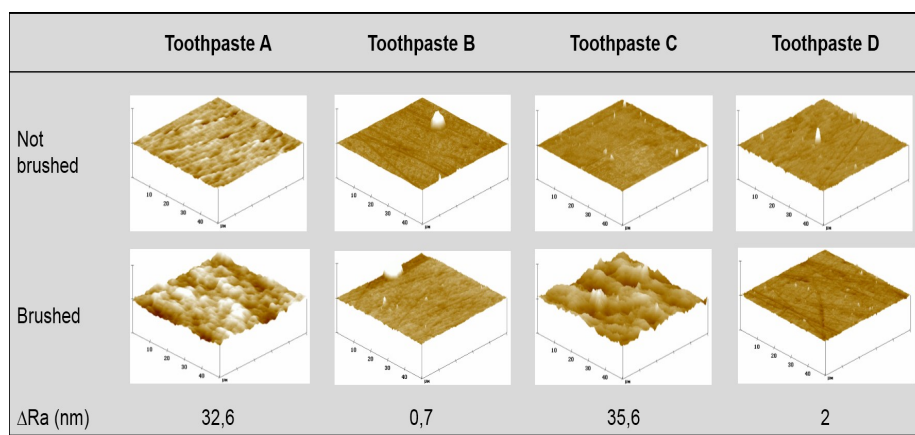


Figure I: Surface roughness measurement by profilometry (DRa, nm) and atomic force microscopy of enamel specimens following brushing with toothpastes A-D and powered toothbrushes.

	Manual brush Mean (SEM)	Significant differences between groups ($p>0.05$)	Powered brush Mean (SEM)	Significant differences between groups ($p>0.05$)
Toothpaste A	93.57 (1.67)	Group 2	95.21 (3.24)	Group 1
Toothpaste B	78.43 (1.95)	Group 3	83.25 (2.33)	Group 2
Toothpaste C	102.14 (2.26)	Group 1	93.18 (1.84)	Group 1
Toothpaste D	65.99 (1.88)	Group 4	77.86 (1.21)	Group 2

Table IV: Cleaning Efficacy Measured by Pellicle Cleaning Ratio (Mean Values \pm SEM) as Described by Stookey, et al. (1982)

	Manual brush	Powered brush
Toothpaste A	0,73	0,24
Toothpaste B	1,42	0,34
Toothpaste C	0,81	0,17
Toothpaste D	1,64	0,34

Table V: Cleaning Efficacy Versus Dentin Abrasion

Cleaning Performance

The results for the stain removal efficacy measured by the pellicle cleaning ratio (**Table IV**) show significant differences in the cleaning performances between toothpastes when brushed with manual toothbrushes. Toothpaste C performed best, followed by A, B, and D in that order.

When brushed with powered toothbrushes, no substantial increase in cleaning performance was seen. Results were in the magnitude of 0.91 to 1.18-fold those of manual toothbrushes.

To evaluate the balance between the cleaning benefit and abrasion risk, we calculated the ratio between cleaning performance (pellicle cleaning ratio, PCR) and abrasion (relative dentin abrasion, RDA) (**Table V**). The higher the PCR/RDA ratio the more effectively the toothpaste is supposed to clean the teeth while being gentle to the dentin. Toothpastes B and D had the best ratio with both the manual and powered toothbrushes.

DISCUSSION

This study had two main objectives: a) elucidate the balance between cleaning performance and dental tissue abrasion of different toothpaste formulation when brushed with manual or high oscillating-rotating powered toothbrushes and b) evaluate if formulations developed especially for use with powered toothbrushes have advantages in terms of dental tissue abrasion and cleaning efficacy. To measure these effects, various in vitro test methods were used, the relative dentin abrasion, relative enamel abrasion and pellicle cleaning ratio [10, 11, 12] as well as profilometry and atomic force microscopy. The four tested toothpastes were chosen from the German market and belong to the "regular" or "whitening" toothpaste segment, whereas one formula of each segment was developed especially for use with powered toothbrushes.

The results can be summarized by the following key findings:

- Toothpaste formulations used with an oscillating-rotating powered toothbrush showed higher abrasion of dental hard tissue (relative dentin abrasion; relative enamel abrasion) than with a manual toothbrush.
- Toothpaste formulations used with an oscillating-rotating powered toothbrush showed no significantly improved cleaning performance (PCR) compared with a manual toothbrush.
- Toothpaste formulations developed especially for use with oscillating-rotating powered toothbrushes resulted in less tooth surface roughness and in an optimized balance between cleaning and abrasion ability.

Similar findings on dental hard tissue abrasion were also obtained by Wiegand et al. [7]. In this study, the influence of different powered toothbrushes on sound and eroded dentin was investigated. The results indicated that oscillating-rotating powered toothbrushes lead to an increased loss of demineralized and sound dentin. In addition, a separate study showed that demineralized enamel was also subject to increased wear using powered toothbrushes [8].

When comparing different oral care regimens the experimental in vitro test setup can influence the outcome of studies [13]. Therefore we adapted the standard manual toothbrush protocol for use with powered toothbrushes. Analysis of the dentin abrasion using the relative dentin abrasion revealed very high values for all toothpastes when brushed with powered toothbrushes. The American Dental Association recommends a relative dentin abrasion of 250 as the upper limit, as described in the ISO Standard 11609:2010 Dentifrices [11]. Although the test protocol for testing powered toothbrushes as implemented in this study is not described in this ISO guideline - making a direct link to the American Dental Association recommendation difficult - the relative dentin abrasion values obtained are very high.

In contrast, toothpastes B and D, which were developed specifically for use with powered toothbrushes, also showed increased relative dentin abrasion values, but below the recommended values of 250. Although the increase in relative enamel abrasion values was similar for the different regimens, the values were below the maximum level of 40 recommended by the American Dental Association (ISO 11609:2010) [11]. Similar findings that certain ingredients affect dentin and enamel differently are known and described elsewhere [1, 14].

In vitro methods can be used to assess mechanisms, but correlating them with the in vivo situation is often difficult. Many clinical studies support the safety of powered toothbrushes [5, 6]. Tooth wear is a multifactorial process, triggered by individual brushing techniques and it slowly develops in the course of years until it might reach clinical relevance. Among clinical studies assessing the safety of powered toothbrushes [reviewed in 6], the longest study period was 18 months [16]. However, this might be too short to assess any measurable effect of oral care regimens on tooth wear.

Another aspect to be reviewed in this context is dental erosion mostly due to changing nutrition habits. As described by Wiegand et al. [8], powered toothbrushes show a higher abrasion on demineralized enamel. If the individual lifestyle tends to support demineralization and erosion, the risk of losing enamel during the daily oral care regimen is increased.

While several studies have indicated that powered toothbrushes have advantages in terms of cleaning efficacy, plaque removal and gingival health [15, 16], it should be of interest to improve the oral hygiene even further by using toothpaste formulations with a proven low abrasive potential. In this in vitro study two products specifically developed for use with powered toothbrushes (toothpastes B and D) were evaluated. Among the tested endpoints of this study, they showed superior results with a high cleaning performance and a low abrasive potential. To reach this goal the optimal ratio

between gentle cleaning particles and surfactants was identified during formula development. Furthermore to meet the requirement for a whitening toothpaste, we avoided use of harsh cleaning particles, but increased the cleaning performance by using sequestrants that dissolve stubborn stains, which then can be removed more gently with brushing. In addition, these toothpastes meet the needs of consumers who frequently use powered toothbrushes by offering an improved freshness and foaming experience.

As life expectancy rises people need to rely on healthy teeth for a longer period of life. A suboptimal oral care regimen that supports increased tooth wear will backfire with age, either introducing high costs for tooth restoration or leaving aged people desperate. Therefore it is important to do the utmost for proper oral hygiene by applying the right brushing technique especially in terms of the right brush tension and by using toothpastes with an optimized abrasion/cleaning ratio.

CONCLUSIONS

In the present study we compared the influences of different toothpastes in combination with oscillating-rotating powered toothbrushes and manual toothbrushes in terms of dental hard tissue abrasion and cleaning performance.

These in vitro studies indicate that some toothpastes in combination with powered toothbrushes might negatively influence dental hard tissue abrasion with a limited improvement in cleaning efficacy. Over years, this might lead to loss of tooth form, function and esthetics, as well as to dental hypersensitivity.

Toothpastes developed especially for use with powered toothbrushes showed an improved ratio of abrasion versus cleaning and thereby can further improve oral hygiene.

Acknowledgment: We would like to thank Hans Laska and Wilfried Howorka for excellent support in the analytical tests and Nicole Duschek and Jennifer Evening for product development.

REFERENCES

- [1] Attin, T., *Erosion und Abrasion von Zahnhartsubstanz – Einflussfaktoren, Pathogenese und Therapie*, In: Heidemann D (ed.), *Deutscher Zahnärztekalendar*, 58 (1999) 1-3.
- [2] Hunter, M.L., Addy, M., Pickles, M.J., and Joiner, A., *The role of toothpastes and toothbrushes in the etiology of tooth wear*, *Int. Dent. J.*, 52(SUPPL.2) (2002) 399-405.
- [3] Addy, M., and Hunter, M.L., *Can toothbrushing damage your health? Effects on oral and dental tissue*, *Int. Dent. J.*, 53 (Suppl3) (2003) 177-186.
- [4] Deacon, S.A., Glenny, A-M, Deery, C, Robinson, P.G., Heanue, M., Walmsley, A.D., and Shaw, W.C., *Different powered toothbrushes for plaque control and gingival health*, *Cochrane Database of Systematic Reviews*, 12 (2010)
- [5] Robinson, P., Deacon, S.A., Deery, C., Heanue, M., Walmsley, A.D., Worthington, H.V., Glenny, A.M., and Shaw, B.C., *Manual versus powered toothbrushing for oral health*, *Cochrane Database of Systematic Reviews*, 2 (2005)
- [6] Van der Weijden, F.A., Campbell, S.L., Dörfer, C.E., Gonzalez-Cabezas, C., and Slot, D.E., *Safety of oscillating-rotating powered brushes compared to manual toothbrushes: A systemic review*, *J. Periodontol.*, 81(1) (2011) 15-24.
- [7] Wiegand, A., Lemmrich, F., and Attin, T., *Influence of rotating-oscillating, sonic and ultrasonic action of power toothbrushes on abrasion of sound and eroded dentine*, *J. Periodontol. Res.*, 41 (2006) 221-227.
- [8] Wiegand, A., Begic, M., and Attin, T., *In vitro evaluation of abrasion of eroded enamel by different manual, power and sonic toothbrushes*, *Caries Res.*, 40 (2006) 60-65.
- [9] Schemehorn, B.R., Moore, M.H., and Putt M.S., *Abrasion, Polishing, and stain removal characteristics of various commercially dentifrices in vitro*, *J. Clin. Dent.*, 22 (2011) 11-18.
- [10] Hefferen, J.J., *A laboratory method for assessment of dentifrice abrasivity*, *J. Dent. Res.*, 55 (1976) 563-573.
- [11] ISO 11609:2010 – Dentistry – Toothpastes – Requirements, test methods and marketing.
- [12] Stookey, G.K., Burckhardt, T.A., and Schemehorn, B.R., *In vitro removal of stain with dentifrices*, *J. Dent. Res.*, 61 (1982) 1236-1239
- [13] Wiegand, A., and Attin, T., *Design of*

Erosion/Abrasion Studies – Insights and Rational Concepts, 45(suppl) (2011) 53-59.

[14] Moore, C., and Addy, M., *Wear of dentine in vitro by toothpaste abrasives and detergents alone and combined*, *J. Clin. Periodontol.*, 32 (2005) 1242-1246.

[15] Dentino, A.R., Derderian, G., and Wolf, M., *Six month comparison of powered versus manual toothbrushing for safety and efficacy in the absence of professional instruction in mechanical plaque control*, *J. Periodontol.*, 73 (2002) 770-778.

[16] Ainamo, J., Xie, Q., Ainamo, A., and Kallio, P., *Assessment of the effect of an oscillating-rotating electrical toothbrush on oral health. A 12-month longitudinal study*, *J. Clin. Periodontol.*, 24 (1997) 28-33.

Corresponding author
email: Thomas.Welss@Henkel.com